STARS

University of Central Florida
STARS

Electronic Theses and Dissertations, 2004-2019

2010

Tunable Infrared Metamaterials

David Shelton
University of Central Florida

 Part of the Materials Science and Engineering Commons
Find similar works at: https://stars.library.ucf.edu/etd
University of Central Florida Libraries http://library.ucf.edu

This Doctoral Dissertation (Open Access) is brought to you for free and open access by STARS. It has been accepted for inclusion in Electronic Theses and Dissertations, 2004-2019 by an authorized administrator of STARS. For more information, please contact STARS@ucf.edu.

STARS Citation
Shelton, David, "Tunable Infrared Metamaterials" (2010). *Electronic Theses and Dissertations, 2004-2019*. 4269.
https://stars.library.ucf.edu/etd/4269

TUNABLE INFRARED METAMATERIALS

by

DAVID SHELTON
B.S. University of Evansville, 2005
M.S. University of Central Florida, 2007

A dissertation submitted in partial fulfillment of the requirements
for the degree of Doctor of Philosophy
in the Department of Mechanical, Materials, and Aerospace Engineering
in the College of Engineering and Computer Science
at the University of Central Florida
Orlando, Florida

Summer Term
2010

Major Professor: Glenn D. Boreman

© 2010 David Shelton.

ABSTRACT

Metamaterials are engineered periodic composites that have unique refractive-index characteristics not available in natural materials. They have been demonstrated over a large portion of the electromagnetic spectrum, from visible to radiofrequency. For applications in the infrared, the structure of metamaterials is generally defined using electron-beam lithography. At these frequencies, the loss and dispersion of any metal included in the composite are of particular significance. In this regard, we investigate deviations from the Drude model due to the anomalous skin effect. For comparison with theoretical predictions, the optical properties of several different metals are measured, both at room temperature and at 4 K. We extend this analysis to the coupling between plasmon and phonon modes in a metamaterial, demonstrating that very thin oxide layers residing at the metal-substrate interface will significantly affect the spectral location of the overall resonance. Oxide-thickness-dependent trends are then explored in some detail. Potential applications of this general area of study include surface-enhanced infrared spectroscopy for chemical sensing, and development of narrowband notch filters in the very long wavelength infrared. We then consider various possibilities for development of tunable infrared metamaterials. These would have wide applicability in dynamically variable reflectance surfaces and in beam steering. We consider several methods that have been previously shown to produce tunable metamaterials in the radio frequency band, and explore the challenges that occur when such techniques are attempted at infrared frequencies. A significant advance in tunable-infrared-metamaterial technology is then demonstrated with the use of thermochromic vanadium dioxide thin films. Highlights include the first demonstration of a tunable reflectarray in the infrared for active modulation of reflected phase, the first

demonstration of a tunable resonance frequency in the thermal infrared band, and the largest resonance-frequency shift recorded to date in any part of the infrared. Finally, future work is proposed that holds the promise of wideband frequency tuning and electronically-controllable metamaterials.

ACKNOWLEDGMENTS

Portions of this research including the thermochromic reflectarray, DC Schottky diode tunable devices, and the photoconductive tunable devices were supported by grants from Northrop Grumman Space Technologies, and the Florida High Tech Corridor Council.

Portions of this research including work on flexible elements and THz filters were supported by grants from Idaho National Labs.

Portions of this research including work on fringing field capacitance effects in split-ring resonator metamaterials and plasmon-phonon coupling were supported by the Laboratory Directed Research and Development program at Sandia National Laboratories. Sandia is a multiprogram laboratory operated by Sandia Corporation, a Lockheed Martin Company, for the United States Department of Energy's National Nuclear Security Administration under Contract DE-AC04-94AL85000.

TABLE OF CONTENTS

LIST OF FIGURES

LIST OF TABLES

LIST OF SYMBOLS/ABBREVIATIONS

Al……..Aluminum

Au……...Gold

BCB……...……...B-staged Bisbenzocyclobutene

CMP……..Chemical-Mechanical Polish

CAD……..Computer Aided Drafting

dc……...Direct Current

deg……..Degree

εr……...…..Dielectric Constant

e-beam……Electron Beam

F/#.....F-number

FEM……..…Finite Element Method

FSS……...Frequency Selective Surface

fs……...….Femtosecond (10^{-15} second)

FWHM…….Full Width Half Maximum

FZP……...Fresnel Zone Plate

GUI…….....Graphical User Interface

HeNe…….Helium Neon

HFSS…….……High Frequency Simulation Software

IR…….....Infrared

IR-VASE……..Infrared Variable Angle Spectral Ellipsometer

IPA…….. …….Isopropyl Alcohol

kV……..Kilovolt (10^3 Volt)

LHM…….……Left Handed Material (Medium)

LWIR……Long-Wave Infrared (8^{-15} μm)

m……...Meter

μm...……....Micrometer (10^{-6} Meter)

μC...…….....Microcoulomb (10^{-6} Coulomb)

mm...……...…….…….Millimeter (10^{-3} Meter)

MPIE…….. Mixed-Potential Integral Equation

MSE…….Mean Square Error

MWIR…...…….Mid-Wave Infrared (3^{-8} μm)

NIR……Near Infrared (0.75^{-3} μm)

OPD…….…Optical Path Difference

Ni…….Nickel

nm...…….Nanometer (10^{-9} Meter)

nA……..….Nanoamp (10^{-9} Ampere)

NIM…….……Negative Index Metamaterial

PEC……..…Perfect Electric Conductor

PMC……..Perfect Magnetic Conductor

Pt…….……..…Platinum

PVD……Physical Vapor Deposition

rf……...Radio Frequency

RHM…….……..Right Handed Material (Medium)

S……...….Siemens

SEIS……Surface-Enhanced Infrared Spectroscopy

SEM……..Scanning Electron Microscope

SP……..Surface Plasmon

SPP…….Surface Plasmon Polariton

SRR……..…….Split-Ring Resonator

δskin……...….Skin Depth

tan(δ)……..……Loss Tangent

THz…...……...……...Terahertz (10^{12} Hertz)

Ti……..…Titanium

ZDMAC……...……...N,N-Dimethylacetamide

ZEP RD…..….Xylene (o-, m-, p- mixed)

ZEP Resist……Methyl Styrene / Chloromethyl Acrylate Copolymer

ZrO2….……Zirconium-Dioxide

CHAPTER 1: INTRODUCTION

1.1 Metamaterial Definition and Motivation

Materials Science is the study of how physical structure determines the mechanical, electrical, thermal, magnetic, and optical properties of a thin film or bulk material. This dissertation will focus on the optical properties of thin films, and in particular metallic films. Dielectric, or electrically insulating, thin films are well known to have many interesting optical properties resulting from their physical structure including thermochromism which will be discussed in this dissertation. The optical properties of metallic films, particularly as relates to their physical structure, have historically been regarded with less interest. Metals reflect electromagnetic radiation and can be polished to make mirrors. Within the bounds of traditional metallurgical processing there is nothing that can change this basic behavior.

In recent years work in metamaterials and plasmonics has brought considerable interest to the optical properties of metallic thin films, and to controlling the optical properties of a surface using metallic thin films by artificially engineering nanoscale structures. The capability to artificially structure metal elements at a sub-wavelength scale into a periodic array has been enabled by the increased availability of electron-beam (E-beam) lithography over the past decade. Using such elements it is possible to control the way a surface transmits, absorbs, reflects, or emits radiation in such a way that would not be possible with metallurgical processing or in naturally occurring materials. These composite material thin film systems consisting of sub-wavelength scale metallic element

arrays layered with dielectric thin films and a substrate are called metamaterials. Metamaterials have extraordinary optical properties that can not be achieved in normal materials.

Although the artificial structure primarily determines the optical properties of a metamaterial, the physical structure and the properties of the constituent metal films at the frequency at which they are used also determine the metamaterial's behavior. This fact is often overlooked in the literature leading to grandiose claims based upon simulations using idealized material properties. In this dissertation the IR optical properties of metal and dielectric films will be carefully considered in each experiment.

Metamaterials were first constructed in the radio frequency (RF) portion of the electromagnetic spectrum and have been built for increasingly shorter wavelengths for the past decade. The focus of this dissertation will be metamaterials in the infrared (IR) portion of the spectrum. The IR spectrum is sub-divided into three bands of interest; the near-IR from 1.5 to 3 μm in wavelength, the mid-IR from 3-8 μm in wavelength, and the thermal-IR from 8-12 μm in wavelength. The thermal-IR is so named because a blackbody at 300 K will emit most strongly in this band. While a range of metamaterial configurations and applications are considered in this dissertation, all of the experiments share common design, fabrication, and testing methods.

1.2 Design, Fabrcation, and Testing Methods

1.2.1 Design with Finite Element Method

The numerical simulation tool used for the experiments in this dissertation was finite-element method (FEM) with the Ansoft HFSS commercial software. The user inputs a unit cell design using a CAD interface and then defines electromagnetic constants for each component in the unit cell. The software then uses FEM and the electromagnetic boundary conditions to solve Maxwell's equations to determine how incident radiation is scattered or absorbed by the unit cell.

The FEM simulations considered linearly polarized radiation at normal incidence to a unit cell constructed using the software's CAD interface. In addition to the unit cell, periodic boundary conditions are applied so that all calculations are made for the case of an infinite array. This accounts for interelement coupling. For example Fig. 1.1 shows an HFSS model for a split-ring resonator (SRR) metamaterial.

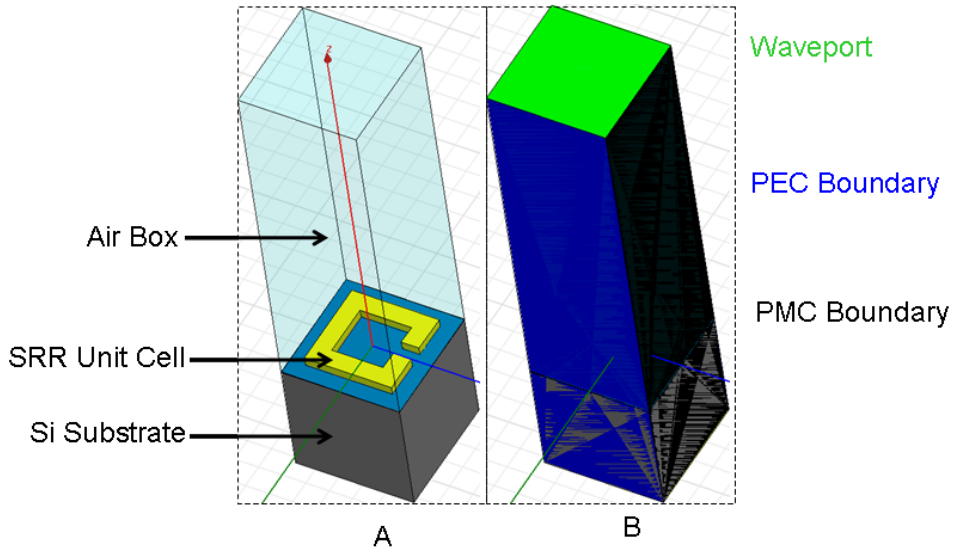

Figure 1: A: HFSS unit cell in standard view, B: HFSS unit cell in solver view to show boundary setup.

Part A of Fig. 1 shows the standard HFSS view with an air box surrounding the unit cell to define boundaries for the solver. Each side of the air box is given a boundary condition as shown in solver view in part B of Fig 1. The boundary conditions are symmetric about the axis such that the boundary conditions of the three sides not shown are the same as the opposite side. The waveports on the top and bottom of the unit cell act as both source and receiver of radiation. The top waveport is designated 1, and the bottom waveport is designated 2, so that the radiated power S_{ij} can be defined. In this nomenclature i is the radiation source, and j is the receiver, so S_{11} would be the radiated power reflected from the unit cell, and S_{12} would be radiated power transmitted through the unit cell. Since the sum of radiated power reflected, transmitted, and absorbed must be equal to unity, the absorbed power is determined by taking unity minus the sum of S_{11} and S_{12}.

With the setup shown in Fig 1 two linear polarization states are possible depending upon which axis is chosen to have perfect electric conductor (PEC) boundaries. In the case of SRR elements this choice is important because the resonant mode depends upon whether the electric field is parallel or perpendicular to the gap. The radiation mode that is generated by this configuration may only propagate normal to the element in the unit cell. Grazing angle incidence will not be considered in this dissertation.

An important consideration in addition to the electromagnetic boundary conditions is the material properties used for the different parts of the unit cell. Depending upon the needs

of the experiment, HFSS simulations are done across a region of the IR spectrum. In almost any material, dispersion is significant in any appreciable bandwidth in the IR. Thus frequency dependent material constants are used for each layer and element present in the unit cell. There are several equivalent ways to describe the complex optical constants such as dynamic conductivity, permittivity, or the index of refraction (real part) and extinction coefficient (imaginary part). It is also possible to use some combination of the three, but it is best to pick a convention to use in simulations. For the simulations in this dissertation the real and imaginary parts of permittivity are used for both the conductors and dielectrics. This method produces the best agreement when simulations are compared to measurements, and is preferred over using only the real part of dynamic conductivity to represent conductors.

Permittivity values over large spectral ranges are available from many sources in the literature, but as the optical properties depend upon the physical structure of the thin film such sources are not always accurate. There is also only a limited amount of IR data. To solve these problems IR Ellipsometry was used to measure the frequency dependent optical constants for all of the thin films used in this dissertation. A J.A. Woollam VASE system was used with the capability to measure from 2 to 40 μm in wavelength and is shown in Fig 2.

Figure 2: J.A. Woollam IR VASE Ellipsometer

Ellipsometry measurements were made by sending circularly polarized IR radiation incident onto a continuous thin film sample at a grazing angle. The IR radiation that is reflected from the sample is elliptically polarized, and polarization optics are used to measure the power ratio of the two orthogonal components of the ellipse, and the relative phase difference between these components. Both of these spectral measurements will depend upon the composition, film thickness, and many other details of the sample. A model is then constructed and fit to the polarization data. Optical constants may be extracted from this model. In some cases when only one interface is present, for example an optically thick metal film, optical constants may be calculated directly from the polarization data. In most cases the sample consists of a thin film that is at least partially transparent on a substrate, and a model must be used to account for thin film interference effects. While modeling tools such as HFSS are helpful in the initial designing stage, the simulations are only a first step and it takes multiple characterization steps for a simulation to match fabricated designs.

1.2.2 E-beam Lithography and Lift-Off Processing

Once a design is complete the next step is to fabricate metamaterial elements using electron beam (E-beam lithography) and standard semiconductor processing techniques. The thin films used in this dissertation's experiments were deposited using physical-vapor deposition (PVD) by either sputtering or E-beam evaporation. These processes are described in detail for the individual experiments. The main topic to be introduced here is the lift-process that is used for the elements in all of the experiments. Figure 3 shows the process flow for single and multiple layer metamaterial elements.

Most of the experiments in this dissertation use only single layers of elements. Specifics of E-beam resist type and dose are discussed further in chapter 4. After spinning resist onto a Si wafer a metamaterial pattern is exposed using the Leica direct-write E-beam lithography system. The pattern is defined using CAD software such as L edit, and the resulting file is converted for use with the Leica. During the exposure step the elements are written one at a time with a 1 to 25 nA beam on a raster scan stage. Depending upon the size of the elements to be used, a typical write time for a 1 cm by 1 cm element array would be several hours. To fully populate a standard 4 inch diameter wafer with metamaterial elements can take several days of write time. The exposed sections of the resist polymer are now cross linked and can be etched away using a developer solvent. The next step is to deposit metal onto the resist pattern. This is done with E-beam evaporation rather than sputtering because the deposition needs to be highly directional for proper lift-off to occur. Finally the resist is stripped using a second chemical solvent to leave only the metallic elements behind.

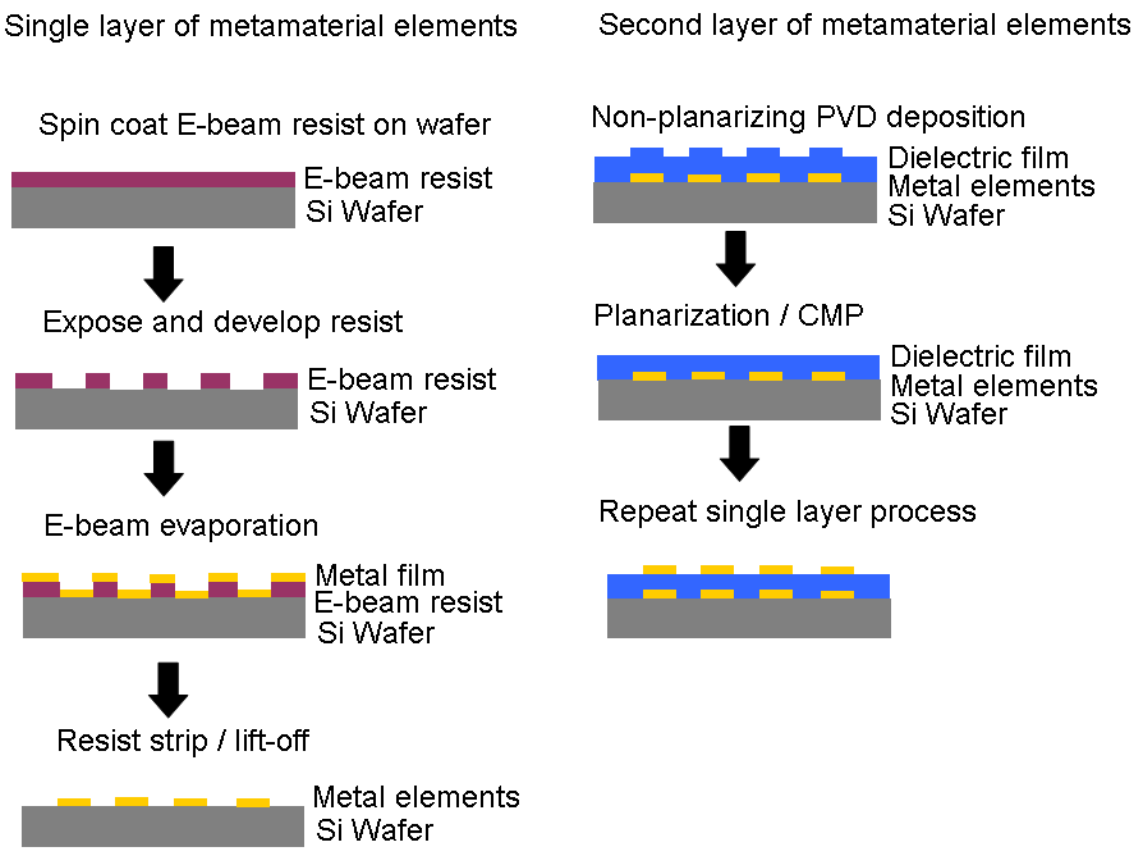

Figure 3: Device cross section diagrams and process flow for liftoff lithography.

Figure 3 also shows process steps required for a second layer of elements. Multiple layer metamaterials will be considered in further detail in chapter 5, and it is critical to understand the planarization issue involved whenever multiple layers are considered. If a PVD deposition is used for the dielectric spacer between element layers then the surface contour from the first layer of elements will be projected to the second layer. There are two possible ways to planarize the dielectric spacer before fabricating the second layer of elements. The direct method is to use chemical-mechanical polishing (CMP), but since the dielectric spacer may be an unusual material for semiconductor processing it is not trivial to find a polishing house to perform the process. Developing new CMP recipes for the variety of dielectric spacer materials available in the IR can be costly and time

consuming. An alternative method is to use self-planarizing materials that may be spun onto the wafer, or dip coated. This limits the available materials for IR dielectrics compared to PVD, but several choices are considered in chapter 5 as well as appendix C.

1.2.3 Metamaterial Testing Techniques

Once fabrication of a new metamaterial surface is complete it is tested to determine how it spectrally reflects, transmits, absorbs, or emits IR radiation. Additionally the tunable metamaterials in chapter 6 are tested to determine their change in reflected phase, but the power measurements used in all of the experiments are the focus of this section. Spectral reflection and transmission are measured with a Perkin-Elmer FTIR spectrometer. This is done with a microscope attachment so that metamaterial elements need only populate an array that is 1 mm by 1 mm in size. The FTIR uses a broad band source that covers the band from 1.5 to 25 μm and then uses a numerical Fourier transform technique to determine the spectrum of the scattered radiation received by the detector. This gives the FTIR the ability to measure the data from a large portion of IR spectrum quickly without taking measurements at one frequency at a time using a filter wheel. A more detailed explanation of FTIR spectroscopy may be found in Ref. 1.1.

While the FTIR may be used to collect spectral reflection data from any planar surface, transmission data requires a transparent substrate. In order to be IR transparent, Si wafers must be double side polished and high resistivity to avoid free-carrier absorption. Absorption may also be measured with an FTIR, but it is not always reliable. If both the spectral transmission and reflection are known, then so is the absorption based on

conservation of energy. However in practice the FTIR is more reliable for determining the spectral location and bandwidths of resonant features than in measuring their magnitudes. This is particularly important when measuring potential tunable metamaterials. A shift in the amplitude of reflected power with no corresponding spectral change in features (resonant minima shifts, bandwidth changes) should not be trusted as evidence of tunability. Several examples of this pitfall will be seen in chapter 6.

One round through the design, fabrication, and testing process is only the beginning. After testing is complete the original simulation is corrected to account for actual versus ideal element dimensions, native oxide layers, and other features and phenomena. A new design may then be fabricated and tested and the cycle is repeated. A good example is the experiments presented in chapter 5 which detail the most precise metamaterial experiments done to date in the IR resulting in excellent agreement between simulation, analytical model, and measured data.

1.3 Thesis

It is the intended goal of this dissertation to explain how the properties of the constituent thin films and elements comprising an IR metamaterial affect the composite's behavior. This is demonstrated for a variety of element geometries in both static and tunable metamaterials. The anomalous skin effect is shown to affect the properties of metallic thin films and can play an unexpected role in the behavior of metamaterials at cryogenic temperatures. In addition to the properties of the metallic elements, the surrounding

dielectric layers also play a role. Even layers as thin as the native oxide on a Si wafer are shown to affect the resonant frequency of SRR elements. It is then shown that incident IR radiation excites plasmonic-cavity modes in metamaterials which can couple to phonon modes in surrounding dielectric layers. Finally it is shown how materials with electronically, or thermally, controlled optical properties may be used to build tunable metamaterials.

1.4 Prior Publication and Financial Support Disclosure

Portions of this research including the thermochromic reflectarray, DC Schottky diode tunable devices, and the photoconductive tunable devices were supported by grants from Northrop Grumman Space Technologies, and the Florida High Tech Corridor Council.

Portions of this research including work on flexible elements and THz filters were supported by grants from Idaho National Labs.

Portions of this research including work on fringing field capacitance effects in split-ring resonator metamaterials and plasmon-phonon coupling were supported by the Laboratory Directed Research and Development program at Sandia National Laboratories. Sandia is a multiprogram laboratory operated by Sandia Corporation, a Lockheed Martin Company, for the United States Department of Energy's National Nuclear Security Administration under Contract DE-AC04-94AL85000.

Portions of chapter 3 were published previously by the author in Ref. 1.2. Portions of chapter 4 were published previously by the author in Refs. 1.3-1.4. Portions of chapter 5 were published previously by the author in Refs. 1.5-1.6. Portions of chapter 6 were published previously by the author in Refs. 1.7-1.8.

CHAPTER 2: THEORETICAL BACKGROUND

2.1 The Drude and Sommerfeld Models

In the contemporary literature the majority of papers on topics concerning the optical properties of metallic thin films begin by stating that permittivity may be calculated according to the Drude model. This is often approximated as Eq. 2.1 which only gives the real part of the permittivity and assumes that there is no damping.

$$\varepsilon_r = 1 - \frac{\omega_p^{\,2}}{\omega^2} \tag{2.1}$$

The permittivity is written this way to emphasize that when the frequency of the incident radiation, ω, is below the plasma frequency, ω_p, the dielectric function has a negative value. This is significant for metamaterials as will be discussed in chapter 2.3. In the Drude model the electro-optical behavior of metals is approximated by the kinetic theory of a dilute gas. Since we are primarily concerned with metals in a condensed state this requires some explanation.

The Drude model has been in use since the beginning of the 20th century, and thus predates modern descriptions of the atom. A Drude metal may be considered to consist of a collection of positively charged ions that are balanced by an equal number of free electrons such that charge neutrality is maintained. This description may be translated to say that the ionic cores are the nucleus and bound electrons and that the free electrons are the valence electrons. The valence electrons are assumed to be free in the sense that they do no not interact with the ion cores, but not so free that they can escape from the metal. These free electrons move about on straight line paths behaving just like particles in a

gas. If an external electric field is applied the motion of the free electrons may be considered to occur according to Newton's laws. As in the kinetic theory of gases, the velocity of the free electrons depends upon the temperature of the metal and may be calculated using the Maxwell-Boltzmann distribution. In the absence of an external electric field the free electrons, like particles in a gas, will move in random directions such that their net velocity is equal to zero.

The other key feature of the Drude model is that free electrons can suffer inelastic collisions as they move about. This accounts for electrical resistivity, but is not always mentioned when considering the optical properties of a metal film as in Eq. 2.1. In the Drude model electrons are assumed to not interact with each other and since the metal is modeled as a dilute gas there is no physical structure to scatter electrons either. Therefore the free electrons are assumed to collide exclusively with the ion cores. We may also define an electronic mean free path λ_{mfp} between collisions, and then depending upon the velocity of the electrons, a scattering time τ. The motion of the free electrons will then have a damping rate equal to $1 / \tau$ that must be accounted for.

Analytical equations for the optical properties of a metal may be determined by considering the response of a metal to an electric field according to the Drude model. A DC electric field vector ***E*** will move electrons though some area of the metal allowing us to define a current density ***J*** which will be parallel to ***E***. The two vectors may be related by a DC conductivity σ_0 according to Eq. 2.2.

$$\vec{J} = \sigma_0 \vec{E} \tag{2.2}$$

This leads to the derivation of σ_0 [2.1] resulting in Eq. 2.3.

$$\sigma_0 = \frac{Ne^2\tau}{m} \tag{2.3}$$

In Eq. 2.3 N is the concentration of free carriers (valence electrons) per unit volume, e is the charge on the electron, and m is the mass of the electron. When IR radiation is incident on a metal film the external electric field is now a function of frequency and has the form $\boldsymbol{E_0}exp(-i\omega t)$ of a time-harmonic wave. Modifying Eq. 2.2 for a time-harmonic field and current-density wave necessitates that conductivity as a function of frequency, or dynamic conductivity, be considered as well. To do so we write the equation of motion for a free electron as in Eq. 2.4. [2.2]

$$m\frac{d^2x}{dt^2} + m\frac{1}{\tau}\frac{dx}{dt} = -e\vec{E}_0\exp(-i\omega t) \tag{2.4}$$

By assuming solutions for the electron's displacement x are of the form $x_0exp(-i\omega t)$, and since velocity is the derivative of displacement, we can obtain a solution for the free electron's velocity under a time-harmonic field in Eq. 2.5.

$$\vec{v} = \frac{-e\tau}{m}\frac{1}{1-i\omega\tau}\vec{E}_0\exp(-i\omega\tau) \tag{2.5}$$

By combining Eq. 2.5 with the expression for the time-harmonic current-density wave we arrive at the expression for dynamic conductivity in Eq. 2.6.

$$\sigma(\omega) = \frac{\sigma_0}{1-i\omega\tau} = \frac{\sigma_0}{1+(\omega\tau)^2}(1+i\omega\tau) \tag{2.6}$$

The physical meaning of dynamic conductivity is not so clear compared to DC conductivity. With a DC external field we understand that the electrons now travel parallel to the field with some net velocity, and that for a given free carrier density, the lower the conductivity is the more inelastic collisions occur resulting in resistive heating,

or ohmic loss, from the current. In contrast dynamic conductivity is a complex number, and when the frequency ω is on the order of the scattering time τ the external electric field is now out of phase with the current density wave. It is tempting to maintain the resistive heating picture and say that the real part of the dynamic conductivity is still ohmic loss. However we might then look at Eq. 2.6 and see that if we decrease τ in some experiment we can increase the real part of dynamic conductivity if ω is sufficiently large. This is despite the fact that any decrease in τ would decrease the DC conductivity by Eq. 2.3. At the same time the imaginary part of the dynamic conductivity gets larger as well, so it becomes an interesting paradox to try to improve dynamic conductivity by decreasing the DC conductivity. However in the current discussion it is still unclear whether the real part of dynamic conductivity may be equated with ideal optical response from a metal, so we must further describe the optical properties of materials and consider what sort of behavior we would like a metal to have.

Although the dynamic conductivity completely describes the optical properties of a metallic thin film the presence of a large imaginary component makes its physical meaning uncertain. For this reason permittivity is usually used once the $\omega\tau$ product is greater than unity. For most metallic thin films used in metamaterials τ is on the order of 10 fs. In the IR and at higher frequencies permittivity is the easiest way to describe the optical properties of metals. We can relate permittivity to dynamic conductivity by returning to the equation of motion for the free electrons in Eq. 2.4. The solution for the displacement of free electrons is given by Eq. 2.7.

$$x(t) = \frac{eE_0 \exp(-i\omega t)}{m} \frac{1}{\left(\omega^2 + i\frac{\omega}{\tau}\right)} \tag{2.7}$$

The polarization P of the free electron gas is equal to the product of the electron's displacement, its charge, and the concentration of free electrons. Permittivity can then be derived from the electric displacement D in Eq. 2.8.

$$D = \varepsilon_r \varepsilon_0 E = \varepsilon_0 E + P = \varepsilon_0 E - nex \tag{2.8}$$

By substituting Eq. 2.7 into Eq. 2.8 we arrive at an expression for the permittivity of a metal according to the Drude model in Eq. 2.9.

$$\varepsilon_r(\omega) = 1 - \frac{Ne^2}{\varepsilon_0 m} \frac{1}{\left(\omega^2 + i\frac{\omega}{\tau}\right)} \tag{2.9}$$

Using Eqs. 2.9 and 2.6 we can write can an expression for the relationship between the dynamic conductivity and the permittivity in Eq. 2.10

$$\varepsilon_r = 1 + \frac{i\sigma(\omega)}{\varepsilon_0 \omega} \tag{2.10}$$

By considering the relationship in Eq. 2.10 we can begin to understand the physical meaning of the real and imaginary parts of the dynamic conductivity. In Eq. 2.11 permittivity is broken into real, ε_r', and imaginary, ε_r", parts and written in terms of the real and imaginary parts of the dynamic conductivity.

$$\begin{aligned} \varepsilon_r' &= 1 - \frac{\sigma''(\omega)}{\varepsilon_0 \omega} = 1 - \frac{\sigma_0 \tau}{\varepsilon_0 \left(1 + (\omega\tau)^2\right)} = n^2 - k^2 \\ \varepsilon_r'' &= \frac{\sigma'(\omega)}{\varepsilon_0 \omega} = \frac{\sigma_0}{\varepsilon_0 \omega \left(1 + (\omega\tau)^2\right)} = 2nk \end{aligned} \tag{2.11}$$

In Eq. 2.11 n is the index of refraction and k is the extinction coefficient. The real part of dynamic conductivity is related to the imaginary part of the permittivity. The imaginary

part of permittivity is proportional to a material's extinction coefficient and so is related to photons being absorbed by the material. The ideal optical response of a metal is typically reflection, not absorption, and associating the real part of conductivity with photonic absorption rather than ohmic loss may be more meaningful at high frequencies. The real part of permittivity is related to the imaginary part of the dynamic conductivity. If we want metamaterials to have a sharp, narrowband response and a large oscillator strength, then we want the real part of permittivity to be negative sign and large in magnitude. According to Eq. 2.11 this means that we should favor a large imaginary part of the dynamic conductivity.

In metamaterial elements when incident radiation interacts with the metal's free electrons we want this interaction to generate surface current modes that are confined to the surface of the element as much as possible. If the surface current diffuses into the elements this results in broad band resonance and lower oscillator strengths. In some cases a broad-band response is desired, but when broad-band behavior comes at the expense of low oscillator strength (low resonant amplitude, small 'depth of notch') it is not usually a favorable trade off. Therefore the optical properties of a metal that are ideal in most situations for metamaterial elements are low imaginary part of permittivity and large, negative sign, real part of permittivity. It is useful to define a loss tangent as the ratio of the imaginary to the real part of permittivity. The best metallic response will occur when the loss tangent is made to be negative sign and small in magnitude. The relationship between the physical structure and the loss tangent of a metal film will be explored experimentally in chapter 3.

One other feature of the Drude model that was brought up in Eq. 2.1 was the plasma frequency. This is a convention for naming the group of constants appearing in Eq. 2.9 and the plasma frequency is defined in Eq. 2.12.

$$\omega_p = \sqrt{\frac{Ne^2}{\varepsilon_0 m}} \tag{2.12}$$

The plasma frequency marks the frequency limit at which a metal can no longer screen electric fields. For most metals the plasma frequency is in the ultraviolet portion of the spectrum. An incident time-harmonic field having frequency greater than ω_p could propagate through the metal, while at frequencies below ω_p the metal will reflect radiation. Some degree of absorption will occur in either case. The name plasma frequency is used because in the Drude model we approximate a condensed-phase metal as a plasma.

The Drude model is still used to describe the optical properties of metal films because it works as an adequate first-order approximation in many situations such as in modeling metamaterials and plasmonic modes. However, the treatment of a metal as a dilute gas entirely ignores the fact that electron motion is subject to a periodic potential associated with the metal's crystal lattice. Without the resulting theories on electronic-band structure there is no way to explain such basic phenomena as why Au is the color gold in the visible. For the purposes of the optical properties of metals that are most relevant to metamaterials and other applications the full details of electronic-band theory are not necessary. However there are also basic assumptions in the Drude model that affect its prediction of the permittivity at high frequencies that are not necessarily true, and that affect IR metamaterials. Examples include the assumption that the scattering time is

constant with respect to frequency, that the free electron concentration is independent of physical structure, the distribution of electron velocities is determined by the Maxwell-Boltzmann equation. By expanding our view of electron theory to include the Sommerfeld model we can begin to address some of these problems.

The most significant failures of the Drude model are not in its description of the optical or electrical properties of metals, but rather in the thermal properties of metals. To correct these problems, Sommerfeld updated the theory of an electron gas to include the Fermi-Dirac distribution in place of the Maxwell-Boltzmann distribution. Qualitatively the difference between these two is that electrons are now considered to be Fermions and are bound by the Pauli exclusion principle that states only one electron may occupy one energy state at a time in an atom. The thermal properties of metals are outside the scope of this dissertation, but the impact of Fermi-Dirac statistics on the optical properties of metals is explained.

In the Sommerfeld model a single electron is described by a wave function with a specified spin state. The electron is confined to some arbitrary volume by the attraction of the ions, and we can solve the time-independent Schrödinger equation subject to periodic-boundary conditions. [2.3-2.4] This results in the solutions for energy levels given by Eq. 2.13

$$\mathrm{E}\left(\vec{k}\right)=\frac{\hbar^2\vec{k}^2}{2m}=\tfrac{1}{2}m\vec{v}^2 \tag{2.13}$$

where $\hbar$ is Planck's constant, $\boldsymbol{k}$ is the electron's wave vector, m is still the standard mass of the electron, and $\boldsymbol{v}$ is the electron's velocity. The periodic-boundary conditions result

in a quantization condition such that the arbitrary volume must be filled with an integer number of wave vectors. This may be referred to as a *k*-space, and it has some volume in which a finite number of *k*-values are allowed. If we assume that the electrons do not interact with each other then we can use the solution in Eq. 2.13 and populate our *k*-space with *N* electrons according to the rules for Fermions. Hence for each wave vector there are two electrons – one for each spin state. *N* is a large number and the occupied region of *k*-space can effectively be considered to be a sphere in the Sommerfeld model. The occupied region of *k*-space has a radius called the Fermi wave vector k_F, and the surface of the sphere (or Fermi surface) separates the occupied from the unoccupied states. The Fermi wave vector has units of inverse distance (usually $Å^{-1}$) and will depend upon the radius of a sphere r_s whose volume is equal to the volume of a conduction electron. The radius varies depending upon the metallic atom, but is usually between 1 and 3 Å and can be found in references such as [2.3-2.4]. The Fermi wave vector can be calculated using Eq. 2.14. [2.3]

$$k_F = \frac{(9\pi)^{1/3}}{r_s} \tag{2.14}$$

By plugging Eq. 2.14 into 2.13 we can now calculate the Fermi velocity for a metal according to the Sommerfeld model in Eq. 15.

$$v_F = \frac{\hbar k_F}{m} \tag{2.15}$$

The Fermi velocity calculated using Eq. 2.15 is on the order of 10^6 m/s, and v_F is an order of magnitude larger the electron's velocity would have been according to the Maxwell-Boltzmann distribution at room temperature.

The Fermi velocity can be taken to be the average speed of a conduction electron in a metal. Since we can measure τ using Eq. 2.3, we can now determine the electronic mean free path of free electrons in a particular model. This concept is critical to understanding the anomalous skin effect in chapter 3, and the Sommerfeld model is essential to correctly calculate λ_{mfp} according to Eq. 2.16.

$$\lambda_{mfp} = v_F \times \tau \tag{2.16}$$

It is worth noting that the Fermi velocity is a property of the atom, and thus must remain constant regardless of how we might process the metal and change the physical structure. The scattering time however depends entirely on the physical structure of the metal, and although this is not assumed in either the Drude or Sommerfeld models, it will be shown in chapter 3. One limitation of the Sommerfeld model is that we are limited to spherical Fermi surfaces. If we were to develop a more sophisticated approach using something like the tight-binding model we would find that the Fermi surface may not be very spherical at all as occurs with W [2.5] and Ru [2.6]. In this case we must treat the Fermi velocity as a vector, and it can vary greatly depending upon crystallographic direction. However this is only relevant for single crystals, or else metal films with grains much larger than λ_{mfp}. This dissertation will mostly be concerned with polycrystalline metallic thin films.

2.2 Surface Plasmon Polaritons

A closely related field to metamaterials that has been simultaneously developed is the study and applications of surface plasmon polaritons (SPP). In the past few years these two fields have merged, and metamaterials are now frequently discussed in terms of plasmonics. The goal of this chapter is explain the physics necessary to understand the rest of this dissertation, but also for the reader to be able to read the literature on metamaterials. This requires some explanation of the relationship between SPPs and metamaterials.

The study of plasmonics does not have much to do with the actual plasma state, but rather in the sense that we can treat a metal as a plasma according to the Drude and Sommerfeld models. The word plasmon refers to a quanta of plasma oscillation which is analogous to the relationship between photons and radiation or phonons and vibration. Despite the basic principal of quantizing plasma oscillations, the equations describing the wave vectors and propagation constants associated with SPPs are derived from Maxwell's equations. Thus any plasmonic experiment can be designed using standard electromagnetic simulation tools such as HFSS. Plasmons are mathematically treated as waves, and the utility of the plasmonic quasi-particle concept is just to create a picture to help understand how plasmons interact with other particles such as photons or phonons. This picture allows us to imagine the interaction between a plasmon and a phonon as two

coupled harmonic oscillators (mass on a spring) driven by an external force. This will be shown to be an accurate picture in chapter 5.[†]

There are both bulk and surface plasmons (SP). Bulk plasmons occur at or above the plasma frequency when the field can now propagate through the metal. Below the plasma frequency the field can not penetrate beyond a skin depth into the metal, and so the only allowed plasmon modes are confined to the surface, or more specifically at the interface between a metal and a dielectric. A plasmon mode on its own is not very useful, and it needs to couple to radiation to become useful. A plasmon coupled to a photon is called a plasmon polariton. In general a polariton is a quasi-particle consisting of two coupled particles which could also be a photon coupled to a phonon. If radiation is incident on a continuous metallic thin film SPs are not excited. Since SPs are confined modes there will always be a mismatch between the wave vectors of freely propagating radiation and the SP. This is illustrated by the dispersion relationship for a SP which depends upon the SP wave vector (k_{SP}) in Eq. 2.17. [2.7]

$$k_{SP} = k_0 \sqrt{\frac{\varepsilon_d \varepsilon_m}{\varepsilon_d + \varepsilon_m}} = k'_{SP} + ik''_{SP} \tag{2.17}$$

In Eq. 2.17 ε_d is the frequency dependent permittivity of the dielectric, ε_m is complex Drude model permittivity from Eqs. 2.10 to 2.11, and k_0 is the free space wave vector. The real part of k_{SP} is the propagation term and the imaginary term describes the loss of the mode. The SP propagation length L_P is given by Eq. 2.18.

[†] We could make an equivalent picture by discussing metamaterials in terms of surface currents and circuit analog models, but this would be less elegant, and would receive less attention in the literature. By the same token we could call a metamaterial a frequency selective surface, but the chances of getting a paper on circuit analog models and frequency selective surfaces published in the Physical Review are near zero. A paper on plasmon-phonon coupling in metamaterials has more appeal.

$$L_P = \frac{1}{2k''_{SP}} \tag{2.18}$$

We can use the real part of Eq. 2.17 along with Eq. 2.11 to generate surface plasmon dispersion relationships varying with dielectric permittivity shown in Fig. 4. To calculate ε_m the DC conductivity and scattering time of bulk Ag is used in Eq. 2.11, and non-Drude phenomena are ignored for the time being. The values used for ε_d are assumed to be real and constant with respect to frequency for the time being as well.

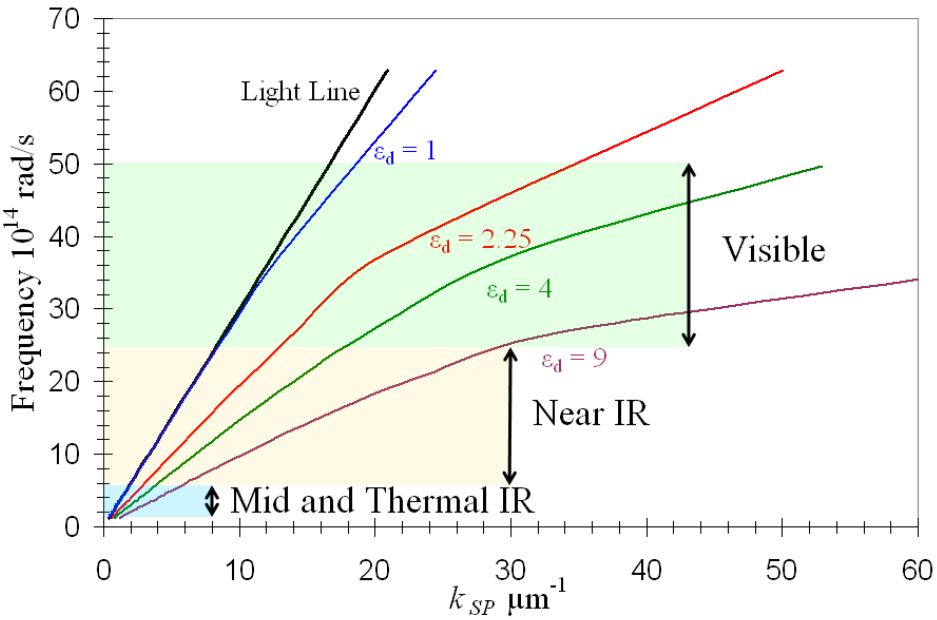

Figure 4: Surface plasmon dispersion relationship for different dielectric permittivities

Figure 4 shows that k_{SP} always lies beneath the light line – that is the line for which the frequency is equal to the free space wave vector. This indicates that the SPs are confined modes, and in order for radiation to couple to SPs the difference in wave vector must be made up. However once radiation has coupled to an SP the large difference in wave vector will allow the mode to propagate without leaking or re-radiating – hence confined to the surface. Several methods have been developed over the years to couple radiation

into SPs to launch SPP modes including prism coupling [2.8-2.9], near-field scattering from a sub-wavelength feature [2.10-2.11], and diffraction grating coupling [2.12]. Figure 4 also labels the bands corresponding to visible, near IR, and the mid to thermal IR frequency bands. As the frequency decreases from ω_P the confinement of the SP decreases as evidenced by the decreasing difference in wave vector between k_{SP} and the light line. Yet as the frequency decreases the dynamic conductivity begins to favor longer propagation distances. This may be shown using Eq. 2.17 and Eq. 2.11. With these two competing factors a sweet spot occurs in the visible to near IR bands where the SP modes is still strongly confined and propagation lengths are long enough to match component sizes.

Because of this propagation length to confinement tradeoff, the applications for SPP technologies have been primarily in the visible band for applications including nano-scale waveguiding [2.13], enhanced transmission through lossy media [2.14], biological detection using nanoparticles [2.15], and for high resolution lithography [2.16]. At sufficiently low frequencies in the IR or THz bands, SPPs lose confinement as the penetration length into the metal of the incident field increases relative to the wavelength. This can also be seen in Fig. 4 with the small contrast in wave vector between k_{SP} and the light line. During the same period of time that SPP modes were being studied in the visible and near IR, metamaterials were being developed first in the radio frequency band, and then pushed to increasingly higher frequencies. Since both metamaterials and SPPs involve sub-wavelength metallic elements excited by incident radiation it would seem that they have a lot in common. Once both metamaterials and SPP structured

surfaces were being fabricated for use in the near IR it made sense to connect these similar fields of study.

The connection between SPPs and metamaterials began by showing that surfaces structured with sub-wavelength dimensions could mimic SPP behavior and dispersion relationships. Pendry referred to this as a "spoof" SPP. [2.17] Another novel feature of spoof SPP modes is that they do not have the low frequency confinement limitations that existed for the continuous metal film. Spoof SPP modes have been shown to occur in the THz band [2.18], so IR metamaterials may be said to support spoof SPP modes. While these spoof SPP modes were originally demonstrated with metal structures that were thick compared to the wavelength, more recent results showed that spoof SPPs can occur in metamaterial elements that are thin compared to the wavelength which includes the metamaterials fabricated in this dissertation. [2.19]

Since spoof SPP modes essentially behave like standard SPP modes they still need to be launched by prism coupling or some other means to achieve a significant propagation distance. The design goal in this dissertation is fundamentally different in that we are interested in constructing resonant elements that we can use to engineer the optical properties of a surface. Radiation that is incident on a metamaterial normal to the elements, or incident at some grazing angle, can excite plasmonic-cavity modes. These are similar to spoof SPPs except that they have been confined not only to the surface, but are further confined to oscillate on a single element without strongly coupling to nearest neighbors. Metamaterials have been shown to support trapped plasmonic-cavity modes

confined to a single element. [2.20] In chapter 5 this dissertation extends the theory to show that plasmonic-cavity modes in standard IR metamaterials exist, and that they can strongly couple to transverse-optical-phonon modes.

At this point we have considered how the Drude and Sommerfeld models treat thin metallic films as an electron gas or plasma. It was next shown how the SPP theory was developed beginning with the concept of a metal as a plasma, and that plasmonic theory may be used to explain the behavior of IR metamaterial elements. Metamaterials may be considered to be a branch on the larger plasmonics tree that contains a diverse group of experimental work and many applications.

2.3 Metamaterials

Much of the recent interest in metamaterials is due to the possibility of creating a negative refractive index metamaterial (NIM). The justifications for NIMs are presented based on the arguments represented in the literature. It will be discussed how the optical properties of metals limit the use of NIM. More practical applications of IR metamaterials will then be discussed.

In any normal dielectric material incident radiation is refracted along the direction given by Snell's law as shown in Fig 5.

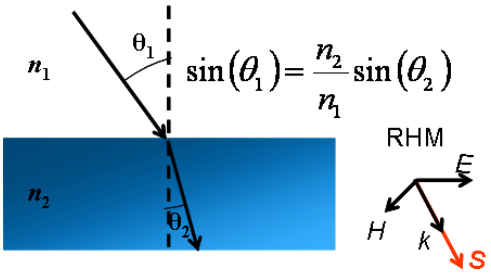

Figure 5: Refraction in a normal right handed material (RHM). H is in the direction out of the plane of the page.

The index of refraction is determined by the permittivity ε and permeability μ as shown in Eq. 2.19 where loss (and hence the imaginary components) is ignored for the moment.

$$n = \sqrt{\varepsilon\mu} \tag{2.19}$$

The rays in Fig. 5 correspond to the direction of the propagating electromagnetic wave corresponding to the wave vector ***k***. The time average of the Poynting vector ***S***, or the direction of energy flux, has direction given by the cross product of the electric ***E*** and magnetic fields ***H***. In a normal material the electric field, magnetic field, and the wave vector form a right-handed set, and the direction of propagation (wave vector) is parallel to the Poynting vector. We may call this a right-handed material (RHM). In 1968 Veselago argued that if both ε and μ were simultaneously changed to negative sign then a left handed material (LHM) would result [2.21]. From Eq. 2.19 the sign of n is ambiguous since both positive and negative roots exist whenever ε and μ have the same sign. Veselago's derivation begins with Maxwell's equations in Eq. 2.20.

$$\begin{aligned} &\vec{\nabla}\times\vec{E} = -\frac{\partial\vec{B}}{\partial t}, \vec{\nabla}\times\vec{H} = \frac{\partial\vec{D}}{\partial t} \\ &\vec{B} = \mu\vec{H}, \vec{D} = \varepsilon\vec{E} \end{aligned} \tag{2.20}$$

We assume Cartesian coordinates such that ***H*** is in the positive x direction and ***E*** is in the positive y direction. If the fields are associated with a monochromatic plane wave then

each will equal to a vector coefficient with the term exp(ikz-ωt). If we substitute fields of this form into Eq. 2.20 we come up with Eq. 2.21 which describes the direction of ***k*** with respect to the sign of ε and μ.

$$\vec{k} \times \vec{E} = \omega\mu\vec{H}$$
$$\vec{k} \times \vec{H} = -\omega\varepsilon\vec{E} \tag{2.21}$$

If the sign of ε and μ are both positive then Eq. 2.21 describes an RHM and ***k*** is in the negative z direction. If the sign of ε and μ are both negative then Eq. 2.21 describes an LHM and ***k*** is now in the positive z direction. In either case the direction of the Poynting vector is still the cross product of ***E*** and ***H*** and is thus in the negative z direction. Therefore in an LHM, which is also sometimes referred to as a double-negative material, the energy flux and propagation of the wave are in opposite directions. We have a backwards propagating wave. Based on the definition of the wave vector in terms of the index of refraction in Eq. 2.22, Veselago concluded that *n* had the negative root from Eq. 2.18 based on the direction of ***k***.

$$\vec{k} = \frac{\omega}{c} n \tag{2.22}$$

This situation is shown schematically in Fig. 6.

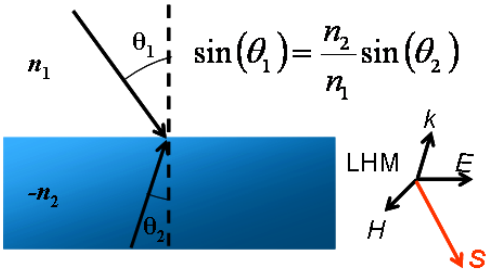

Figure 6: Refraction in a left handed material (LHM). H is in the direction out of the plane of the page.

Veselago's theory of an LHM implies a situation which appears to violate causality, and it is as if the backwards propagating wave were originating in the material before even reaching the material. This has been explained by saying that since the LHM is electrically thin the interaction is entirely within the near fields where superluminal waves may be said to "surf on a back ground of *c* travelling waves." [2.22] Superluminal propagation is well beyond the scope of this dissertation.

It is one thing to mathematically describe the properties of a material with double-negative optical constants, but such materials do not exist in nature. Metals have negative ε below the plasma frequency, but negative μ requires a magnetic resonance which does not normally occur at high frequencies. In fact μ for metals in high frequency range can universally just be equated to unity and is generally ignored. Since a real material that has a simultaneous permittivity and permeability resonance at high frequency would likely have loss we need to re-write the condition for an LHM in terms of complex permittivity and permeability in Eq. 2.23 [2.23].

$$\varepsilon'\mu''+\varepsilon''\mu'<0 \tag{2.23}$$

The challenge is then to design a material that has a magnetic resonance at high frequency. In 1999 Pendry showed mathematically that two concentric cylinders, split at opposite ends, and made of nonmagnetic conducting sheets could support an induction current along the surface of the sheets. Pendry predicted that the gap in the conductor would reflect the current due to the resulting electric fields and thus set-up a rotary current mode which would could be described as having a restoring force and thus a magnetic resonance. [2.24]

The effective permeability of a metamaterial is then typically written as Eq. 2.24 [2.25]

$$\mu = 1 - \frac{f'\omega^2}{\omega^2 - \omega_0{}^2 + i\Gamma\omega} \tag{2.24}$$

where *f'* is the oscillator strength, ω_0 is the resonant frequency associated with the magnetic restoring force, and Γ is the damping rate of the current mode. It is interesting to note that the ω_0 of the magnetic resonance, defined in Eq. 2.25, is related to the series summation of the gap inductance L_g and the inertial inductance L_i which is related to metallic absorption loss at high frequencies.

$$\omega_0 = \sqrt{\frac{1}{LC}} = \sqrt{\frac{1}{(L_g + L_i)C}} \tag{2.25}$$

In chapter 5 we will see how the gap and fringing field capacitance terms affect the permittivity resonance. The permeability resonance is more strongly tied to effects on the element's inductance.

Split-ring resonator (SRR) elements were subsequently fabricated and tested by Smith in 2001 at 10 GHz demonstrating the existence of NIM metamaterials for the first time. [2.26-2.27] Smith's experiment Showed that a 3-D array of SRR elements refracted an incident beam at a negative angle compared to when the same experiment was done using a Teflon block. The demonstration of a NIM launched the modern field of metamaterial research and began a race to build NIM materials at increasing higher frequencies into the visible band. The most obvious way to accomplish this would be to scale Smith's design down to match shorter wavelengths, but this results in SRR elements that are less than 1 μm across and around 100 nm wide in the thermal IR and another order of magnitude

smaller in the visible. This pushes the limits of E-beam lithography for a single planar layer, and it is a major challenge to fabricate a truly 3-D bulk metamaterial to replicate Smith's work at 10 GHz. In the IR and visible, metamaterials generally do not have more than a two layer stack of elements and are really more like metafilms. One recent exception that has received a great deal of attention are the so called 'fish net' metamaterials that consist of a series of thin film layers with a net pattern etched after deposition [2.28], but the fish nets are still not a bulk material. Thin optical frequency metamaterials present several disadvantages; metafilms have limited performance for off-normal angles of incidence, and they exhibit thin film interference and cavity modes as opposed to obeying Snell's law. A thin film can not be tested using Snell's law to determine its index of refraction as Smith did with the 3-D 10 GHz design. To demonstrate negative refractive index in the IR and visible requires a method that can determine the optical properties of a thin film rather than a bulk material.

As discussed in chapter 1, the principal tool for testing thin metamaterials in the IR is FTIR spectroscopy. Similar spectroscopy techniques are available to measure the power transmitted and reflected by a metamaterial. Ellipsometry is not an effective tool for metamaterial measurements because the surfaces are non-uniform, and ellipsometry is best suited for truly homogeneous thin films without variations in composition or thickness. It is then a matter of determining how measurements of spectral power can be used to calculate the effective refractive index of a metamaterial. Mathematically this requires that we have knowledge of the fields associated with reflection and transmission rather than just the power, and thus we need to know the complex transmission and

reflection coefficients t and r defined by Eq. 2.26 in terms of the transmitted and reflected power T and R and phase φ_T and φ_R.

$$r = \sqrt{R}\exp(i\varphi_R)$$
$$t = \sqrt{T}\exp(i\varphi_T) \tag{2.26}$$

All of the values in Eq. 2.26 may be taken to be functions of frequency. Reflected and transmitted phase can be determined in several ways. Relative phase differences can be measured directly using an interference experiment as is discussed in chapter 6 using an interferometer that functions at a single wavelength, or the transmitted and reflected phase may be measured as a function of frequency for a metamaterial using a phase mask [2.29]. Another method is to use the Kramers-Kronig relations to extract phase information based on the power measurement as is further explained in Ref. 2.30, but there are some limitations to this approach. A third approach, and the one most commonly used, is to simply measure the reflected and transmitted power and then rely on a simulation tool such as HFSS to calculate the phase. If the FTIR measurements agree with the simulated power spectrums, then it is fair to assume the simulated spectral phase is accurate. Thus the only essential measurement necessary to evaluate a metamaterial is the FTIR measurement. Equation 2.26 may then be used to calculate the effective permittivity and permeability of a metamaterial.

Equation 2.19 gave the relationship between the index of refraction and the permittivity and permeability. We need a second equation to determine ε and μ separately. The material impedance z may also be used and is given in terms of ε and μ in Eq. 2.27. We should assume that n, z, ε, and μ are all complex numbers.

$$z = \sqrt{\mu / \varepsilon} \tag{2.27}$$

At this point an assumption must be made that the metamaterial can be mathematically treated as a homogeneous slab of material with thickness *d* given in principle by the sum of the element thickness and any other thin film layers that comprise the metamaterial. The choice of *d* in the literature is not always clear and can be a source of ambiguity in the analysis. Since metamaterial elements are small compared to the wavelength there is cause to accept the assumption that a metamaterial can be treated as optically homogeneous. Given this assumption, equations for *n* and *z* can be written in terms of *r* and *t* as shown in Eqs. 2.28 and 2.29 [2.31].

$$\cos(nkd) = \frac{\exp(-ikd)}{2t}\left[1 - \left(r^2 - t\exp(ikd)\right)^2\right] \tag{2.28}$$

$$z = \pm\sqrt{\frac{\left((1+r)^2 - (t\exp(ikd))^2\right)}{(1-r)^2 - (t\exp(ikd))^2}} \tag{2.29}$$

In order to avoid ambiguities in the sign of *n*, reality conditions need to be imposed on Eq. 2.28 and 2.29 so that the correct root is taken. In a passive material the real part of *z* and the imaginary part of *n* must be greater than zero. When the roots are taken properly it is possible to show that the real part of *n* is less than zero when *r* and *t* are measured for a NIM.

Over the past ten years there have been many examples of NIMs in the visible and IR, and the possibility of using metamaterials to bend rays around an object to make it "invisible" has generated considerable excitement and pubic attention to so-called metamaterial-cloaking devices. [2.32] However metamaterial cloaking is limited by the

optical properties of metals. To date metamaterials have required metallic elements in order to generate the artificial magnetic response given by Eq. 2.24. When realistic permittivity at optical frequencies is used the imaginary part of n, i.e. the extinction coefficient, in Eq. 2.28 becomes large. The high degree of absorption loss associated with metamaterials at optical frequencies means that they do not so much make things invisible as make them look like a black hole – which is not particularly useful. Secondly the requirement that μ be less than zero will only occur in Eq. 2.24 for the case of anomalous dispersion which requires a resonance that is both strong and narrow bandwidth. Given this limitation it is only possible to cloak an object over a small frequency range, and given the loss it would not be possible to stack metamaterials for different frequencies together. NIM and cloaking get much of the attention but have little of the utility that is actually possible with metamaterials.

Metamaterials can be used to engineer ε and μ for many purposes besides making both quantities simultaneously negative. The use of tunable metamaterials, as discussed in chapter 6 of this dissertation, combined with the artificial magnetic response may be used for optical data storage devices [2.33]. As supplies of magnetic elements dwindle and their cost increases, artificial magnetism from metamaterials may become a viable alternative. In the IR we are not usually concerned with controlling μ but rather tailoring the spectral features of a surface as discussed in chapters 4 and 5. Essentially this means that we are altering the effective permittivity of the surface, but in this dissertation measured values will be left in terms of the measured spectral quantities r and t rather than converting to n and z. This also avoids some of the ambiguities that were discussed

in the derivation of Eqs. 2.28 and 2.29. Some good examples of practical metamaterial work in the IR include the control of spectral transmission, [2.34] reflection, [2.35] absorption, [2.36] emission, [2.37-2.38] reflected phase, [2.39] emitted phase, [2.40] as broad-band wave plates, [2.41] and for molecular detection. [2.42]

CHAPTER 3: ELECTRONIC TRANSPORT IN METALLIC THIN FILMS AT INFRARED FREQUENCIES

So far it has been shown that the optical properties of metals may be modeled as an electron gas, or plasma, according to the Drude and Sommerfeld models. It is well known that deviations from the Drude model occur in the visible band when photons are sufficiently energetic to excite interband transitions, but IR photons have too little energy for such events to occur. This raises the question of whether or not the Drude and Sommerfeld models are sufficient to fully describe the optical properties of metals in the IR band. Based on Eq. 2.11 it is clear that anything that affects the DC conductivity will also change the optical properties of the metal. According to a strict interpretation of the Drude or Sommerfeld models only scattering from the ion cores occur. However real metals follow Matthiessen's rule which states that electrical resistivity is the result of independent scattering processes which sum together to yield the total resistivity. Instead of simply scattering from ion cores, electrons in real metals scatter from phonons, impurities, and defects in the crystal lattice. Since an impurity essentially creates a type of defect depending upon the solid solubility of the two species, we may put contributions from defects and impurities together for argument's sake. As a metal becomes more pure and crystallographically perfect DC resistivity decreases, and as the phonon population decreases with temperature the DC resistivity decreases as well. In this chapter we will consider how changes in the DC conductivity based on Matthiessen's rule affect the dynamic conductivity and loss tangent at IR frequencies. These experiments will show that deviations in the Drude and Sommerfeld models occur at IR frequencies due to the anomalous skin effect.

3.1 Theory of the Anomalous Skin Effect

Matthiessen's rule applies to both bulk and thin film metals. Typically when considering the optical properties of thin metallic films to be used in SPP and metamaterial applications only the physical structure of the interface is considered. This assumption is made because SP modes are confined at the surface. Previous research has found that variation of the surface morphology of metal films has altered the dynamic conductivity in the IR for Fe [3.1] as well as Cu films [3.2]. However in the IR, confinement of all SP modes decreases with frequency relative to increasing skin depth. The skin depth δ is the distance at which an incident electromagnetic wave's electric field is able to penetrate into the metal. This is given by Eq. 3.1 in terms of the extinction coefficient *k*.

$$\delta = \frac{\lambda}{2\pi k} = \frac{c}{\omega k} \tag{3.1}$$

We may then consider that within the skin depth phonons and impurities will affect plasmon modes in ways not considered by the Drude or Sommerfeld model. These skin effects have largely been ignored in the literature on SPPs and metamaterials.

Instead of limiting the investigation to the surface of the film, the influence of the electronic mean free path within the film on dynamic conductivity may also be considered. According to the Sommerfeld model, the dynamic conductivity should depend upon the relaxation time. The relaxation time is defined as the ratio of the electronic mean free path (λ_{mfp}) to the Fermi velocity. Modifying the electronic mean free path by adding impurities, or decreasing the temperature, changes the relaxation time of the film and alters the dynamic conductivity within the skin depth while the surface

scattering contribution may be unchanged. For free electrons in noble metals the relaxation time may be approximated within the skin depth as being isotropic. In the IR the skin depth encompasses a depth of around 10 nm. The Sommerfeld model may be used to calculate the effect of changing relaxation time on dynamic conductivity in Au and Cu films deposited by physical vapor deposition (PVD) tools. The discussion in this chapter has been limited to noble metals so as to avoid effects inconsistent with the Drude model that occur in transition metals for which the electronic mean free path is less than or equal to the Fermi wavelength. In this limit transport must be examined using quantum mechanical models, and relaxation time effects may no longer be dominant. [3.3]

The real part of the dynamic conductivity from Eq. 2.11 may be further rewritten to expand the DC conductivity in terms of relaxation time. This is shown in Eq. 3.2 where *N* is the density of valence electrons, e is the charge on the electron, and m* is the effective mass. Eq. 3.2 assumes that the DC relaxation time is equivalent to the dynamic relaxation time. We will investigate the validity of this assumption.

$$\sigma'(\omega) = \frac{ne^2\tau}{m^*(1+(\omega\tau)^2)} \tag{3.2}$$

It is evident from Eq. 3.2 that in the case that the ωτ product is much greater than unity the dynamic conductivity will be inversely proportional to the relaxation time. In this case dynamic conductivity decreases as the mean free path increases. Conversely, if the mean free path is decreased by impurity scattering, then the dynamic conductivity should increase. The maximum value for dynamic conductivity in Eq. 3.2 occurs when the ωτ product is equal to unity. In the RF band a large τ is required to satisfy this condition, but

in the IR band pure metal films have ωτ products that are much greater than unity, so τ must be decreased to maximize the real part of dynamic conductivity in the IR band.

Although the real part of dynamic conductivity may describe ohmic, or electrical, loss in high-frequency-electron transport, the loss tangent describes the optical absorption loss suffered by the component of the incident electromagnetic-wave vector normal to the surface as described in chapter 2.1. We write loss tangent as *loss*(δ) which emphasizes that the loss tangent describes the radiation lost to surface-propagating modes within the skin depth δ. Similarly to Eq. 3.2 we can write Eq. 3.3 for *loss*(δ) in terms of the relaxation time using Eq. 2.11.

$$loss(\delta) \equiv \frac{\varepsilon_r''}{\varepsilon_r'} = \left(\omega \frac{\varepsilon_0}{\sigma_0} \left(1 + (\omega\tau)^2\right) - \omega\tau \right)^{-1} \approx -\frac{1}{\omega\tau} \tag{3.3}$$

This demonstrates that as the ωτ product increases *loss*(δ) linearly decreases. Anything we gain in ohmic loss by decreasing ωτ in Eq. 3.2 is made up for by increases in absorption loss. It would also make sense that an increase in *loss*(δ) due to decreasing τ would result in an increase in the skin depth, and hence an increase in the loss associated with the field leaking into the metal and thus losing surface confinement. If we write δ in terms of relaxation time it can be shown that this is the case. This can be done by combining Eq. 2.11 with Eq. 3.1 resulting in Eq. 3.4.

$$\delta = \left(1 + (\omega\tau)^2\right) \frac{2nc\varepsilon_0}{\sigma_0} \tag{3.4}$$

The *n* in Eq. 3.4 is the index of refraction (or real part of complex index). Since *n* and σ_0 also depend upon τ we must substitute a longer expression for *n* in terms of τ into Eq. 3.4.

It is easier to just plot δ as a function of frequency for various relaxation times which is shown in Fig. 7 based on calculations made using Eq. 2.11 and 3.1.

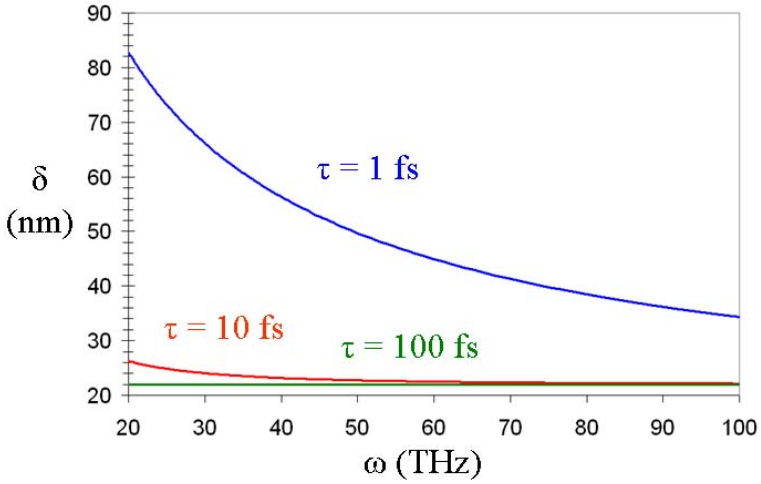

Figure 7: Skin depth δ(ω) for a range of relaxation times τ.

Figure 7 shows that if τ is decreased from 10 fs to 1 fs, and thus made small compared to ω^{-1}, then δ increases significantly resulting in weak surface confinement. When τ is greater than or equal to ω^{-1} between 10 and 100 fs there is not a strong dependence of δ on τ. We can also see in Eq. 3.4 that δ is inversely proportional to the DC conductivity, which is why SPP experiments always use Ag. High DC conductivity in Ag decreases the skin depth and promotes surface confinement.

Eqs. 3.3 and 3.4 point out the fundamental physical difference between so-called surface currents on radio frequency antennas and SPs on IR to visible frequency metamaterials and related structures. For an antenna one only needs to be concerned with ohmic loss because $\omega\tau << 1$ and confinement is very weak, but for SPs in the IR and visible $\omega\tau > 1$ and now current is localized to the surface, but ohmic loss is high. The high ohmic loss means that in the IR and visible we need to work hard to maintain surface confinement.

Confinement allows us to take advantage of plasmonic modes as opposed to the normal kinds of current modes that would occur in a circuit at low frequencies. This is not to say that plasmonic modes could not be equivalently modeled as circuits, but just that we are dealing with two different flavors of electronic transport. At high frequency both the real part of dynamic conductivity and *loss*(δ) should be considered.

This dissertation focuses on the IR. In the IR we have both high ohmic loss, and only moderate confinement of SPs. We are still primarily interested in the SP flavor of current (plasma oscillations), but we must take into account that these will be leaky SP modes. The non-Drude model effect of weak confinement in SP modes is manifest as the anomalous skin effect.[‡]

As plasmonic modes in the IR become leaky electrons within the skin depth of the metal are affected by dynamic conductivity. Within the skin depth electrons are subject to the condition that only those electrons which travel a mean free path within the skin layer may be considered carriers in dynamic conductivity. When skin depth is less than or nearly equal to the mean-free path electrons with trajectories oriented normal to the surface will then no longer participate in dynamic conductivity. [3.4] Possible electron trajectories within the skin depth are illustrated in Fig. 8. When $\delta > \lambda_{mfp}$, as shown on the left side of Fig. 8, the short λ_{mfp} indicates that τ is also short which would result from the electron encountering a high density of scattering events. The density of scattering

[‡] Note to Dr. Boreman: Dr. Munk always said that FSS like the meanderlines should not work in the IR because of ohmic loss, but somehow they did anyway. I propose that this is because we were not exciting the sorts of current modes he was thinking of, but rather plasmonic cavity modes. These are very similar, and if you trick PMM by ignoring dynamic conductivity as Jeff did, then everything just scales with frequency. Anyway the good news is stuff works.

events does not depend upon the excited electron's trajectory, but regardless of the direction it scatters in, the electron will not get far because of the short λ_{mfp}. From Fig. 7 we also know that δ is long in this case.

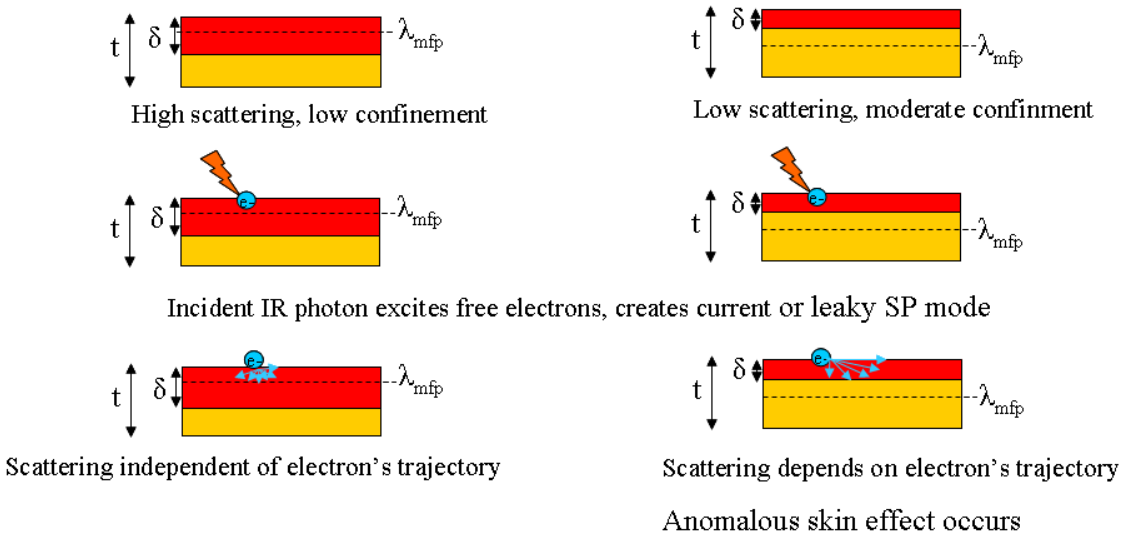

Figure 8: Left: a high scattering, low surface confinement situation in which $\tau < \omega^{-1}$. Right: a low scattering, moderate (in the IR) surface confinement situation in which $\tau > \omega^{-1}$. t is the thickness of the metallic film. Note an IR photon can only excite an SP

When $\delta < \lambda_{mfp}$, as shown on the right side of Fig. 8, the long λ_{mfp} indicates that τ is also long which would result from the electron encountering a lower density of scattering events. The density of scattering events now depends upon electron's trajectory. If the trajectory is normal to the surface the electron will not travel far as it is limited by the small skin depth, and the electron will cease to participate in a current mode once it is no longer driven by the electric field. If the excited electron's trajectory is parallel to the surface then the electric field can drive the current mode, and the transport of an individual electron in a current mode between is only limited by the length of λ_{mfp}. Only a subgroup of the total electrons excited will realize normal transport with scattering determined by λ_{mfp}. The lower concentration of carriers will result in a lower dynamic

conductivity than the prediction of the Sommerfeld model. This is called the anomalous skin effect.

Excited electrons with trajectories parallel to the surface were termed 'effective electrons' by Pippard [3.5] and used to explain the anomalous skin effect at radio wave frequencies in noble metals at cryogenic temperatures. The difference between an effective and an ineffective electron is illustrated in Fig. 9.

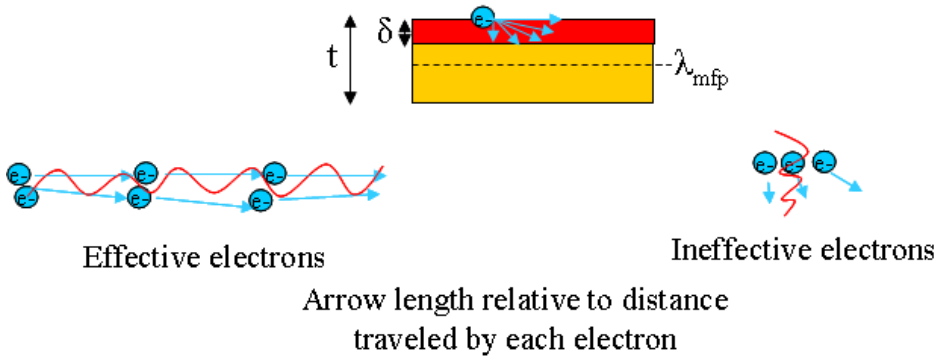

Figure 9: Effective electrons with modes propagating parallel to the surface, ineffective electrons travel normal to the surface where outside the skin depth there is no electric field to generate a current density wave.

In modern language we can say that effective electrons are those confined to the surface and thus a current density wave consisting of effective electrons is an SP mode. As was discussed in chapter 2.2 portions of the electromagnetic wave that excite SPPs normal to the surface are lost, and we can now say that this is because current modes normal to the surface involve ineffective electrons. It is important to note that the propagation length of the SP mode can be much greater than λ_{mfp}, but the individual electrons in the mode are scattered at intervals of λ_{mfp}. In the Drude or Sommerfeld models we assume that after each scattering event an individual electron starts over and can become either an effective or ineffective electron.

The SP mode will lose its effective electrons along the way as some change direction to become ineffective until reaching the end of its propagation distance. If instead of launching SPP, or spoof SPP, modes through prism coupling or some other means, and we instead have plasmonic-cavity modes on metamaterial elements, then we assume that the same behavior occurs with respect to the anomalous skin effect. Only the propagation of the SP mode has changed. We then consider that all SP modes depend upon the optical properties of the metallic film, and that these properties are invariant regardless of whether the metal is an element supporting some kind of plasmonic-polariton mode, or whether the metal is just a continuous thin film exposed to an incident electromagnetic wave. In either case only some fraction of the total free electron density will consist of effective electrons. In order to accurately understand the optical properties of metallic thin films we must adjust the Sommerfeld model to include the anomalous skin effect.

The fraction of effective electrons may then be derived based on the electron distribution f subject to an incident electric field in the Boltzmann transport equation in Eq. 3.5.

$$\frac{e}{m}\left(\vec{E}+\frac{\vec{v}}{c}\times\vec{H}\right)\bullet\vec{\nabla}_v f+\vec{v}_F\bullet\vec{\nabla}_r f=\frac{f-f_0}{\tau}$$
$$f_0=\frac{1}{e^{E-E_F/kT}+1} \tag{3.5}$$

The unperturbed electron distribution f_0 in Eq. 3.5 is given by the Fermi-Dirac distribution as stipulated by the Sommerfeld model. In Eq. 3.5 $\boldsymbol{v}_F$ is the Fermi velocity of the electron, and c is the speed of light. The Fermi-Dirac distribution in the second half

of Eq. 3.5 depends upon the electron's energy E, the Fermi energy E_F, and the temperature T. Solutions for f can be used to find the current density $\boldsymbol{J}$ and thereby the conductivity as shown in Eq. 3.6.

$$\vec{J} = -2e\left(\frac{m}{h}\right)^3 \int \vec{v} f d\vec{v} = \sigma \vec{E} \tag{3.6}$$

Sondheimer solved Eq. 3.5 for the conditions of the anomalous skin effect where the electric field penetrating into the metal is unknown and thus a trial solution f_1 is used according to the conditions in Eq. 3.7. [3.6]

$$\frac{\partial f_1}{\partial z} + \frac{f_1}{\tau v_{F,z}} = \frac{e}{m v_{F,z}} \frac{\partial f_0}{\partial v_{F,x}} E(z) \tag{3.7}$$

Equation 3.7 assumes Cartesian coordinates in which the z direction is normal to the surface of the metal and the x direction is parallel to the surface. Sondheimer's derivation goes beyond the Sommerfeld model to assume that the Fermi surface is not necessarily a sphere. Thus the components of the Fermi velocity along the x and z directions are not equal. The dependence of the anomalous skin effect on the direction of the Fermi velocity was used to make the first experimental measurements of the Fermi surface of Cu by measuring carrier transport along different orientations of a single crystal [3.7].

Once a solution for the electric field is determined it may be used to solve for f which may then be used to find an expression for the conductivity based on the influence of the anomalous skin effect which is similar to Eq. 2.6, but modified by an effective carrier concentration N_{eff} given by Eq. 3.8.

$$N_{eff} = N\beta\frac{\delta'}{\lambda_{mfp}} = N\frac{1}{\tau}\frac{\beta^{2/3}}{V_F^{2/3}}\sqrt[3]{\frac{2m}{\omega n e^2 \mu_0}} \tag{3.8}$$

In Eq. 3.8 δ' is the effective skin depth based on the solution for the electric field in Eq. 3.7. The ratio of δ' to mean free path determines the effective electron concentration and is given on the right side of the equation. The unit-less constant β is related to surface scattering and is proportional to the mean free path times the ratio of the width of surface features to the depth of surface features [3.8].

If the mean free path is much larger than the skin depth then changes in skin layer scattering will not affect the dynamic conductivity. In this limit the dynamic conductivity is dependent on just the Fermi surface. Thus the surface scattering and current modes will be confined to the surface. However, in the metals used for IR metamaterials the mean free path is reduced due to defects and grain boundaries so this condition will not be met. Even at cryogenic temperatures the mean free path does not become very large compared to skin depth because of the high residual defect scattering present in thin films. In the regime where the mean free path is not much larger than the skin depth, scattering within the skin layer should increase the real part of dynamic conductivity by restoring the normal skin effect and increasing the effective carrier concentration towards its standard value of one free electron per atom. Similarly to the Drude model, the effective electron concentration in Eq. 3.8 is inversely proportional to relaxation time. However there is still the tradeoff between confinement and dynamic conductivity. Generating more effective electrons comes at the expense of lost confinement, and we must then resort to standard current modes that suffer from still appreciable ohmic loss.

Before completing modifications to the Sommerfeld model we should also consider that the relaxation time has been treated to this point as a constant value that may be equated with the DC relaxation time. However, it has been observed experimentally in Ref. [3.9] that the relaxation time tends to vary as a function of frequency according to the form given in Eq. 3.9.

$$\tau(\omega) = \frac{1}{a + b\omega^2}. \tag{3.9}$$

Clearly the constant term *a* in Eq. 3.9 corresponds to the inverse of the DC relaxation time. Several explanations have been given for the quadratic term. In Ref. [3.10] dynamic conductivity is described by a two-carrier model in which the constant term is the DC relaxation time of carriers inside the crystalline grains, and the quadratic term is determined by a second distinct carrier type on the grain boundaries. A second explanation in Ref. [3.11] is that the quadratic term results from electron-electron scattering events that occur in all metals at high frequency and are independent of temperature and crystal defects. To completely describe the behavior of dynamic conductivity in the IR, a frequency-dependent relaxation time should be included in addition to the effective carrier concentration from the anomalous skin effect. Thus the ratio between measured dynamic conductivity and the Drude model, γ(ω), in Eq. 3.10 may be formed by substituting Eq. 3.9 into Eq. 3.8. The validity of this equation may then be proven by comparison to data from dynamic conductivity experiments conducted at different temperatures and degrees of impurity scattering.

$$\frac{\sigma(\omega)_{measured}}{\sigma(\omega)_{Drude}} = \gamma(\omega) = \left(\frac{1}{\tau_{DC}} + b\omega^2\right)\frac{\beta^{2/3}}{V_F^{2/3}}\sqrt[3]{\frac{2m}{\omega n e^2 \mu_0}} \tag{3.10}$$

3.2 Experimental Investigation of the Anomalous Skin Effect

Dynamic conductivity and *loss*(δ) may be determined from the complex refractive index measured by ellipsometry as shown in Eq. 2.11. Ellipsometric measurements are taken by reflecting circularly polarized IR radiation at an oblique angle from a thin film sample, and then measuring the polarization state of the reflected elliptically polarized radiation. In these experiments IR ellipsometry was used as described in chapter 1.2. In addition, the low temperature measurements were taken using a UHV cryostat attachment. Ellipsometry has been found to be a reliable method for measuring the optical properties of metal films in Ref. [3.12-3.13]. When used in FEM simulations, optical constants and corresponding dynamic conductivities from Eq. 2.11 which were obtained via ellipsometry have been found to improve agreement between simulated and measured results for IR frequency selective surfaces [3.14]. Therefore dynamic conductivity and *loss*(δ) measured by ellipsometry can be assumed to predict the performance of IR metamaterials. When multiple transparent layers are present in the sample a model is developed to fit the optical properties and thickness of the layers. For metallic films several skin depths thick, only the metal and any surface oxides are measured, so the model is straightforward. The films discussed in this paper, Au and Cu, did not have any appreciable surface oxide layers. Noise caused by depolarized reflected radiation was low at only 1-5% across the spectrum. Measurements were taken from 2 to 20 μm and at

angles of incidence ranging from 65 to 75 degrees. There were no significant changes in dynamic conductivity with angle of incidence in the Au and Cu films.

The DC electronic transport in the films was characterized using four-point probe measurements. Using the known relationship between DC conductivity and relaxation time as in Eq. 2.3, the DC relaxation time was measured using standard values for the constants N, and m. The effective mass was used for m. A valence of one free electron per atom was assumed to determine carrier concentration, and the effective mass was taken to be 0.99 and 1.49 times the standard electron mass for Cu and Au respectively. [3.15] Measured relaxation times were then used in the Drude model for comparison with ellipsometer measurements. Experiments described in the following section were conducted to alter the relaxation time and measure the resulting change in the dynamic conductivity. For each experiment both ellipsometric and DC electronic transport measurements were made.

3.2.1 Anomalous skin effect measurements

The first experiment was to decrease the relaxation time by increasing the impurity scattering density in a Au-Cu alloy. Compositions of $Au_{75}Cu_{25}$, $Au_{50}Cu_{50}$, and $Au_{25}Cu_{75}$ in atomic percent were used to test a range of relaxation times. Boron was added to an additional alloy at a composition of $Au_{50}Cu_{40}B_{10}$ to further increase scattering. The films were deposited by co-sputtering Au and Cu with deposition rates set relative to the desired composition in a UHV PVD tool. The thicknesses of the films were approximately 100 nm. No thermal processing was performed on the films and the

crystal structure was measured by XRD to be the disordered fcc phase in each case. The films may then be considered to be a random mixture of Au, Cu, or B atoms with no intermetallic phase present. XRD data demonstrating the fcc phase for the $Au_{50}Cu_{50}$ alloy are shown in Fig. 10 and the DC electronic transport measurements for the range of Au-Cu films are in table 1. The increase in DC resistivity in the alloy corresponded to the relaxation time falling to just 14% of the pure Au relaxation time for the $Au_{50}Cu_{50}$ film, and further decreases to 5.7 % for the $Au_{50}Cu_{40}B_{10}$ film. The (111) peak in the XRD data shifted to an intermediate value between that of the pure components, and the broad Lorentzian character of the peak indicated a high defect density consistent with the decreased relaxation time.

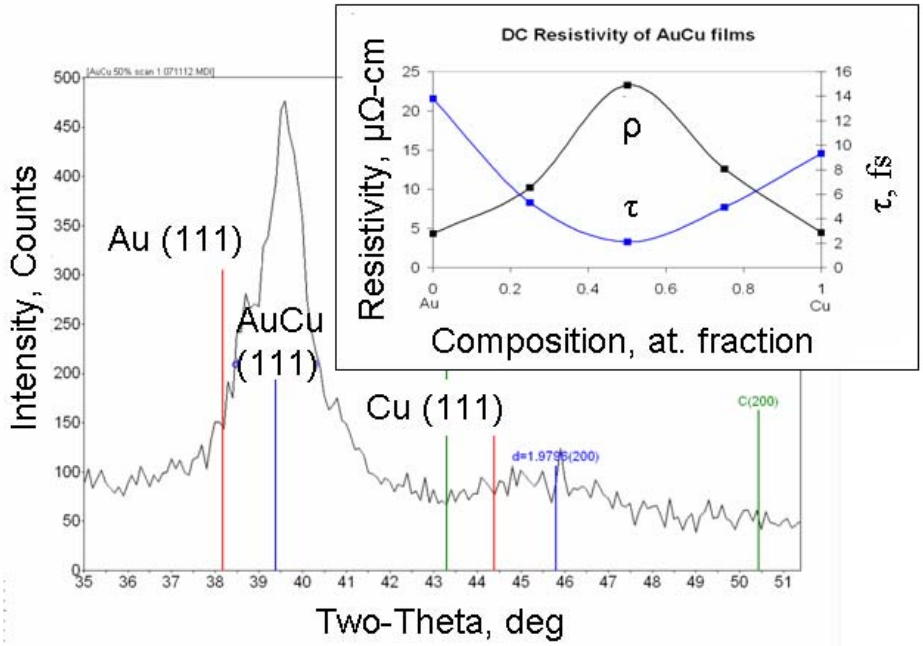

Figure 10: XRD for 100 nm thick, Au50Cu50 alloy.

The second experiment aimed to increase relaxation time by measuring dynamic conductivity at cryogenic temperature. The cryogenic DC electronic transport

measurements were carried out by immersing the samples in liquid helium and then measuring with an in-situ four point probe. Both a Au and Cu sample were measured and the results are given in table 1 where relaxation time has been calculated based on the DC resistivity.

Table 1: DC electronic transport measurements including maximum and minimum $\omega\tau$ products for IR band.

Metal	ρDC, μΩ-cm	τ, fs	ωτ, λ = 20 μm	ωτ, λ = 2 μm
Au 295 K	4.21	13.8	1.30	13.0
Cu 295 K	4.48	9.33	0.879	8.79
Cu annealed 295 K	1.97	25.0	2.36	23.6
Au ~4 K	1.21	50.0	4.71	47.1
Cu annealed ~4 K	0.198	304	28.6	286
$Au_{50}Cu_{50}$ 295 K	23.3	2.12	0.200	2.00
$Au_{75}Cu_{25}$ 295 K	10.2	5.31	0.500	5.00
$Au_{25}Cu_{75}$ 295 K	12.6	4.93	0.464	4.64
$Au_{50}Cu_{40}B_{10}$ 295 K	71.7	0.862	0.0812	0.812

The increase in relaxation time is a factor of 6 larger for the Cu film compared to the Au film because the Cu film was annealed at 400 C for 30 minutes. The heat treatment decreased the defect density in the Cu film thereby reducing the residual resistivity when the phonon contribution to resistivity was removed at low temperature. The resistivity decrease is comparable to those previously observed in similar films. [3.16]

Contrary to DC conductivity results, the increase in impurity scattering in the $Au_{50}Cu_{50}$ film was found to result in larger dynamic conductivity compared to the pure components

as shown in Fig. 11. When the product of the frequency and relaxation time, ωτ, for $Au_{50}Cu_{50}$ was equal to unity at a wavelength of 4 μm, the $Au_{50}Cu_{50}$ alloy's dynamic conductivity was greater that of Cu by 195% and of Au by 260%. At shorter wavelengths the dynamic conductivity of the alloy continued to increase relative to the pure components. At sufficiently long wavelengths, the pure components had a higher conductivity than $Au_{50}Cu_{50}$ once the ωτ product was far enough below unity. This occurs when the product is equal to 0.33. This counterintuitive result of increased conductivity with decreased electronic mean free path is in qualitative agreement with the Drude model.

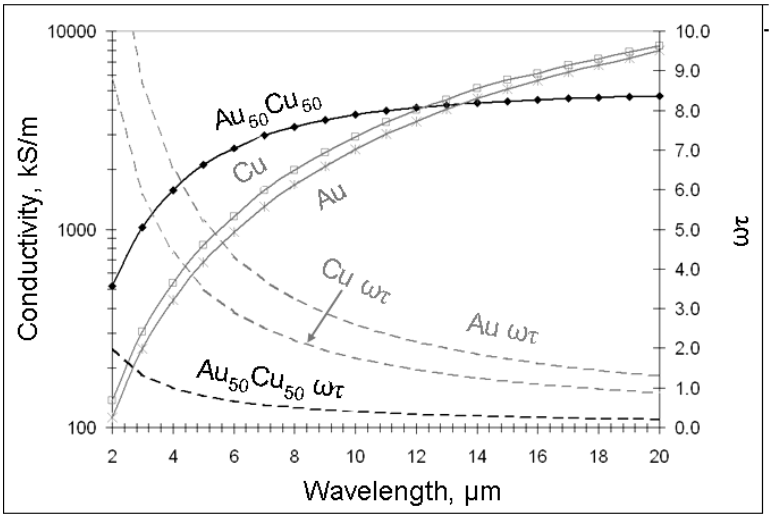

Figure 11: Ellipsometric dynamic conductivity data for Au50Cu50 alloy compared to pure components shown as solid lines and the ωτ products for each shown as broken lines.

The *loss*(δ) for the data in Fig. 11 is shown in Fig. 12. As ωτ decreases *loss*(δ) increases in magnitude in agreement with Eq. 3.3.

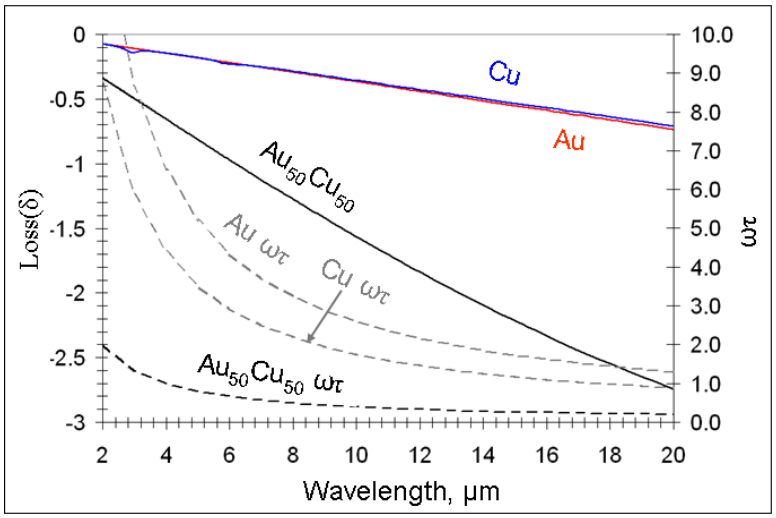

Figure 12: Ellipsometric loss tangent data for Au50Cu50 alloy compared to pure components shown as solid lines and the ωτ products for each shown as broken lines.

The measured dynamic conductivities of the full range of alloys are shown in Fig. 13. Figure 14 shows the corresponding loss tangents. There existed a range of wavelengths for which each type of alloy had the highest dynamic conductivity relative to the other alloys. At wavelengths longer than 7 μm the $Au_{75}Cu_{25}$ or $Au_{25}Cu_{75}$ alloys had the largest dynamic conductivity corresponding to their smaller DC resistivities. At wavelengths ranging from 3 to 7 μm, the $Au_{50}Cu_{50}$ alloy was found to have the largest dynamic conductivity. The $Au_{50}Cu_{40}B_{10}$ alloy was found to have the greatest dynamic conductivity at wavelengths shorter than 3 μm. In each case the ωτ product ranges from about 0.4 to 1.4 in the range of greatest dynamic conductivity. This suggests that a particular relaxation time, τ°, exists for any given wavelength to maximize the dynamic conductivity. This τ° is a convenient reference point for describing the optical properties in terms of DC transport measurements. An expression for τ° is derived in section 3.2.2 and tested against the alloy dynamic conductivity data.

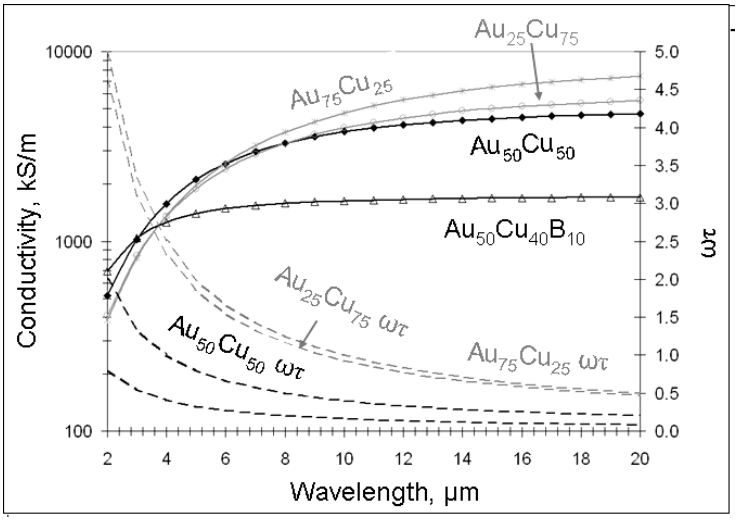

Figure 13: Ellipsometric dynamic conductivity data for range of alloy films including Au75Cu25, Au50Cu50, Au25Cu75, and Au50Cu40B10 as solid lines with ωτ products for each as broken lines.

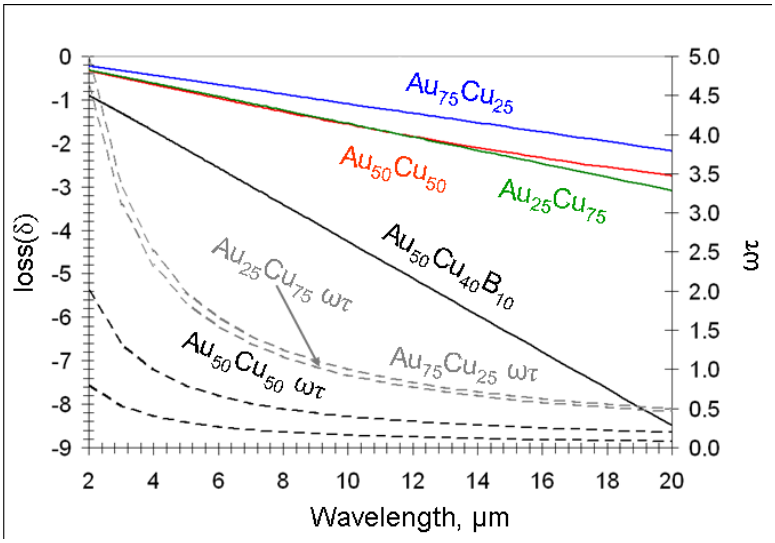

Figure 14: Ellipsometric loss tangent data for range of alloy films including Au75Cu25, Au50Cu50, Au25Cu75, and Au50Cu40B10 as solid lines with ωτ products for each as broken lines.

The absence of phonon scattering at cryogenic temperature decreased the dynamic conductivity in the Au and Cu films as shown in Fig. 15. Due to the lack of thermal processing in the Au film the increase in ωτ is smaller than that of the Cu film; however, the decrease in dynamic conductivity is greater for the Au than for the Cu film. Over the

2 to 20 μm band the ωτ product decreased monotonically from 13.5 to 1.35 at 395 K and from 47.1 to 4.71 at 4 K as shown in table 1. Similarly the ωτ product decreased monotonically in the Cu film from 28.8 to 2.88 at 295 K and from 287 to 28.7 at 4 K. At approximately 4 K the dynamic conductivity of Au decreased to 22, 31, and 47 % of its value at 295 K at wavelengths of 4, 10, and 20 μm respectively. The dynamic conductivity of Cu decreased to 51, 48, and 56 % of its 295 K value at wavelengths of 4, 10, and 20 μm respectively. The cryogenic data showed that the IR dynamic conductivity had the opposite response of the DC conductivity to increases in electronic mean free path. The experiments with impurity scattering also showed the same opposing response.

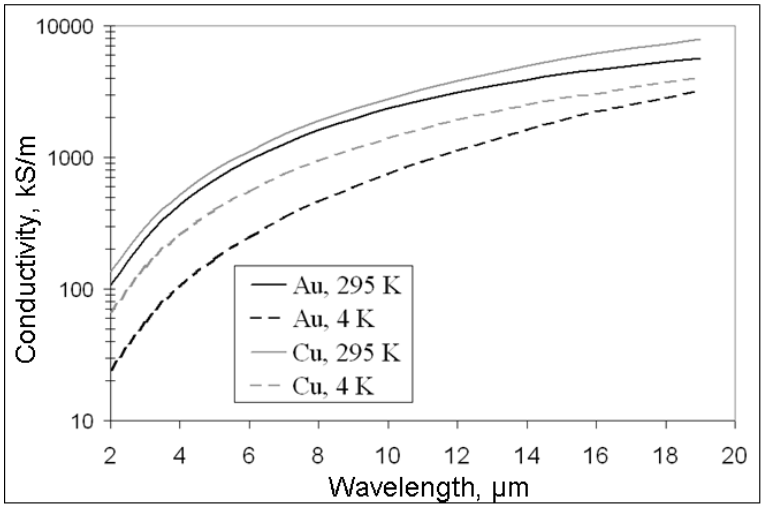

Figure 15: Ellipsometric dynamic conductivity data under cryogenic temperatures. Solid lines refer to data at 295 K, broken lines refer to data at approximately 4 K.

As in the Au-Cu alloy experiments the measured *loss*(δ) follows the increase in ωτ by decreasing at low temperature as shown in Fig. 16.

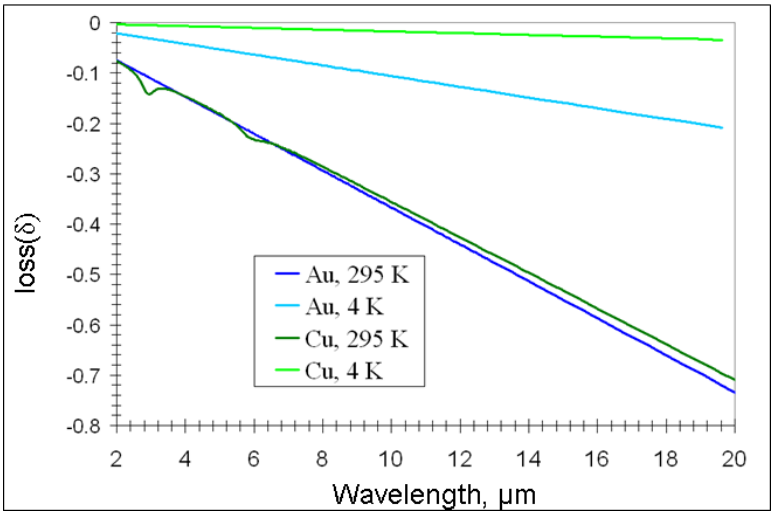

Figure 16: Ellipsometric loss tangent data under cryogenic temperatures

3.2.2 Deviation from the Sommerfeld model caused by the anomalous skin effect

The measured increases in dynamic conductivity were observed when the ωτ product was increased to a value of around 0.4 or higher. Although these results are in qualitative agreement with the Sommerfeld model, there are quantitative differences between the measurements and the classical theory. This is represented in Fig. 17 with the Sommerfeld deviation function γ(ω) defined as the ratio between the measured dynamic conductivity data and the Sommerfeld modeled conductivity defined in Eq. 2.6. The relaxation times measured using the four-point probe and the constants discussed in the experiment section were used when calculating the real part of Eq. 2.6.

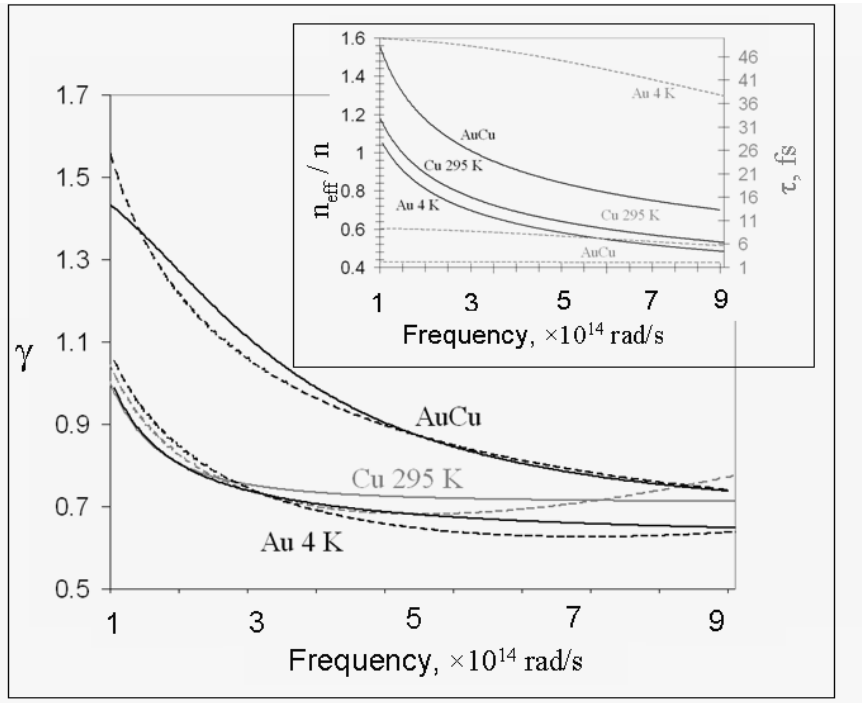

Figure 17: Sommerfeld deviation ratios for selected metals; solid lines refer to measured data, broken lines refer to fitted data. Insert; solid lines refer to , broken lines refer to relaxation time.

The results may be interpreted using the anomalous skin effect and dynamic relaxation time theories as defined in Eq. 3.11. This resulted in a fitting function with two independent constants shown in Eq. 3.11. Expressions for α_1 and α_2 are given in Eq. 3.12.

$$\gamma(\omega) = \frac{\sigma(\omega)_{measured}}{\sigma(\omega)_{Drude}} = \frac{\alpha_1}{\sqrt[3]{\omega}} + \alpha_2 \omega^{5/3} \tag{3.11}$$

$$\begin{aligned} \alpha_1(\beta) &= \frac{1}{\tau_{DC}} \left(\frac{\beta}{V_F} \right)^{2/3} \sqrt[3]{\frac{2m^*}{ne^2\mu_0}} \\ \alpha_2(\beta, b) &= b \left(\frac{\beta}{V_F} \right)^{2/3} \sqrt[3]{\frac{2m^*}{ne^2\mu_0}} \end{aligned} \tag{3.12}$$

The fitted functions are compared to the measured data in Fig. 17 for selected data, and results from the full range of experiments are shown in table 2. The discrepancy between

the fitted and measured functions was computed as a function of frequency and this was taken to be the error in the fitting process. The mean and standard deviation of the error data set was calculated and is shown in table 2.

Table 2: Fitted values and associated error; relative to wavelength where indicated.

					λ, 3 μm	λ, 10.6 μm	λ, 3 μm	λ, 10.6 μm
Metal	**β**	***b*, fs**	**Mean Error, %**	**Standard Deviation, %**	***neff / n***	***neff / n***	**τ, fs**	**τ, fs**
Au 295 K	0.766	0.0577	9.63	5.72	0.558	0.849	10.5	13.5
Cu 295 K	0.447	0.0720	3.83	2.03	0.619	0.941	7.37	9.14
Cu annealed 295 K	9.07	0.0336	12.90	12.00	1.50	2.29	18.8	24.4
Au ~4 K	5.31	0.00653	3.76	1.95	0.154	0.235	44.0	49.5
Cu annealed ~4 K	5840	0.00116	2.71	1.74	0.0189	0.0289	267	301
$Au_{50}Cu_{50}$ 295 K	0.0819	0.0278	2.33	2.74	0.815	~ 1	2.07	2.12
$Au_{75}Cu_{25}$ 295 K	0.207	0.255	5.50	5.20	0.608	0.926	3.46	5.09
$Au_{25}Cu_{75}$ 295 K	0.191	0.378	6.95	5.55	0.581	0.885	2.84	4.65
$Au_{50}Cu_{40}B_{10}$ 295 K	0.0142	0.385	5.00	6.95	0.622	0.947	0.762	0.853

Using known values for the constants in Eqs. 3.10 and 3.12, the dynamic relaxation time and effective carrier concentrations were determined as shown in table 2 and plotted for selected data in Fig. 17. The unknown values in Eq. 3.10 include the quadratic term from the dynamic relaxation time theory and the constant β from the theory of the anomalous skin effect. The fitted values for both constants are shown in table 2. The constant β was directly proportional to the electronic mean free path as expected from its definition in Ref. [3.12]. The quadratic term *b* was small compared to the DC relaxation time as expected, and it was also inversely proportional to the electronic mean free path. The frequency dependent behavior of all the experiments were consistent with that shown in

Fig. 17, so no further information is required to describe the behavior of the films beyond that shown in table 2. Instances where the effective carrier concentration increased above unity were considered to be a result of the model becoming invalid when the anomalous skin effect did not occur. This behavior is seen in the long-wavelength spectra of the size effect and AuCu films which had little anomalous skin effect to begin with due to their small electronic mean free paths.

The mean error and standard deviations were consistently low across the experiments with the exception of the room temperature Au films which tended to be somewhat higher. The values in table 2 show that adding scattering via impurities in Au-Cu alloys increased the effective carrier concentration, and that removing phonon scattering via testing at cryogenic temperatures significantly decreased the effective carrier concentration. The effective carrier concentration is lower for the ~4K Cu film compared to the ~4K Au film due to the larger grain size of the Cu film. At 295 K data for both annealed and unprocessed Cu are shown in table 2. As expected the annealed Cu film has a longer electronic mean free path which results in a larger value for β compared to the unprocessed Cu film.

The changes in the quadratic term *b* in table 2 suggest a connection between electronic mean free path and dynamic relaxation time. In general as impurities in the metal film increase, electrons scatter more as a function of frequency. This implies that the mechanism behind the dynamic relaxation time is neither electron-electron scattering nor a two-carrier mechanism, but that electrons scatter off of the same obstacles at high

frequency as they do in DC transport. However, at high frequencies, scattering events are more frequent when the impurity or defect density increases. The electron-electron scattering mechanism should be independent of crystal structure or impurities, but this was clearly not the case from the data in table 2. Although the annealed Cu film may be assumed to have larger grains than the unprocessed films, the unannealed films should have similar grain sizes near that of their common thicknesses. Thus a two-carrier model involving grain boundaries can not explain the dynamic relaxation time data in table 2. We conclude that electronic scattering in the IR is analogous to scattering in DC transport, but in the IR scattering occurs over a shorter time scale.

The results for impurity scattering in alloy films showed that there was a range of frequencies over which each film had a DC relaxation time that produced the greatest dynamic conductivity. These results suggest that there exists a particular DC relaxation time, τ°, that yields the largest possible real part of dynamic conductivity and *loss*(δ) at a particular frequency for a given metal. This value of τ° is a convenient reference point for describing IR frequency dynamic conductivity in terms of known constants and DC transport measurements. By using the Sommerfeld model in Eq. 3.2 it can be shown that the greatest dynamic conductivity occurs when the DC relaxation time is equal to the inverse of the frequency. This would imply that in the Sommerfeld model τ° is independent of the relationship between the electronic mean free path and skin depth of the metal. A correction factor from the theory of the anomalous skin effect should then be added to the Sommerfeld model prediction of τ°. This yields the expression in Eq.

3.13 where the ratio of effective to DC carrier concentration is used as the anomalous skin effect correction factor.

$$\left(\tau^{\circ}\right)^{3} = \left(\frac{N_{eff}}{N}\frac{1}{\omega}\right)^{3} = \frac{\beta}{V_F}\sqrt{\left(\frac{2m^*}{Ne^2\mu_0}\right)}\omega^{-2} \tag{3.13}$$

In Eq. 3.13 N_{eff} has been substituted from Eq. 3.8. In order to compare DC to IR frequency carrier transport, Eq. 3.13 may be re-written to give the reference DC resistivity ρ° that results in the largest IR dynamic conductivity and *loss*(δ) as a function of frequency in Eq. 3.14.

$$\left(\rho^{\circ}\right)^{3} = \left(\frac{V_F}{\beta}\right)\omega^2\sqrt{\frac{\mu_0}{2}}\left(\frac{m^*}{Ne^2}\right)^{5/2} \tag{3.14}$$

Although β is not a function of frequency, β varies as the electronic mean free path is adjusted by the addition of impurities. In order to quantitatively determine τ° the value of β that corresponds to the alloy with the greatest dynamic conductivity for a particular frequency must be used. This reference β will be called β°(ω) for clarity. Thus an empirical β°(ω) plot may be constructed from the measured data by taking the β values that corresponded to the alloy with greatest dynamic conductivity for a given wavelength range. Using the available data points for the Au-Cu system a step function is generated for β°(ω) as shown in Fig. 18. To aid calculation, the experimental data can be fitted by considering that β is proportional to the relaxation time, which tends to go towards ω^{-1} at the ideal relaxation time. Following this reasoning the data was fit to a Taylor series in Eq. 3.15 with constant terms x_i, and this is shown in Fig. 18.

$$\beta^{\circ}(\omega) \cong x_0 + \frac{x_1}{\omega} + \frac{x_2}{\omega^2} + \ldots \tag{3.15}$$

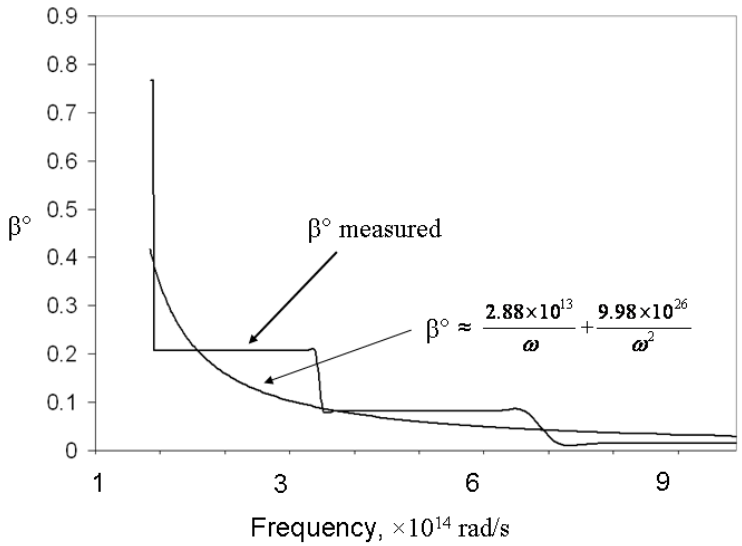

Figure 18: The reference β°(ω) which is taken to be the measured β constant corresponding to the alloy with the highest dynamic conductivity over a given frequency range and fitted to a Taylor series in Eq. 3.15.

In Eq. 3.16 a simplified expression for the reference DC resistivity, ρ°, as a function of wavelength in μm is obtained in units of μΩ-cm using the fitted β°.

$$\rho^{\circ}\left[\mu\Omega - cm\right] = \frac{34.1}{0.248\lambda[\mu m] + 0.0654\lambda[\mu m]^{4/3}} \qquad \text{for Au-Cu system} \qquad (3.16)$$

The alloy film experiment may then be used to verify the prediction of Eq. 3.14. Figure 19 shows the percent increase in dynamic conductivity as a function of wavelength for Au with different concentrations of Cu or B impurities. The bolded black line in Fig. 19 highlights the dynamic conductivity increase in the film that was predicted by Eq. 3.14 to have the greatest dynamic conductivity over the wavelength band. The alloy composition and resulting DC resistivity are displayed for each band at the top of Fig. 19. The reference DC resistivity based on Eq. 3.16 is plotted in the insert to Fig. 19.

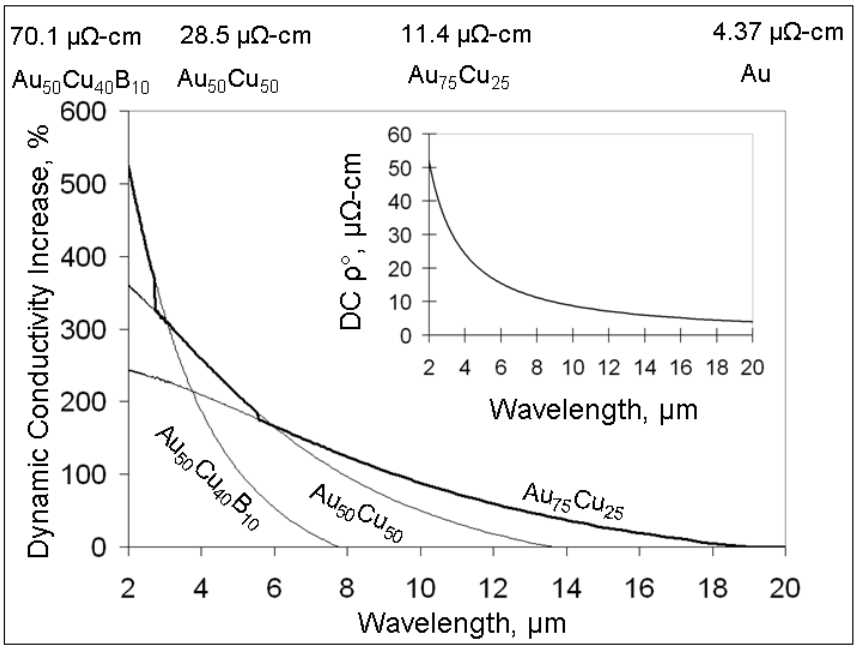

Figure 19: Dynamic conductivity increase is plotted for each alloy (in at. %) compared to pure Au. The bold line highlights the alloy with the greatest conductivity increase based on ideal resistivity in Eq. 3.16 compared to measured values shown

There is good agreement between the ideal relaxation time predicted at a given frequency by Eq. 3.16 and the measured relaxation time for the alloy with the greatest conductivity at the corresponding frequency. This may be seen by comparing the ideal relaxation time in the insert to Fig. 19 to the measured values shown at the top of Fig. 19 for a given wavelength range. Because of the dependence in Eq. 3.14 on the surface scattering term β, the ideal resistivity is self correcting of changes in temperature and impurity or defect densities. Thus Eq. 3.14 will have useful applications in determining the optical properties of metal films at any wavelength or operating temperature.

Decreasing the relaxation time was proven to be an effective method for increasing the dynamic conductivity of noble metals in the IR band. These effects resulted from an increase in the effective carrier concentration. At the same time the *loss*(δ) increases in

magnitude indicating that more of the incident electromagnetic wave is 'lost' to modes normal to the surface of the metal and thus no longer confined to the surface. The increase in dynamic conductivity was strongest at shorter wavelengths below 8 μm where the anomalous skin effect was more pronounced. The dynamic conductivity in the 3-5 μm wavelength band was shown to increase by more than 300%, and below 3 μm the dynamic conductivity increased by more than 500%. There was also shown to be a corresponding decrease in dynamic conductivity at cryogenic temperatures to only 20 % of its room temperature value in the 3-5 μm wavelength band. A relationship was established for the reference DC relaxation time or resistivity to produce the greatest possible dynamic conductivity and *loss*(δ) as a function of both frequency and the fraction of effective electrons from the anomalous skin effect. By adjusting for the anomalous skin effect the reference DC resistivity is able to take the effects of both temperature and impurity scattering into account. These theories have been verified by experiment and may be used to determine the optical properties of metallic thin films based solely on DC transport measurements and known physical constants.

CHAPTER 4: STATIC IR METAMATERIALS

This chapter addresses practical applications and fabrication details of metamaterials. Chapter 4.1 discusses the details associated with fabricating metamaterials on a polymer substrate for flexible tags and decals. Metamaterials are generally fabricated on silicon wafers. One purpose of metamaterials is to modify the optical properties of surfaces, so flexible substrate fabrication is an important technique because most real surfaces are not perfectly flat wafers. Another purpose of metamaterials is to act as an optical element. In the IR the cost associated with optical systems is dominated by the cost of the optical elements. Since metamaterials may be fabricated using entirely earth-abundant materials such as Si and Al, metamaterial filters and focusing elements compete well against traditional IR optics. In addition static metamaterials may be tailored to operate at any frequency yielding a flexibility that can not be achieved with traditional optics. A good example of metamaterial optics is in chapter 4.2 which shows that metamaterials may be used to create the most narrow-band THz filters demonstrated to date.

4.1 Element Fabrication on Flexible Substrates

Microlithography techniques used in the fabrication of photonic devices traditionally use rigid substrates such as Si wafers. However, metamaterials often require flexible substrates, so that the final structure is able to be conformally contacted to a nonplanar surface. The conformal substrate considered in this study was HD Microsystems liquid polyimide. Metamaterial elements appropriate for the IR [4.1] typically have critical dimensions between 0.2 μm and 2 μm, with excellent spatial uniformity of the final

periodic structure required. The metamaterial shown in Fig. 20 consists of three layers on top of the underlying structural substrate, a continuous metallic groundplane, a continuous dielectric standoff layer, and the periodic microstructural elements.

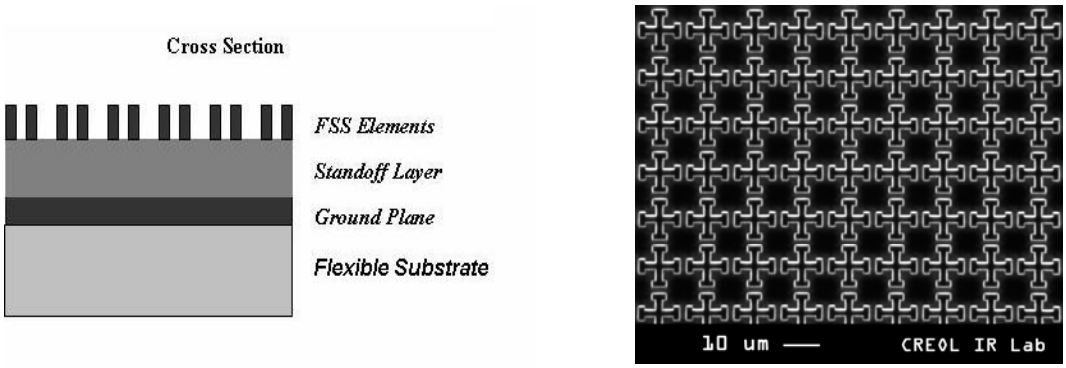

(a) (b)

Figure 20: Metamaterial structural schematic with cross section (a) and top view (b).

The thickness of the standoff layer is typically $\lambda/4n$, where λ is the center of the design wavelength band of operation and n is the refractive index of the standoff layer, which yields thicknesses in the range of a few μm. The groundplane and elements are fabricated from metallic films of typical thickness of 0.1 to 0.2 μm. The Jerusalem cross designs were used in this study as the unit cell geometry for the metamaterial (compared to the square loop designs of Ref. 4.1) because of the presence of a second harmonic resonance that was useful in applications such as frequency selective filters.

When fabricating on a flexible substrate, it is desirable that the Young's moduli of the substrate and standoff layer be similar, which indicates that polymers be considered as candidate materials for the standoff layers. For example HD Microsystems liquid polyimide, and Benzocyclobutene (a candidate polymer standoff layer) have Young's moduli of 2.7, and 2.9 GPa respectively. Standoff materials used previously [4.2] had

Young's moduli ranging from 80 GPa for a-Si to 223 GPa for Zirconia. However, choice of the standoff layer material is constrained by two considerations that tend to exclude most polymers. To maintain proper functionality of the metamaterial, it is desirable to minimize absorption losses in the standoff layer. It is also difficult to fabricate many common polymers with the quarter-wave optical thickness required. Thus, the polymer chosen for the standoff layer must have high IR transparency and be capable of being spun or rolled out to the desired thickness with good uniformity.

The high resolution required in the fabrication of the FSS elements places constraints on the flatness and surface roughness of the combined underlying structure of the substrate, groundplane, and standoff layer. Typical flexible substrates such as polyimide sheets are both locally rough and difficult to secure in a sufficiently flat configuration. Previous research [4.3-4.4] has addressed this issue by using liquid polyimide, which gives the user control over both the surface roughness and flatness of the polyimide substrate. However, the lithographic-resolution limit seen in these references was on the order of tens of μm, and relatively small areas of the substrate were used for fabrication. In this study, a full 10 (4 inch) diameter substrate was populated with metamaterial elements. The combination of large write area and small element size required that the substrate had less than 10 nm rms surface roughness, with a high degree of planarization.

To investigate the optical properties of the candidate polymers, a J.A. Woollam IR ellipsometer was used. The ellipsometer uses polarization data such as the amplitudes of the electrical field components and their relative phase shifts to determine the complex

index of refraction by fitting to an appropriate model. To facilitate fabrication, three resists and spin on dielectrics (ZEP, PMGI, and BCB) were investigated to find standoff-layer materials that met the optical and mechanical requirements. Zeon Chemicals ZEP 520A7 is a positive tone electron-beam resist that has favorable optical properties in the mid IR as shown in Fig. 21. ZEP can be difficult to fabricate on because of its poor adhesion to most metals. An adhesion promoter such as hexamethyldisilazane (HMDS) can improve adhesion to some oxides, but fabricating small metallic elements onto ZEP remains a challenge.

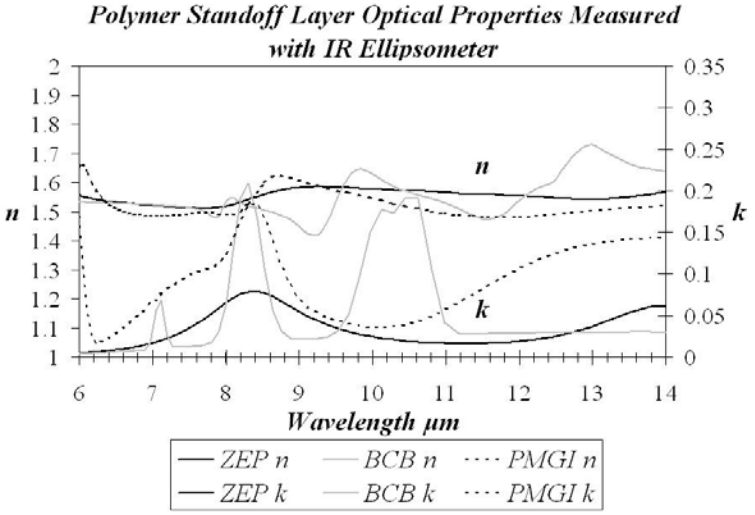

Figure 21: Mid IR Optical Properties of Polymers

A complete fabrication process was attempted with polydimethlglutarmide (PMGI). MicroChem PMGI SF7 was used. PMGI is from the same family of polymers as polymethylmethacrylate (PMMA) and shares many of the same optical and chemical properties. As seen in Fig. 21, the loss associated with PMGI in the IR is significant. In two passes of 10.6 µm radiation through a quarter-wave standoff layer (1.75-µm

thickness), 44% of the radiation is absorbed. This leads to undesirable increases in emissivity beyond 10 μm in PMGI.

PMGI and PMMA are both cured at 180 C which is a lower cure temperature than the spin-on dielectrics require. PMGI is preferable over PMMA because it is not removed by solvents commonly used in post-exposure lithographic processing such as Acetone or Xylene. PMGI also has this advantage over ZEP which is attacked by Methelyne Chloride and Acetone over time.

Using the PMGI standoff layer, problems were encountered in the liftoff of the excess metal between structures, after the FSS pattern had been exposed in photoresist and metalized with Ti. Fig. 22 shows the boundary between successfully lifted off structures, non-lifted off structures, and the region where the metal elements lost adhesion to the PMGI. The entire wafer was exposed, developed, and metalized. The liftoff was stopped before completion because the individual FSS elements were disassociating from the wafer in the solvent. The elements did not appear to liftoff immediately. Indeed, the small region of normally lifted off elements shows that there was some time between proper liftoff and disassociation of the elements, which unfortunately was not spatially uniform. The disassociated elements left behind ghost images that were measured via profilometery to be 20 nm deep.

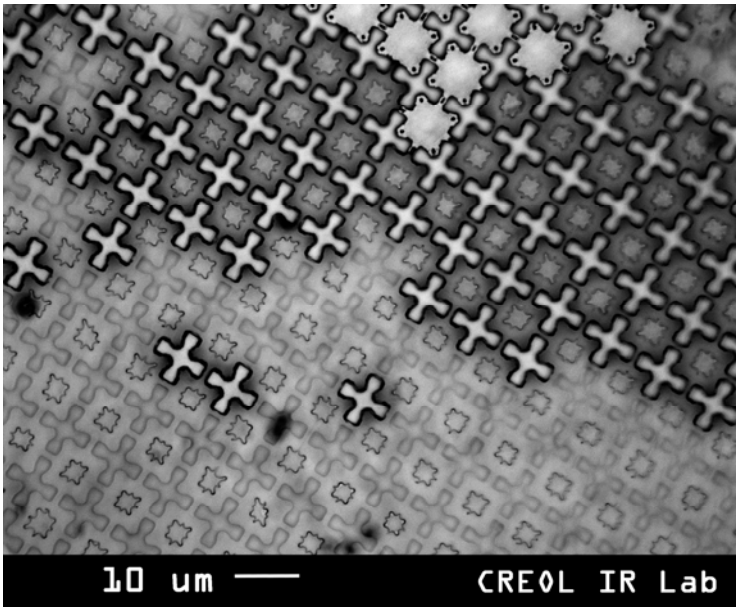

Figure 22: PMGI liftoff results; bottom, ghost images left behind after disassociation of elements; middle, properly lifted off elements; top middle, elements before liftoff.

The disassociation of the antenna elements and the appearance of ghost images appeared consistently over six separate trials without significant deviation. We suspect that this phenomenon was caused by the oxidation reaction between the polymer and the Ti elements. Normally an oxidation reaction between a metal and a polymer is favorable and provides an adhesion mechanism. For polymers from the PMMA family the new oxide species that forms after the reaction is not chemically bonded to the remainder of the polymer. During the reaction thermal energy is transferred from the metal elements to the PMGI beneath causing an amorphization of the polymer carbon structure [4.6]. This resulted in the metal elements floating off of the substrate along with the reacted portion of the PMGI leaving behind the ghost images seen in Fig. 22. Noble metals without an oxidation state at room temperature and standard pressure such as Au or Ag were considered to replace Ti, but these non-reactive metals have no mechanism for adhesion.

Following the initial experiments with PMGI, we attempted to use a layer of silicon nitride or a layer of silica to insulate the Ti elements from the polymer layer. However a mismatch in the thermal coefficients of the dielectrics compared to the polymer resulted in a cracking of the dielectric layer. This initially occurred when the substrate was cooling down after deposition of the dielectric, but the cracking became more pronounced following further thermal processing steps.

Of the three polymer standoff layer choices investigated in this study, Benzocyclobutene (BCB), gave the most satisfactory results overall. Referring again to Fig. 21, we see that compared to the other polymers, BCB has the highest IR absorption. Although this is undesirable, the absorption is still low enough that it may be compensated for in the FSS design. BCB has an advantage over the other candidates because it has the ability, unlike ZEP, to form strong bonds with transition metals such as Ti. Unlike PMGI, the oxidation reaction between BCB and Ti does not result in the disassociation of the reacted product. Another advantage of BCB is that as a spin-on dielectric material, it can be thinned to achieve a layer of any thickness from 300 nm to 2 μm. It must however be cured at 250 C in an inert environment. The cure temperature was not an issue for liquid polyimide films which were not observed to deplanarize under these conditions.

In initial IR metamaterial fabrications, an optically thick (150 nm) Au film was used as the ground plane, which created a problem with the use of a polymer standoff layer because of the lack of adhesion between Au and BCB. During fabrication trials it

appeared that the metal elements were disassociating from the BCB, but ellipsometric measurements proved that the BCB layer beneath the elements was no longer present following the liftoff procedure. It was concluded that the BCB had insufficient adhesion with the Au ground plane. A solution was attempted by evaporating a Ti seed layer between the Au and the BCB, but this was unsuccessful because the Ti did not adhere well to the Au.

Au adheres well to Ti because the surface of the Ti film is rough and provides a means for the polycrystalline Au to form a diffusive bond with the Ti. The Au film is smooth and does not provide an opportunity the Ti film to form a strong bond. BCB forms a strong bond with Ti via oxidation. For this reason subsequent FSS designs used an all-Ti ground plane. Fig. 23 shows the spectral conductivity for Au and Ti as well as the spectral skin depth for both metals. At a wavelength of 10 μm the skin depth of Ti is about 50 nm, and the skin depth of Au is about 12 nm. Either 150 nm thick metal film is sufficient to prevent transmission, but it is also desirable in the FSS design to have the highest possible spectral conductivity in the mid-IR range. Although Au is preferred for this reason, Ti may be used with appropriate design compensation. Modeling software such as Ansoft HFSS has been successfully modified to account for this spectral dependence [4.7].

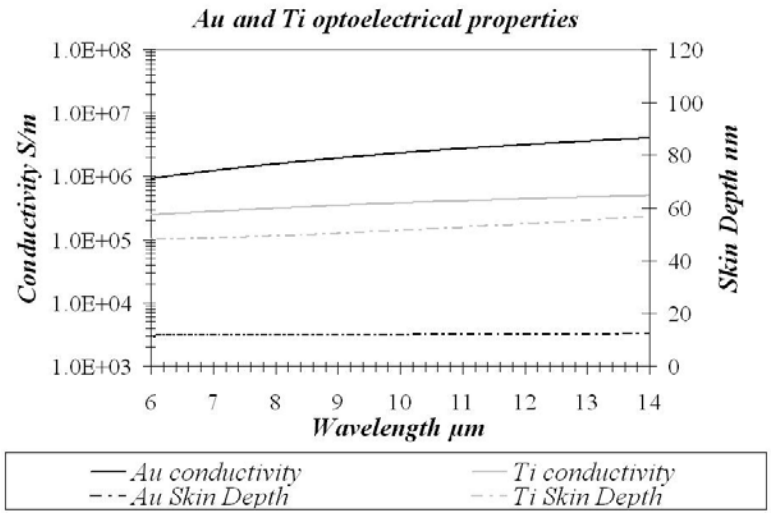

Figure 23: Spectral conductivity and skin depth derived from optical constants measured with IR-VASE Elipsometer.

Three separate masks were designed consisting of a 10 cm (4 inch) square fully populated with elements. Two different types of elements were used depending upon the design. Two designs used Jerusalem cross elements as shown in Fig. 20, one with a 12.7-µm periodicity and a 1.7-µm critical dimension, and the other with a 7-µm periodicity and a 1.3-µm critical dimension. The third type of element fabricated was a square-loop design (Ref. 4.1) with a 10-µm periodicity and a 1.2-µm critical dimension.

Fabrication of the FSS periodic structures used HD Microsystems liquid polyimide, which served as a structural substrate beneath the ground plane shown in Fig. 20. Liquid polyimide could be spun on and cured by the user. This allowed for control over surface roughness. HD Microsystems liquid polyimide was spun onto a prime-grade Si wafer at 2000 rpm. Each layer was 13-µm thick and three layers were spun for a total substrate thickness of about 40 µm. The polyimide film was soft cured at 150 C between each

layer, and the final three-layer film was hard cured at 300 C in an inert environment. The surface roughness was measured to be 4 nm rms with Dektak profilometery.

The remaining process steps were carried out as they would have been if the substrate was simply a Si wafer. The 150-nm thick Ti ground plane was deposited onto the liquid polyimide surface using an electron beam evaporation system. Next, BCB was spun onto the Ti at a speed and viscosity combination appropriate to the desired thickness. Undiluted BCB was spun at 1500 rpm to achieve a thickness of 1.8 μm. Charts for BCB showing the film thickness as a function of spin speed for given viscosities may be obtained from the Dow Corporation. BCB also uses an adhesion promoter (Dow AP3000) that goes on before the polymer film. The BCB film was soft baked at 120 C and hard cured in an inert environment at 250 C.

Electron-beam lithography was used to write the elements. This was done to ease fabrication issues associated with the resolution of the available photolithography systems. ZEP 520A7 was used as the electron-beam resist, and cured for 3 minutes at 180 C. The liquid polyimide substrate led to nearly complete uniformity and well resolved elements across the populated region.

The final fabrication steps were to deposit a metal film onto the pattered resist. Depending upon the metamaterial design, 100 nm of either Ti or Au was used for the antenna elements. A 10 nm thick Ti adhesion layer was used beneath the Au film. Both metals were deposited via electron-beam evaporation at 5.0×10^{-6} Torr and 50° C. ZEP

was removed by Methylene Chloride. Although liftoff was much faster with ZEP compared to standard photoresists, the wafer had to be quickly rinsed and re-immersed in solvent to prevent metal contaminants from settling on the surface.

Once the lithography processing was completed the liquid polyimide could be peeled off of the Si wafer. One way to peel the liquid polyimide off of the substrate was to place a piece of weak adhesive tape across the surface and then pull the tape off. This did not remove the FSS structures and several repetitions would cause the polyimide to begin to separate from the substrate. Another method to remove the liquid polyimide from the Si wafer is to break the wafer and carefully peel the polyimide off as the two halves of the wafer are pulled apart. Figure 24 shows the FSS after removal from the Si wafer. The metalized FSS elements are shown to be intact after removal in part b of figure 24.

(a) (b)

Figure 24: Completed polyimide FSS: (a) Flexible 10 cm (4 inch) wafer fully populated, (b) Elements intact on flexible substrate after polyimide backing removal.

The substrate flatness of the sample was measured using a Newton interferometer while the samples were still fixed to Si wafers. A transparent optical flat was placed in contact with the sample and a fringe pattern was observed using a mercury lamp. The lamp was filtered so that only the green line with λ = 546 nm was transmitted. Flatness was

measured by counting the number of circular fringes per unit length. The liquid polyimide film on Si showed 0.06λ/mm in the center of the wafer and 0.08λ/mm toward the edges of the wafer. Deviations from flatness in the polyimide film were radially symmetric. This was likely a result of the spin-on application of the film. For comparison a polyimide sheet was glued to a substrate and measured in the same manner. The polyimide sheet showed deviations in flatness ranging from 1.25 λ/mm to 3.75λ/mm. The liquid polyimide substrates were easily able to conform around a cylindrical axis, and there did not appear to be any damage to the elements as the substrate was elastically deformed [4.7]. The substrates are reasonably easy to handle, but can be torn by a shearing force. They can handle a moderate degree of stretching along the plane of the structures. The liquid polyimide membranes may be used at temperatures up to 300 C. The fabrication techniques demonstrated in this section open the door for the fabrication of other structures such as IR detectors that may need to employ lithography on a similar element size on flexible substrates.

Three different metamaterial structures were fabricated on liquid polyimide membranes. The periodic structures had periodicities from 1.2 to 1.7 μm and fully populated a 10 cm (4 inch) diameter wafer. The metamaterials showed excellent uniformity across the wafer. The success of the fabrication suggests that the degree of non-flatness and surface roughness in these films was acceptable for 1-2 μm critical dimension lithography processes. The liquid polyimide structures had deviations in flatness from 0.06 λ/mm to 0.08 λ/mm and 4 nm rms surface roughness. Benzocyclobutene (BCB) was used as an intermediate layer beneath the periodic structures. It was found to have sufficiently low

absorption in the mid-IR as well as favorable adhesion properties for metamaterial fabrication. Two other polymers were found to have unfavorable adhesion properties. Au and Ti were used for the periodic structures as well as for the ground plane beneath the intermediate layer. The conductivities of Au and Ti at IR frequencies were measured, and Ti was found to be less conductive (by nearly an order of magnitude) than Au. The fabrication techniques described here would be suitable for the fabrication of many different types of periodic microstructures on flexible substrates.

4.2 Narrowband Metamaterial Filters

Metamaterials using Ag dipole elements were simulated, fabricated, and tested to demonstrate improved narrow band transmission compared to the current state of the art filters in the 1-2 THz band. Several designs are presented including variations in dipole packing density, and sensitivity to a cladding layer. The sharpest resonant response was measured to have a bandwidth of 90 GHz at a center frequency of 1.3 THz, for a Q of 14.5, which is the highest thus far reported for a THz narrow band filter. In addition, the sensitivity of the resonance of the structures to material properties may be exploited as a way to measure the permittivity and loss tangent of thin films in the THz band.

Metamaterials may be used for narrow band transmission filters and other photonic applications [4.8]. The sub-wavelength sized metamaterial elements were incased in a mechanically flexible cladding. Narrow band transmission filters are characterized by a Q factor defined as the ratio of the center frequency to the full width at half maximum (FWHM) of the filter. The current state of the art for metamaterial narrow band filters in the 1-2 THz band has been achieved using a periodic array of Cu cross slot elements on a glass substrate, and a Q factor of 6.1 at a center frequency of 1.54 THz [4.8]. Recent work has demonstrated the use of split-ring resonator metamaterials in the THz which have a Q factor of 4.2 at a center frequency of 1.05 THz [4.9]. In this section a new class of THz metamaterials are explored based on an adaptation of gangbuster elements [4.10] which consist of dipole antennas having lengths approximately equal to half of the wavelength at peak transmission. The dipoles are staggered as shown in Fig. 25 so that

the periodicity is small on both the x and y axis to prevent diffraction effects. Following the nomenclature of RF gangbuster surfaces, the THz gangbuster designs are classified by a packing 'type' defined by the ratio of the major to minor axis as shown in figure 20. In this paper type 2, 3, and 4 gangbuster surfaces are evaluated in the 1-2 THz band. In addition, the sensitivity of the filter's resonance location and width to the permittivity and loss tangent of the cladding layer was also investigated and shown to have applications in the determination of unknown permittivities for materials of potential utility in the THz band.

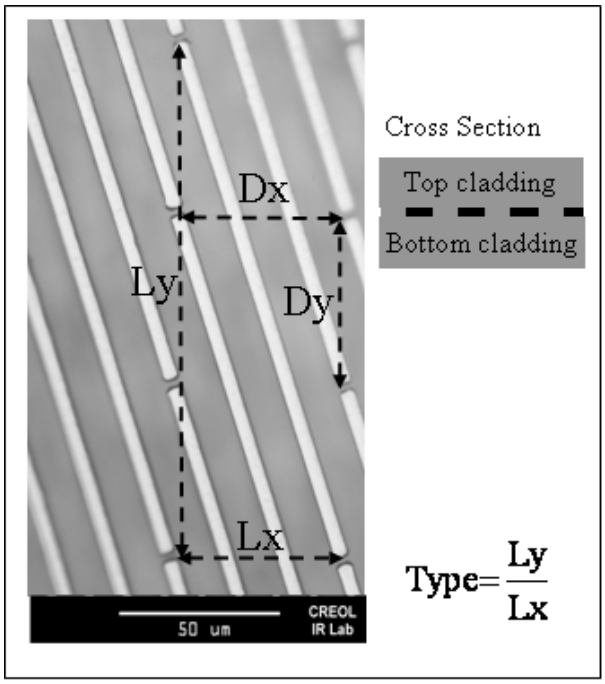

Figure 25: Dipole metamaterial array configuration indicating gangbuster type with cross section shown on right where thicknesses of the top and bottom cladding layers

The response of the THz gangbuster metamaterials was simulated using Ohio State Periodic Method of Moments (PMM) code. A sheet resistance based on four-point probe measurements and the Drude model was used in the PMM simulations. The metallic

elements were immersed in the center of an 18-μm-thick cladding layer. The permittivity of the cladding layer at 1.5 THz was initially unknown.

Identifying suitable metamaterial substrates in the THz band is challenging compared to the RF or IR bands. In the RF substrates that are very thin compared to the wavelength are of convenient mechanical thickness, while substrates in the IR band are typically many wavelengths thick resulting in Faby-Perot resonances that are very closely spaced. To avoid substrate loss and minimize the impact of unwanted substrate modes , we used a membrane substrate consisting of an 18-μm layer of the flexible polymer HD Microsystems liquid polyimide. The IR properties of liquid polyimide have been previously measured and the material was found to have low absorption at long wavelengths [5]. Detailed device fabrication and processing using liquid polyimide has been described in a previous article [6].

The spectral transmission of the metamaterials was measured using a Bomem Fourier transform THz spectrometer with a Hg arc lamp source and a He-cooled Si bolometer. The beam diameter of the measurement region was 10 mm. In order for the gangbuster to function properly, the incident radiation must be linearly polarized and oriented parallel to the dipoles. Thus a wire grid polarizer was placed between the source and the elements. The required orientation of the polarizer may be determined by taking the arc tangent of the number corresponding to the gangbuster type.

Measured and simulated results for linearly polarized input are shown in Fig. 26 for three different element packing types. Although the most densely packed surface, type 4, would be expected to result in the highest Q factor, measurements show that the effect of finite conductivity was to reduce the Q factor and hence widen the spectral response. As the packing density increased, so did metallic loss, and the type 4 surface had smaller throughput and a lower Q factor than the type 2 metamaterials. The type 2 surface was measured to have the highest Q factor (14.5) reported to date in the THz band. Table 3 lists the dimensions and Q factors for the metamaterials.

Table 3: Gangbuster dimensions and measured results.

	Lx	Ly	Dx	Element width	Center Frequency	Q factor
Type 2	35.5 μm	142 μm	81 μm	25 μm	1.35 THz	14.5
Type 3	22.0 μm	198 μm	71 μm	6 μm	1.03 THz	10.0
Type 4	8.67 μm	139 μm	37 μm	5 μm	1.41 THz	11.6

The agreement between simulation and measurement was excellent for the type 2 and 3 packing densities, but the simulation predicted a larger Q factor for the type 4 packing density than was measured. The PMM software uses a sheet resistance approximation to represent a metal surface, which limited the simulation's accuracy when a finite conductivities was used.

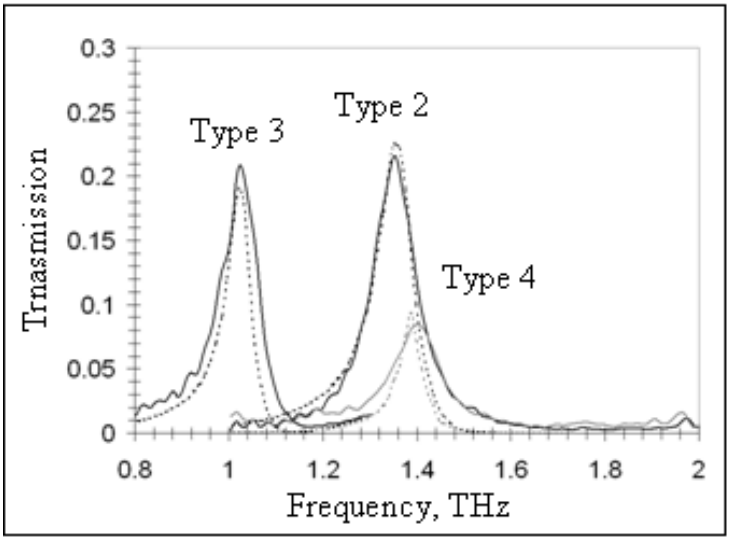

Figure 26: Transmission for gangbuster type 2, 3, and 4 with linearly polarized input. Measured data in solid lines, model predictions in broken lines.

Thus, the simulation predicted a narrower bandwidth than what was measured, which was most noticeable for the type 4 surface. Measured transmission was below 25% for all of the devices due to substrate reflection loss and 50% of the incident radiation being blocked by the linear polarizer.

Comparing the modeled and measured filter resonance in terms of center frequency, peak transmission strength, and width, we were able to obtain a fit for the permittivity and loss tangent of the cladding layer, which are presented in Table 4.

Table 4: Material properties. Sheet resistance measured, permittivities are fitted.

Element thickness	**Element Metal**	**Sheet resistance**	**Cladding thickness**
200 nm	Ag	0.385 Ω/Sq	18 μm
Dielectric	**Frequency**	**Permittivity**	**Loss Tangent**
Polyimide	1.03 THz	3.6	0.0042
Polyimide	1.35 THz	3.55	0.011
BCB	1.41 THz	1.85	0.24

The center frequency had the strongest dependence on the permittivity, while the peak transmission depended most strongly on the loss tangent. If a set of gangbuster surfaces of various types or element lengths (with a resulting range of resonant frequencies) were fabricated on a given thin film substrate, this dependence could used to determining the THz optical properties of the film material. We used the sensitivity of the metamaterial resonance to the properties of the metallic elements and the surrounding dielectric to measure the THz permittivity and loss tangent of the popular spin-on dielectric BCB (Benzocyclobutene, or Dow Cyclotene) which can be used in the construction of THz metamaterials. In this portion of the study, BCB was spun on top of the type 2 elements in place of top cladding layer of liquid polyimide. The permittivity and loss tangent of BCB at 1.41 THz were thus fitted, with results shown in Fig. 27 and Table 4.

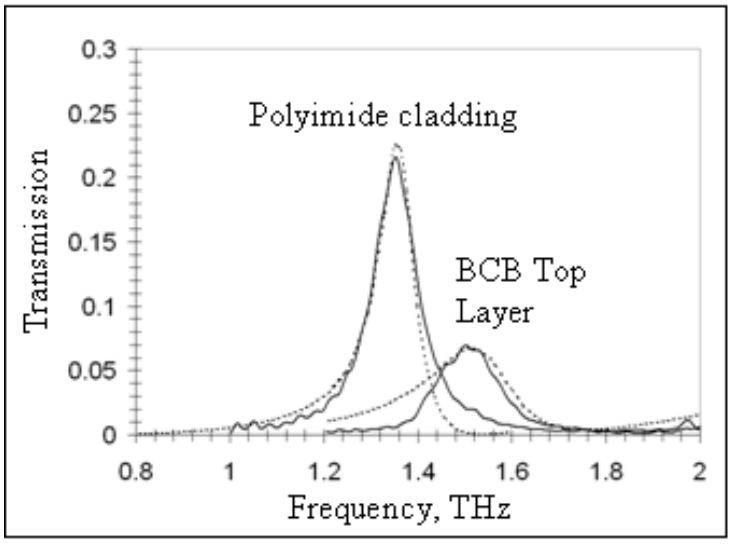

Figure 27: Top cladding for type 2 gangbuster replaced with BCB and compared to all polyimide cladding. Measured data in solid lines, model predictions in broken lines

Metamaterials consisting of gangbuster elements immersed in a flexible cladding layer were demonstrated to have the highest resonant Q factor yet observed (14.5) for a filter in the 1-2 THz band. In addition, the metamaterial resonance was shown to be sensitive to

material properties of the metals and dielectrics; and this property was used to measure the unknown properties of useful materials at THz frequencies.

CHAPTER 5: METAMATERIALS FOR SURFACE-ENHANCED IR SPECTROSCOPY

Resonant metamaterial elements are characterized by their extinction spectrum measured with FTIR spectroscopy. They have a resonance frequency which corresponds to the minima in the transmission spectrum. Since the principal task of a tunable metamaterial is to dynamically tune the resonance frequency, it is important to understand the factors that affect the resonance frequency in a static metamaterial. The experiments in this chapter began with the persistent problem of measured resonance frequencies that blue shift compared to simulations. This problem was solved by showing that dielectric components of the seed layer and the native oxide on Si wafers reduced the fringing field capacitance of the elements and thus blue shift the resonant frequency. Accurately accounting for these dielectric layers in FEM has resulted in the best agreement between measurements and simulations observed to date in IR metamaterials.

In addition to understanding the contributions to the metamaterial's resonance frequency from surrounding dielectric layers, the sensitivity the elements exhibit has interesting applications to IR spectroscopy. FTIR extinction spectra are shown to be enhanced by the presence of resonating elements such that vanishingly thin films as small as 2 nm may easily be detected in the extinction spectrum. Thus metamaterials enable FTIR measurements over nanoscale optical-path lengths. Normally in FTIR measurements a microscale optical-path length is required in order to produce a sufficient extinction signal. In order to make use of surface-enhancement phenomena, analytical models are formulated in this chapter to explain the physics behind the resonance shifts and coupling

events. Combined with other plasmonic techniques, surface-enhancement and its ability to obtain signals from nanoscale path lengths may be used to realize new FTIR-on-a-chip technologies.

5.1 Fringing Field Effects of thin oxide layers

The impact of the native oxide layer on metamaterial device performance has not been studied to date. It is reasonable to expect that such layers will have an effect, since the resonance of metallic IR metamaterial elements will be impacted by their fringing-field capacitance which results from intra-element fields between opposite sides of the element. These fields pass through the interface between the metal elements and the Si wafer; when a native oxide or other thin insulating layer is present this capacitance may change considerably.

This section demonstrates the sensitivity of IR metamaterials fabricated on semiconductor substrates with thin silicon dioxide (SiO_2) layers. This sensitivity is manifest as an SiO_2-thickness-dependent shift in the spectral location of both resonances as well as coupling between the SRR resonance and the Si-O absorption resonance. The native oxide effect explains blue shifting in the resonance spectral location in measurements compared to numerical simulations that is commonly seen in the literature such as Ref. 5.1.

Split-ring resonator (SRR) type metamaterials operating near 1 THz exhibit dual resonances when incident radiation is linearly polarized parallel to the gap in the elements [5.2]. By scaling down the size of the SRR elements dual resonances in the IR

at wavelengths of 4 and 10 μm (75 and 30 THz) may be achieved. A schematic of an SRR element with labeled dimensions is given in Fig. 28.

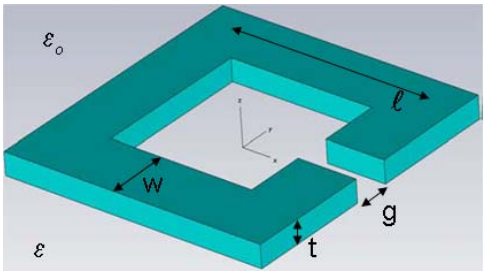

Figure 28: Schematic of SRR element.

The high frequency resonance at 4 μm is due to coupling between elements in the array and is described in Ref. 5.3. The fundamental resonance at 10 μm is due to the electronic resonance of the unit cell and may be described as an LC circuit with resonance frequency, ω_0, as defined by Eq. 5.1.

$$\omega_0 = \frac{1}{(LC)^{1/2}} = \frac{1}{\left[L\left(C_g + C_f\right)\right]^{1/2}} \tag{5.1}$$

For SRRs C_g is the gap capacitance defined by Eq. 5.2 with permittivity of free space ε_0.

$$C_g = \varepsilon_0\left(\frac{wt}{g}\right) \tag{5.2}$$

The TiO_2 layers that occur as part of the adhesion layer and the SiO_2 layer beneath the elements form a series capacitance to the fringing field across the diameter of the SRR. This fringing-field capacitance, C_f, depends upon the permittivity and thickness of the thin film stack of lower index oxide layers that exist between the SRR elements and the Si substrate as shown schematically in Fig. 29.

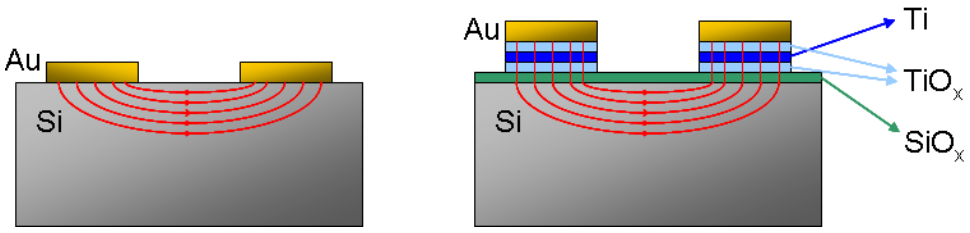

Figure 29: Schematic of fringing-field capacitance where electric field lines are shown across the diameter of the SRR penetrating the oxide layers beneath the elements.

As the thickness of the SiO_2 layer, t_{SiO2}, increases relative to the penetration depth of the resonant electric field mode, t_n, C_f decreases according to Eq. 5.3

$$C_f = \left[\varepsilon_0 + \varepsilon_{SiO2}\left(1 - \frac{t_{SiO2}}{t_n}\right) + \varepsilon_{TiO2}\left(1 - \frac{t_{TiO2}}{t_n}\right)\right] \times \eta \tag{5.3}$$

where ε_{SiO2} and ε_{TiO2} are permittivities of SiO_2 and TiO_2 respectively. The term η is a geometrical factor given by Eq. 5.4.

$$\eta = \frac{\pi\ell}{3\ln(\ell/a)} + \frac{(2w+2t)}{2\pi}\left[\ln\left(\frac{4a}{g}\right) - \gamma - \frac{2}{15}\right] \tag{5.4}$$

In Eq. 5.4 a is the rectangular equivalent radius to a circular loop and γ is Euler's constant. The inductance may be computed based on the geometry using Eq. 5.5.

$$L = \frac{\mu_0}{\pi}(2\ell)\left[\ln\left(\frac{\ell}{a}\right) - \gamma + \frac{a}{\ell}\right] \tag{5.5}$$

By combining Eqs. 5.1 and 5.3 it is clear that as the thickness of the SiO_2 layer increases the reduction in the fringing-field capacitance will decrease resulting in a blue-shifting effect on the resonant frequency of the metamaterial. Since a similar fringing-field effect may be expected to occur between elements, it should also be the case that a blue shift should be observed in the high frequency resonance as the SiO_2 thickness increases.

Changes to the fringing field capacitance may be used as a surface-enhancement technique for the detection of low-loss materials within the near-fields of the elements. If either the thickness or permittivity of the unknown dielectric were known then the corresponding unknown property could be fit using Eqs. 5.1 and 5.3. If a resonance shift did occur one would also know that it was due to a dielectric layer within t_n of the elements. Such spatial resolution capabilities do not exist in current IR spectrometry techniques.

An experiment was designed to test the effect of thin SiO_2 layers from 0 to 10 nm thick at the interface between the elements and the Si substrate. For 0 nm SiO_2 thickness a hydrogen terminated Si surface was used. A 2 nm SiO_2 thickness was achieved using the native oxide on the Si wafer. Further 2 nm increments in SiO_2 thickness up to 10 nm were produced by depositing SiO_2 onto Si wafers, taking into account the native oxide layer. This was done by electron-beam evaporation using *in-situ* ellipsometry to monitor the SiO_2 thickness. A J.A. Woollam M-2000 ellipsometer was used for both the native oxide and *in-situ* thickness measurements. Evaporated SiO_2 films have been found to have the correct stoichiometry [5.4], but a density that is reduced relative to thermally grown films. A single layer of SRR and square-loop elements was fabricated on these wafers using electron-beam lithography. The SRR elements (see the inset of Figure 31) had a 1 μm periodicity, 750 nm lengths, 150 nm arm widths, and a 120 nm gaps. The square-loop (see the inset of Figure 32) had a 2.23 μm periodicity, 1650 nm length, and a 300 nm arm width. For the 0 nm SiO_2 sample the resist pattern was exposed to dilute HF for 30 s to produce a hydrogen terminated surface before metallization. Then, a 5 nm adhesion layer of Ti was deposited onto the resist patterned wafer, followed by 75 nm of

Au. The metals were deposited by electron-beam evaporation at a base pressure of 5×10^{6} Torr, and a lift-off process was used to produce the elements. About 5 minutes elapsed between the Ti and Au depositions as the source was changed. During that time some of the Ti seed layer was converted to TiO_2 by the absorption of residual oxygen in the chamber [5.5]. The Ti seed layer appears at the location of highly localized surface plasmon oscillations between the Au elements and the Si substrate, and thus the inclusion of accurate spectral permittivity values in simulations for both TiO_2 and evaporated SiO_2 layers is critical to produce good agreement between simulation and measurement. The IR optical constants for Ti, TiO_2, and SiO_2 were measured on 100 nm thick evaporated films using ellipsometry as described in chapter 1.2. Figure 30 shows the results of these measurements. The IR optical constants for Au films have been discussed in Ref. 5.6.

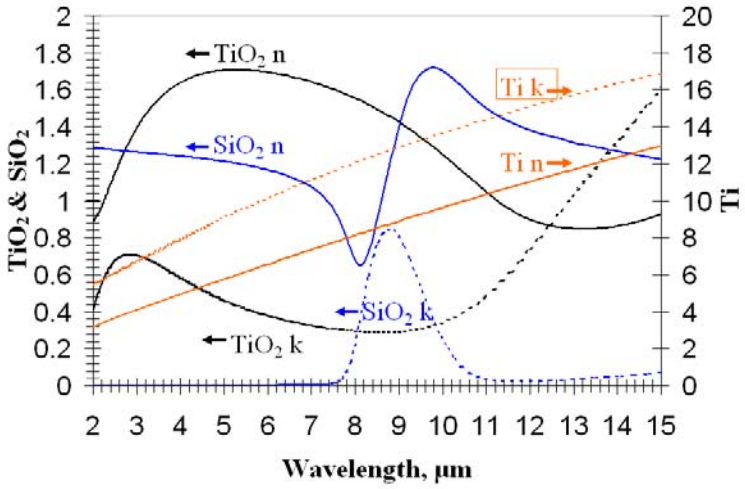

Figure 30: IR optical constants for evaporated SiO2, TiO2, and Ti measured using IR VASE system.

Simulations of the spectral transmission of the SRR structures with thin SiO_2 layers were performed using rigorous coupled wave analysis (RCWA) [5.7] incorporating the measured optical constants shown in Fig. 30. The spectral transmission was measured

using FTIR with the incident radiation linearly polarized parallel to the gap in the elements. Figures 31-32 show the measured and simulated results for an incremental increase in the SiO_2 thickness from 0 to 10 nm. The FTIR measurements with SiO_2 layers 4 nm and thicker are noiser than the 0 and 2 nm thick measurements due to the likely presence of voids in the thin evaporated SiO_2 layers. However the noise does not obscure the blue shift in the resonant frequency.

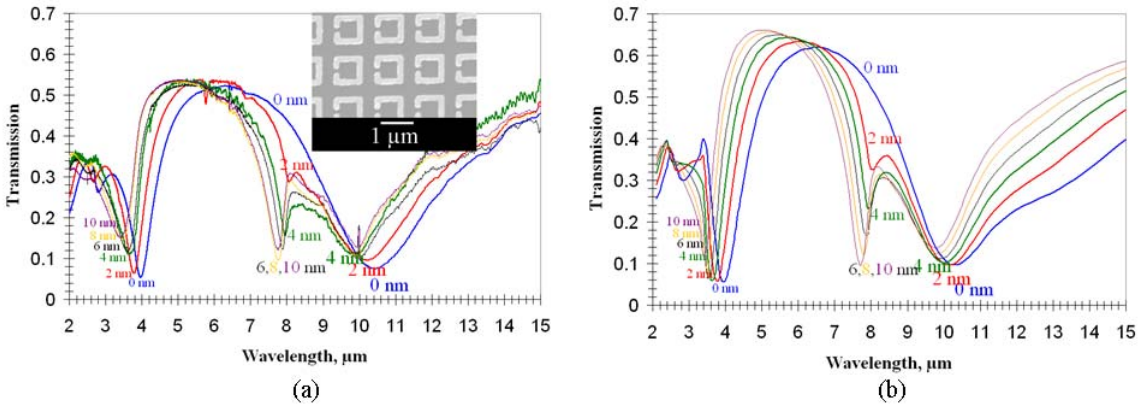

Figure 31: FTIR measurements of SRR metamaterials with SiO2 layer thickness indicated and SEM insert of fabricated elements in (a), RCWA simulations of same structures shown in (b).

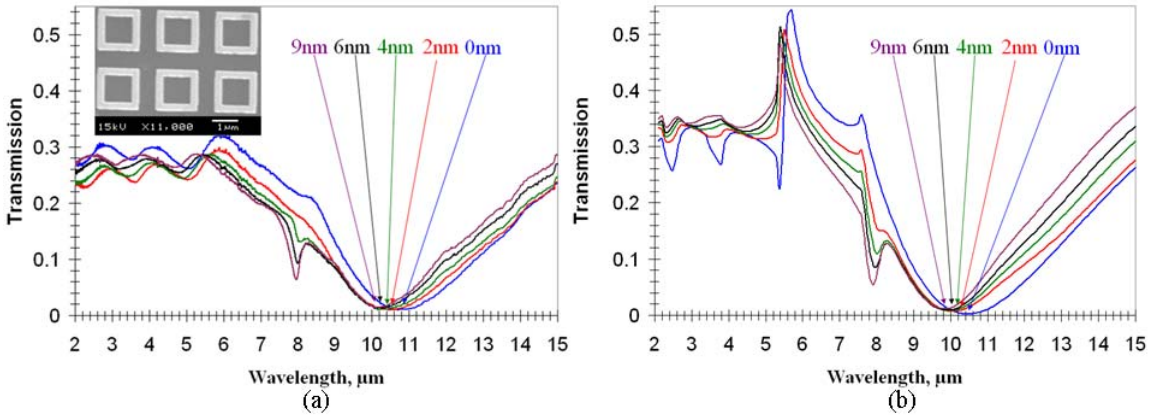

Figure 32: FTIR measurements of square-loop metamaterials with SiO2 layer thickness indicated and SEM insert of fabricated elements in (a), RCWA simulations of same structures shown in (b).

The RCWA simulation accurately reproduces the FTIR measurements when the Ti seed layer is treated as a three-layer stack consisting of 1.25 nm of TiO_2, 2.5 nm of Ti, and 1.25 nm of TiO_2 to account for the oxidation in the vacuum chamber. Some discrepancy between the magnitude in the FTIR measurements and the RCWA simulations occurred because back-side wafer reflections were not included in the RCWA modeling. The measured long wavelength resonance at 10 μm shifts to shorter wavelengths as the SiO_2 thickness increases, with the shift slowing for incremental additions over 4 nm. The SRR short wavelength resonance displayed similar behavior as the long wavelength resonance, except the resonance continues to shift for thicker SiO_2 layers. Furthermore, a transmission minimum is observed near 8 μm that is related to absorption due to coupling between the SRR or square-loop resonance and the Si-O vibrational band in the SiO_2 layer. At zero-SiO_2-thickness this minimum is not observed in either element type.

Using Eqs. 5.1-5.4 the fringing-field capacitance model may be compared to the FTIR and RCWA results for the SRRs. Based on the dimensions of the SRRs the impedance, L, was calculated to be 0.74 pH, the gap capacitance, C_g, was 0.83 aF, and the fringing-field capacitance, C_f, was 40.1 aF for zero SiO_2 thickness. To calculate the expected change in the resonant frequency based upon C_f as the SiO_2 thickness increased we considered that t_n was approximately equal to 60 nm. The analytical results are compared to the FTIR measurements and RCWA simulations in Table 5.

The most significant discrepancy between the measured and analytical results occurs as the SiO_2 thickness increases from 4 to 10 nm. This is due to strong coupling between the SRR resonance and the Si-O vibrational absorption. When the two resonances are

coupled their resonant frequencies repel each other resulting in a red shift to the measured resonance that is not accounted for in the current analytical model.

Table 5: Comparison of fundamental resonant frequency measured by FTIR to simulation and analytical calculations.

SiO_2 thickness (nm)	FTIR $\lambda_{0,1}$ (μm)	RCWA $\lambda_{0,1}$ (μm)	Analytical $\lambda_{0,1}$ (μm)
0	10.42	10.35	10.4
2	10.21	10.15	10.2
4	9.94	10.02	10.0
6	10.00	9.91	9.85
8	9.93	9.84	9.67
10	9.95	9.76	9.49

As seen in Figs. 31-32, the SRR seems to show a stronger coupling to the Si-O absorption than the square loop. The Si-O absorption near 8 μm is not visible in FTIR scans of unpatterned SiO_2 films with thicknesses ranging between 0 and 10 nm, indicating that the appearance of this feature in the metamaterial films arises due to resonant enhancement. Additionally in the zero SiO_2 thickness measurement in Figs. 31-32 only the area beneath the elements was hydrogen terminated, and thus a native oxide layer surrounded the elements. The absence of an effect for this sample indicates that only the element to substrate interface is responsible for the sensitivity to thin SiO_2 layers.

Figure 33 compares the on-resonance electric field intensity, obtained using finite-element method Ansoft HFSS software, at the interface between the metallic elements

and the SiO_2 layer of a square-loop element to a split-ring element. Both element types are scaled to resonate at 30 THz with similar bandwidths when arrayed with a unit-cell spacing which is 1.4 times the length of the element. In both simulations the electric field was a TM mode polarized in the direction perpendicular to the gap of the SRR in Fig. 33. The smaller dimensions and narrow gap of the split ring results in a maximum electric field magnitude of 1.5×10^9 V/m compared to 1×10^8 V/m in the square ring. As seen by comparing the absorption dip at 8 μm in Figures 31 and 32, the SRR showed more sensitivity to coupling to the Si-O absorption band than the square-loop, and thus we conclude that the stronger electric field at the surface of the SRR element leads to more resonantly enhanced absorption in the adjacent SiO_2 layer.

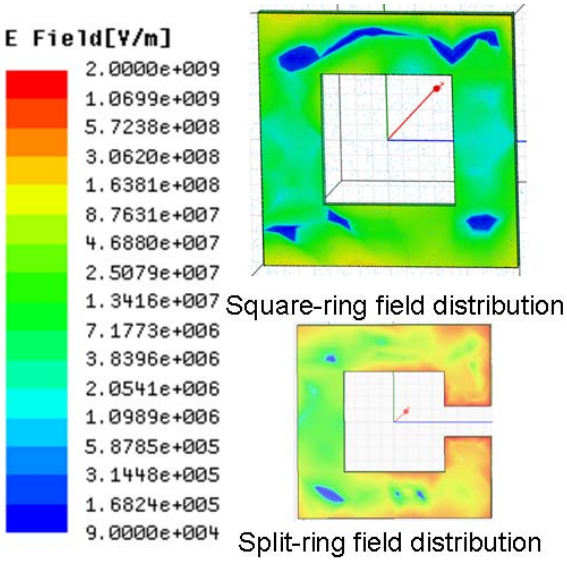

Figure 33: Electric field intensity calculated by finite-element method HFSS simulation at element to substrate interface for square ring compared to SRR element.

In conclusion, SRR resonances exhibit sensitivity to a very thin (as small as 2 nm) layer of native oxide present on a Si wafer due to adding a series capacitance to the fringing-field capacitance. The spectral locations of resonance features shift to shorter wavelength as the SiO_2 layer located between the Si substrate and the metallic elements increases in

thickness from 0 to 10 nm. The spectral shifting is similar for both square-loop and SRR elements, and thus it does not depend greatly on the fringing-field strength or on the presence of a gap. Coupling between the SRR resonance and SiO_2 absorption band was also observed to result in an additional resonance feature, whose strength is dependent on the electric field strength immediately below the metallic element, and may be useful in a sensor application to enhance detection. The thin-SiO_2 resonance shift is an important design consideration for all metamaterial structures on high-index substrates with native oxide layers present.

Equations 5.1 through 5.5 were able to analytically predict the blue shift of the resonance frequency up to a point, but this ability was limited by the appearance of a new mode resulting from a plasmon-phonon coupling event. When the plasmon and phonon mode couple normal-mode splitting occurs, and the two modes spectrally repel each other. Normal-mode splitting red shifts the metamaterial resonance resulting in divergence from the prediction of Eqs. 5.1 through 5.5. The theory must be expanded to include plasmon-phonon coupling so that a complete analytical model may be used to identify molecules within the near-fields of the elements.

5.2 Plasmon-phonon coupling in IR metamaterials

The goal of the work done in section 5.1 was to show the impact of the fringing field on the resonant frequency by changing the thickness of the SiO_2 layer in Fig. 29, and thus the fringing-field capacitance. In the course of the experiments a more interesting phenomena was observed in the form of coupling between the metamaterial resonant

mode and some sort of phonon mode. The ability of metamaterials to sense vanishingly thin dielectric layers that are not otherwise detected by spectroscopic techniques such as FTIR, ellipsometry, or Raman is of great interest. Such coupling events can further be analytically described so that the transverse optical phonon modes of the thin dielectric layer can be identified. Now IR metamaterials find a new role in surface-enhanced IR spectroscopy (SEIS). The experiments described in this section only begin to explore the possibilities of SEIS, but it lays the foundation for future work by explaining the physics of plasmon-phonon coupling in metamaterials.

It has been shown that surfaces structured with sub-wavelength dimensions can mimic surface plasmon polariton (SPP) behavior and dispersion relationships.[5.8-5.9] While these "spoof" SPP modes were originally demonstrated with metal structures that were thick compared to the wavelength, recent results have shown that spoof SPPs can occur in metamaterial elements that are thin compared to the wavelength.[5.10] In addition to propagating spoof SPP modes, metamaterials have also been shown to support trapped plasmonic-cavity modes [5.11] which are confined to the surface of a single element.

The plasmonic-cavity modes excited by IR radiation on metamaterial elements can couple to phonon modes on dielectric films within the near fields of the elements. Such plasmon-phonon coupling phenomena have been observed in piezoelectric 3-D metamaterials in the THz band, [5.12] in metal nanoparticles, [5.13] and in photonic crystals. [5.14] Plasmon-phonon coupling is a fundamental phenomenon in metamaterials which results in normal mode splitting. The eigenfrequencies that evolve

from the interaction between metamaterials and phonon modes will be shown to obey similar quantum-optical behavior as vacuum-Rabi splittings [5.15] that occur in quantum confined semiconductor structures coupled to microcavities. [5.16] Such plasmon-phonon coupling is of interest for sensing applications. Previous work has shown that metallic nanostructures may be used for near-field enhanced detection of surface phonon polaritons. [5.17-5.18] In this section an analytical model is presented to describe the eigenfrequencies and extinction line shapes resulting from the normal mode splitting. This demonstrates how plasmon-phonon coupling in metamaterials can be used for a novel SEIS technique.

The spectral response of the plasmonic-cavity modes on IR metamaterial elements may be described by a resonant frequency, ω_{mm}, and a damping rate, γ_{mm}, that is defined as the full-width half-max of the spectral transmission minimum centered at ω_{mm}. Metamaterials may be described by an LC circuit-equivalent resonance such that ω_{mm} is defined by Eq. 5.1 in the previous section. For the case of SRR elements L and C may be computed based upon the dimensions of the elements resulting in an accurate prediction of ω_{mm} as described in section 5.1. The damping rate γ_{mm} will depend upon the ohmic loss and the geometry of the elements. It may be determined from finite element method (FEM) simulations using measured optical constants as is done in this article, or it may be determined analytically using a circuit-equivalent model. [5.19] Using ω_{mm} and γ_{mm} the extinction spectrum $\alpha(\omega)$ of the uncoupled plasmonic-cavity mode may be analytically described by a Lorentzian line shape as in Eq. 5.6

$$\alpha_{mm}(\omega) = \frac{A\gamma_{mm}}{(\omega - \omega_{mm})^2 + \gamma^2} \tag{5.6}$$

where A is the amplitude corresponding to the depth of the transmission minima. We may write a similar expression for the uncoupled phonon mode given its resonant frequency and damping rate. When plasmon-phonon coupling occurs normal mode splitting will result in two new resonances with distinct eigenfrequencies and damping rates which may also have Lorentzian line shapes.

Figure 29 shows one possible cross section configuration in which a dielectric film is in contact with metamaterial elements. If the thin film has a single phonon mode within the band of the metamaterial's operation then the resulting absorption bands can be described by resonant frequencies ω_{0n} and damping frequencies γ_n. A system of two coupled damped harmonic oscillators driven by a time-harmonic field $E(t)$ is described by Eq. 5.7

$$\frac{\partial^2 x_{mm}}{\partial t} + 2\gamma_{mm}\frac{\partial x_{mm}}{\partial t} + \omega_{mm}{}^2 x_{mm} + Vx_n = \frac{q_{mm}}{m}E(t) \tag{5.7a}$$

$$\frac{\partial^2 x_n}{\partial t} + 2\gamma_n\frac{\partial x_n}{\partial t} + \omega_{0n}{}^2 x_n + Vx_{mm} = \frac{q_n}{m}E(t) \tag{5.7b}$$

where V is the coupling strength between the plasmon and the phonon mode, m is the mass of the particle, and x_{mm} and x_n describe the displacement of a plasmon and phonon respectively. The terms q_{mm} and q_n are the oscillator strengths for the time-harmonic field driving the plasmon and the phonon resonance respectively. Equation 5.7 may then be solved [5.20] to obtain Eq. 5.8.

$$V^2 = (\omega_{mm} - \omega - i\gamma_{mm}\omega)(\omega_{0n} - \omega - i\gamma_n\omega) \tag{5.8}$$

The real parts of the two solutions for ω are the eigenfrequencies of the plasmon-phonon coupled system. The imaginary portion of the solution to Eq. 5.8 is the damping rate of the normal modes. When multiple phonon modes are present near ω_{mm}, then a series of

second order linear differential equations may be formed by using n as an integer index for each phonon mode and summing over all the modes present. This may be written as an n +1 by n +1 square matrix from which the eigenfrequencies and damping rates of the coupled oscillator system may be obtained. For example, in the case of three phonon modes within the band of interest the resulting matrix is given in Eq. 5.9.

$$\begin{pmatrix} \omega_{mm} - i\gamma_{mm} & V_{2-mm} & V_{3-mm} & V_{4-mm} \\ V_{2-mm} & \omega_{01} - i\gamma_1 & 0 & 0 \\ V_{3-mm} & 0 & \omega_{02} - i\gamma_2 & 0 \\ V_{4-mm} & 0 & 0 & \omega_{03} - i\gamma_3 \end{pmatrix} \tag{5.9}$$

The terms of type $V_{n\text{-}mm}$ are coupling constants between the metamaterial plasmonic-cavity modes and the phonon modes. A unique constant is required for coupling with each phonon mode since the coupling strength of the phonon modes may vary. The phonon modes do not need to be indexed in any particular order. It is assumed that phonon modes do not couple to each other, so all $V_{n\text{-}n}$ spots in the matrix equal zero. It is further assumed that by symmetry $V_{i\text{-}mm}$ is equal to $V_{mm\text{-}i}$.

When a thin-film layer couples to the plasmonic-cavity modes on the elements the coupling stength determines how spectrally close ω_{mm} and ω_{0n} need to be for normal mode splitting to occur. Strong coupling results in ω_{mm} and ω_n repelling each other spectrally forming a forbidden energy gap, Ω, that may be measured experimentally. This behavior is analogous to quantum level repulsion or anti-crossing. The energy gap Ω may be related to the coupling constant V by Eq. 5.10. [5.21]

$$\Omega = \sqrt{4V^2 - \left(\gamma_{mm} - \gamma_n\right)^2} \tag{5.10}$$

When ω_{mm} and ω_{0n} are spectrally spaced by energy greater than Ω, strong coupling will not occur. Thus, the matrix formulation for multiple phonon modes should only be needed in cases where modes lie within Ω of each other. Otherwise the problem reduces to the case of two uncoupled damped-harmonic oscillators.

As Ref. 5.18 points out, the plasmonic-cavity modes on the elements will couple to surface-phonon modes rather than the transverse-optical (TO) phonon mode. Surface-phonon modes can occur in dielectric thin films with sufficiently strong absorption peaks to produce negative permittivity. Since the TO phonon mode may be used to identify a material or feature in a SEIS experiment it is important to relate the characteristic frequency of the surface-phonon to the dielectric permittivity, $\varepsilon(\omega)$, determined by the TO mode. This may be done by considering the dispersion of the surface-phonon mode following the analysis of Fuchs and Kliewer. The surface-phonon will fall within a range defined by the maxima of $\mathrm{Im}[-1/\varepsilon(\omega)]$ and $\mathrm{Im}[-1/(\varepsilon(\omega)+1)]$. [5.22-5.23] For thin films, the high frequency limit defined by $\mathrm{Im}[-1/\varepsilon(\omega)]$ corresponds to the phonon mode on the top (element side) interface. The low frequency limit defined by $\mathrm{Im}[-1/(\varepsilon(\omega)+1)]$ corresponds to the phonon mode on the bottom (substrate side) interface. Depending upon the thickness of the dielectric layer it is possible for the surface phonon mode frequency to fall somewhere within this range and blue shifts as the thickness increases as observed in section 5.1.

In order to experimentally verify strong coupling between metamaterial plasmonic-cavity modes and thin-film phonon modes, an experiment was designed where two different

types of metamaterial elements were built on a 10 nm thick SiO_2 film. A 10 nm film thickness was chosen so that a sufficient percentage of the near fields of the elements would be confined in the thin-film and strong coupling would occur. Furthermore, keeping the oxide film thickness small relative to the phonon-resonance wavelength prevents the appearance of an absorption peak related to the TO phonon mode that would then be detected regardless of surface-enhanced effects. The absence of the TO mode is necessary to confirm the validity of Eq. 5.8 and was checked by Fourier transform infrared spectrometer (FTIR) measurements. SiO_2 was selected for the thin film because it is easy to deposit at an accurate thickness, and the Si-O phonon absorption band is near 9 μm which makes it ideal for coupling experiments in the thermal IR. The SiO_2 was deposited onto a Si wafer using electron-beam evaporation monitored by *in-situ* ellipsometry using a J.A. Woollam M-2000 system. The total SiO_2 thickness of 10 nm included the native oxide layer.

In order to show the expected anti-crossing behavior split-ring resonator (SRR) metamaterial elements were built on the SiO_2 film with different element dimensions. The SRR elements were fabricated using electron-beam lithography and a lift-off process. The elements were metalized with 75 nm of Au with a 5 nm Ti adhesion layer by electron-beam evaporation. An SEM image of the fabricated SRR elements is shown in Fig. 31 along with a schematic showing labeled dimensions in Fig. 28. Changing the dimensions of the element allowed the plasmonic-cavity resonance frequency ω_{mm} to be effectively scanned across the surface-phonon mode in separate metamaterial arrays. Table 6 shows the calculated values for the resonant frequency and the uncoupled

damping frequency of the SRR's in the absence of the oxide's phonon mode. These calculations were done using finite-element method (FEM) simulation (Ansoft HFSS) and by assuming in the model a dispersionless SiO_2 film with refractive index equal to 1.45. The dispersionless SiO_2 was included in order to account for the fringing-field capacitance contribution to the resonant frequency as described by Eq. 5.1. The FEM simulation also included the effects of the seed layer and finite element conductivity using measured optical constants.

An additional experiment was conducted using a shorted SRR or square-loop element to investigate the role of element type and oscillator bandwidth on anti-crossing. A single design was used for the square-loop experiment with element width w of 200 nm, length L of 1400 nm, and periodicity of 1750 nm. These dimensions were chosen such that ω_{mm} was nearly equal to the surface-phonon mode based on FEM simulations on a dispersionless SiO_2 film. This allowed the coupling constant V to be measured for the case of square-loop elements and compared to the SRR elements.

Table 6: Unit cell dimensions for SRR elements with array periodicity and FEM simulated ωmm and γmm.

L, nm	g, nm	w, nm	Period, nm	ω_{mm}, meV	γ_{mm}, meV
520	80	100	720	186	96.7
590	100	120	830	165	85.8
660	110	140	930	148	71.9
690	110	140	970	141	69.7

The measured dielectric function ε(ω) of evaporated SiO_2 are shown in Fig. 34(a). For the thin layer of evaporated SiO_2 used in the experiments the TO mode was measured to

be at 130 meV and the surface phonon mode was measured to be at ω_{0n} = 146 meV based on fitting to Eq. 5.8. This value falls within the range of the Fuchs-Kliewer surface-phonon mode and lies between the peaks in the energy loss functions plotted in Fig. 34(b). The damping frequency of the surface-phonon mode was measured to be γ_n = 11.3 meV. Figure 34(c) shows the lorentzian line shapes for the plasmon and phonon modes using Eq. 5.6 for the case where ω_{mm} is nearly equal to ω_{0n} at 141 meV. The broken line in Fig. 34(c) shows the convolution of the two lines that would correspond to the extinction spectrum if coupling did not occur.

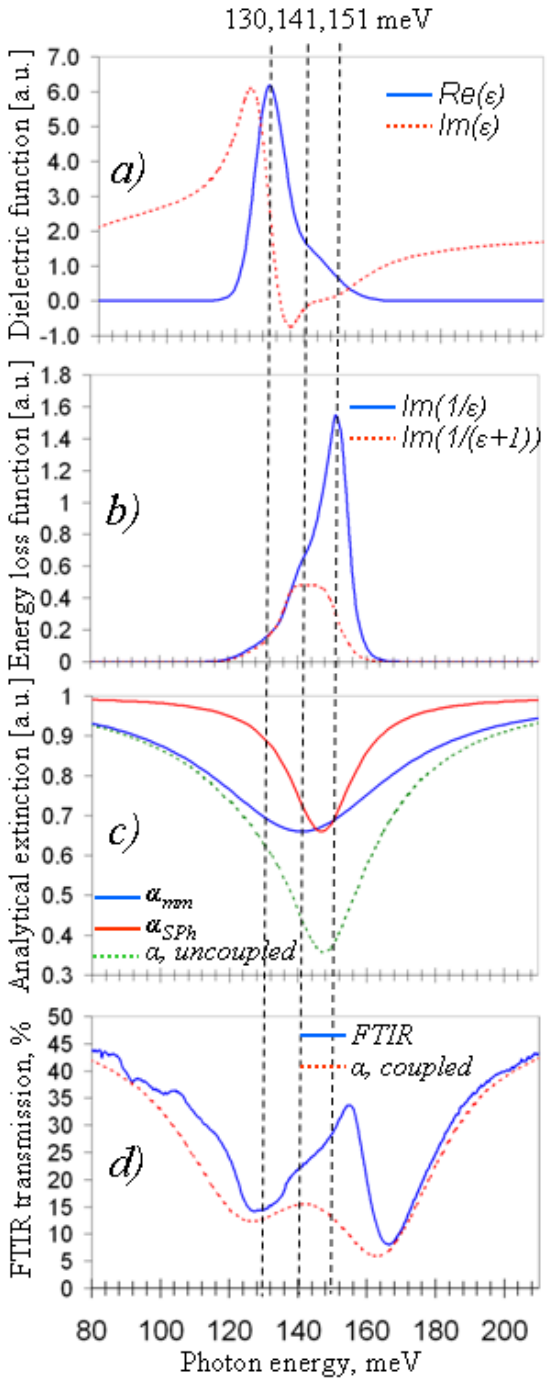

Figure 34: (a) Dielectric function for evaporated SiO_2 measured by IR ellipsometry. (b) Calculated energy loss function for ellipsometry data showing the allowed range of the surface phonon mode between the peaks of Im(1/ε) and Im(1/(ε+1)). (c) Lorentzian line shapes for metamaterial resonance, the surface phonon mode, and the resulting analytical extinction peak if the two modes were uncoupled. (d) FTIR measurement for the same

Figure 34(d) shows the FTIR measured extinction spectrum and the analytical line shape based on the solutions Eq. 5.8 substituted into Eq. 5.6. It is apparent from the comparison of Fig. 34(c) to 34(d) that coupling occurs, and the surface-phonon mode is found to lie outside the Fuchs-Kliewer allowed region due to normal mode splitting.

Figure 35 shows the agreement between FTIR measurement and FEM simulation for the case in which ω_{mm} is nearly equal to ω_{0n} using SRR elements. The spectrum shown in Fig. 35 is in wavelength units, but values are converted to energy units when comparing to the analytical model. The two resonant modes repel each other resulting in new coupled modes that produce a unique dual resonance in the transmission spectrum.

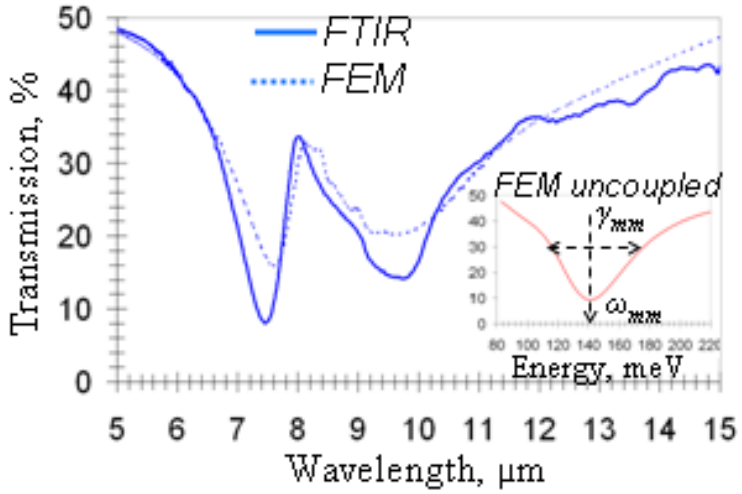

Figure 35: Data for experiment with ωmm = ω0n; FTIR measurement (solid line) FEM simulation with measured optical constant (broken line), inset shows FEM for dispersionless SiO2 used to determine ωmm and γmm.

By considering the spectral location of the two resonant minima in Fig. 35 to be the measured eigenfrequencies of the coupled system, Ω for this system is equal to 39.5 meV. The insert to Fig. 38 shows a separate FEM simulation of the same SRR on a dispersionless SiO_2 layer in order to determine ω_{mm} and γ_{mm}. The uncoupled SRR

damping frequency γ_{mm} was found to be equal to 69.7 meV. According to Eq. 5.10 this results in a coupling constant V equal to 27.4 meV.

Figure 36 shows the collection of FTIR data that was accumulated in the seven separate experiments with the SRR element arrays with dimensions shown in Table 6. Although the data shown in Fig. 36 are for coupled modes, the plasmonic-cavity portion of the hybrid mode is distinguished in blue while the Si-O surface-phonon mode portion is shown in red. As the blue plasmonic-cavity mode is scanned across the IR band from 5 to 15 μm, anti-crossing behavior is observed in the red Si-O phonon mode. An energy gap where neither the plasmon nor the phonon mode have a resonance minima forms around ω_{0n}.

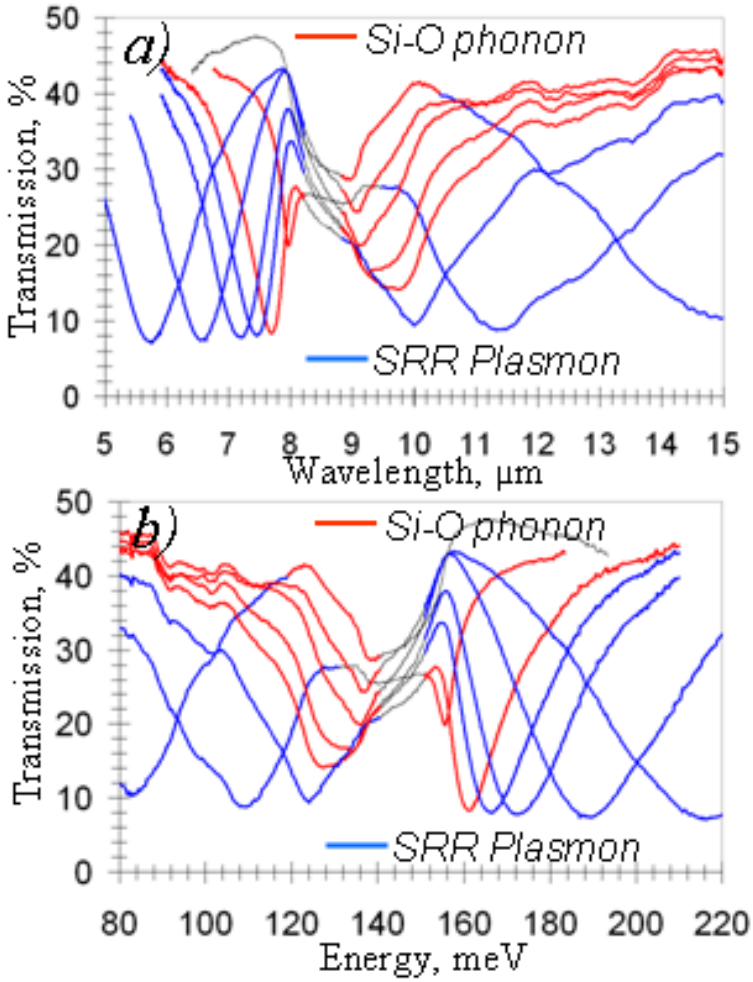

Figure 36: FTIR measurements for different SRR unit cells with dimensions in Table 5. The normal mode extinction lines are drawn in red or blue for correspondence to the phonon or plasmon mode respectively.

Based on the measured results of Fig. 36, Fig. 37 shows the dispersion curves where the eigenfrequencies of the plasmon-phonon coupled system are plotted versus the collection of ω_{mm} values found in Table 6. The FTIR data points in Fig. 37 were determined from the spectral location of the resonance minima in Fig. 36. The FEM data points were determined from the spectral location of the resonance minima from simulations using measured optical properties. The analytical model is shown as the solid curve which was calculated from the measured value for V, ω_{0n}, γ_{0n} and the values for ω_{mm} and γ_{mm} from

Table 5. The broken lines in Fig. 37 show the light line (eigenfrequency equals uncoupled SRR mode energy) and the resonant energy of the phonon mode. Away from the energy gap where ω_{mm} is equal to ω_{0n}, the data should converge to these values. The dispersion curves in Fig. 37 demonstrate agreement between the measurements, simulations, and analytical model.

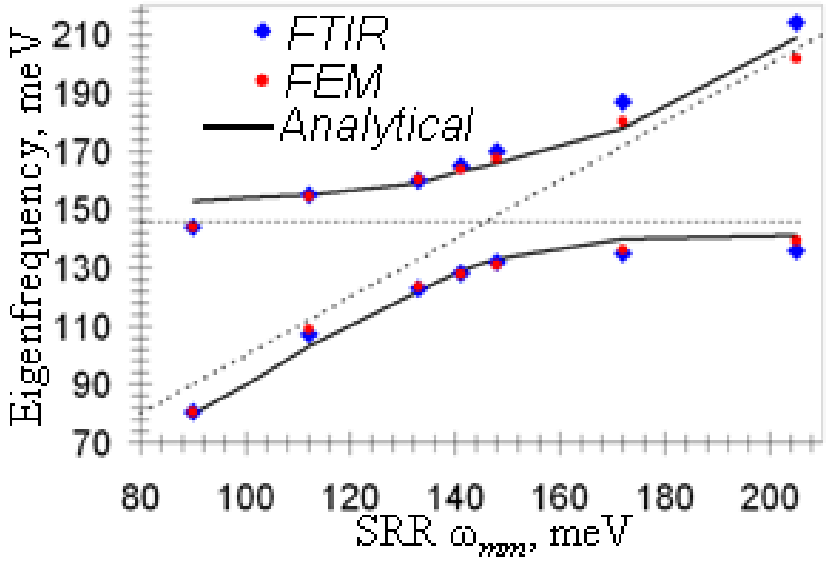

Figure 37: Dispersion relationship for SRR plasmonic-cavity modes coupled to Si-O phonon modes. FTIR data in blue data points represent resonant minima of peaks from Fig. 36. FEM simulations using measured optical properties are shown in red data points, and dispersion curve for coupled oscillators calculated from Eq. 5.6-5.10 is shown as the solid lines.

Figure 38 shows results from FTIR measurement and FEM simulation for the square-loop element with ω_{mm} equal to ω_{0n}. Compared to the SRR element the energy gap between the two resonant minima is 17 % smaller at 32.7 meV and the coupling constant is 81% larger. This discrepancy arises from the increased strength of the square-loop resonant mode relative to the SRR, as indicated by the square-loop's deeper band-gap. The insert to Fig. 38 shows the simulated results for the uncoupled square-loop element on dispersionless SiO_2, and from the FEM data γ_{mm} is determined to be 116 meV. Based on

the measured value for Ω and Eq. 5.10 the coupling strength V for the square-loop elements is 49.6 meV.

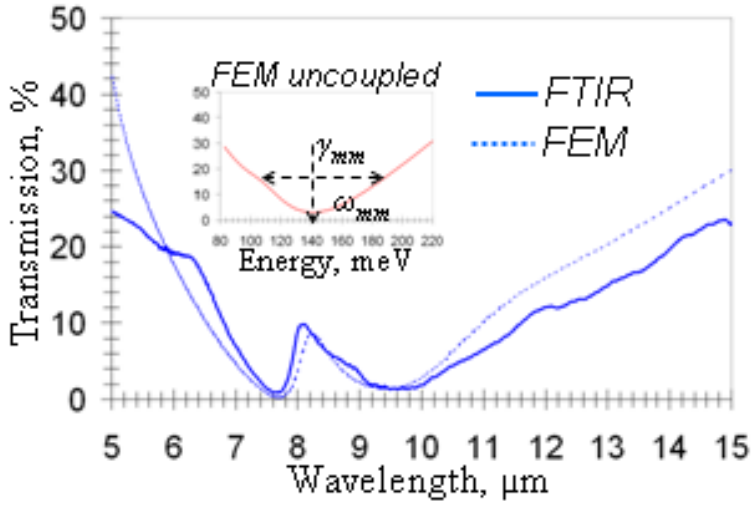

Figure 38: Data for experiment with ωmm = ω0n for square-loop elements; FTIR measurement (solid line) FEM simulation with measured optical constant (broken line), inset shows FEM for dispersionless SiO2 used to determine ωmm and γmm.

In Ref. 5.18 one of the normal modes was always found to be in the allowed region of the Fuchs-Kliewer surface phonon. In that case it was concluded that the mechanism behind the surface-enhanced detection was related to a polariton mode rather than plasmon-phonon coupling. Although the experiments in this article and Ref. 5.18 are similar, the SRR elements used here have a stronger resonance than the widely spaced dipoles of Ref. 5.18. In the case of strong coupling it is possible to push the normal mode out of the range of the Fuchs-Kliewer surface phonon as shown in Fig. 34. The affects of resonator strength and near-field enhancement on normal mode splitting are an important area of future work.

Although the stronger resonant mode of the square-loop results in a smaller Ω between eigenfrequencies, the coupling strength between the SRR and Si-O phonon mode is

weaker than the coupling to the square-loop elements. This is consistent with Eq. 5.10 which says that for a given Ω the coupling strength V increases with the mismatch between the damping frequencies of the plasmon and phonon mode. However, the use of Eq. 5.6-5.10 to predict eigenfrequencies for any given set of oscillators depends upon *a priori* knowledge of either the coupling strength or the energy gap. This is because the current model has no means of accounting for the relative amplitudes of the respective plasmon or phonon resonances. Thus, the damped-harmonic-oscillator model is useful as a tool to understand the plasmon-phonon coupling behavior, but has limited utility as a predictive tool.

Using a tunable metamaterial, such as has been shown in recent experiments, [5.24-5.26] the metamaterial resonance may be scanned to within Ω of multiple phonon modes for a given material. Many materials such as ceramics and organics may be identified by their unique collection of TO phonon modes which are related to surface-phonon modes of resonant frequency ω_{0n} and damping rate γ_n. By examining an FTIR spectrum for a set metamaterial resonance states, with known ω_{mm} and γ_{mm}, the resulting energy gaps could be measured and Eq. 5.6-5.10 could be used to fit ω_{0n} and γ_{0n}. This approach may be used to fingerprint materials with IR-active phonon modes placed in close proximity with the metamaterial elements. The technique is particularly suited for highly localized detection of nanoscale cells or particles since strong coupling only occurs within the near fields of the metamaterial elements. Plasmon-phonon coupling also significantly enhances the ability to sense very thin dielectric layers as layers as small as 2 nm were

able to be detected in Ref. 5.18 and in section 5.1. Thus, metamaterials may be used as nanoscale probes for SEIS.

Strong coupling between plasmonic-cavity modes and phonon modes can occur with all planar metamaterial elements. This was demonstrated by showing that the characteristic anti-crossing dispersion relationship of coupled plasmon-phonon modes occurs in a single layer of SRR elements in contact with a 10 nm thick SiO_2 thin film. Similar mode splitting behavior was observed for square loop elements. These experimental results were shown to be in agreement with numerically simulated results using measured material parameters and an analytical damped harmonic oscillator model. Plasmon-phonon coupling in planar metamaterials may be used to facilitate SEIS based probes.

CHAPTER 6: TUNABLE IR METAMATERIALS

As discussed in chapter 2, the purpose of a metamaterial is to enable absolute local control of the electromagnetic properties ε and μ of a composite material through lithographically defined elements. Tunable metamaterials are interesting because we can extend the absolute control of ε and μ beyond the design stage to enable surfaces with electronically controlled optical properties. There are many potential applications including: filters and waveplates that can change their band of performance on command, optical memory for robust data storage, SEIS sensors and probes (chapter 5), no-moving-parts beam steering for laser communications, solar power concentration, infrared energy harvesting, and many more. Such potential-future inventions begin with the ability to dynamically tune the resonant frequency of a metamaterial on command.

To significantly change the resonant frequency requires elements or surrounding dielectric layers which may have a large change in optical properties that may be electronically controlled in some way. It must be emphasized here that metamaterials are about near-field control, so what influences the resonant frequency is that which falls within the near fields of the elements – as was demonstrated by the SEIS experiments in chapter 5. Therefore the techniques used in traditional optoelectronic modulators are insufficient because they depend upon a small change in refractive index with radiation propagating though crystals that are many wavelengths thick. Applying a bias across a piezoelectric material such as $BaTiO_3$ to achieve $\Delta n = 0.01$ will not make a tunable

metamaterial. Liquid crystals are another possibility, but there are problems with this method which will be considered in this chapter. A tunable metamaterial requires something more like $\Delta n = 1$ to 10 to produce a significant optical change that is local (within the near fields) to the elements. This transition must be both repeatable and reversible. If we consider Eq. 2.1 it is clear that there is really only one way to achieve such a transition; the plasma frequency must be changed relative to the operation frequency by inducing an insulator to metal transition.

Insulator-to-metal transitions can occur in semiconductors and satisfy the local large index change and reversibility requirements for tunable metamaterials. In general an insulator-to-metal transition occurs when free carriers are injected or generated in the semiconductor. This may be done by charge depletion in a Schottky diode, photo generated electron-hole pairs, ion injection by intercalation, or by a symmetry-raising phase transformation. Schottky diodes, photo generated electrons, and phase transformations will be considered in this chapter. Ion intercalation is the basis of electrochromic materials and will be considered as a topic for future work. In all cases a sufficient concentration of free carriers must be generated such that the plasma frequency becomes large relative to the frequency. At infrared frequencies this can be a challenging task because the carrier concentration must be in excess of 10^{19} cm^{-3} for any significant change in permittivity to occur. It is far easier to produce tunable metamaterials at THz or lower frequencies due to lower plasma frequency requirements. Alternative methods such as liquid crystals and photochromics work well in the visible band, but fail in the IR due to a lack of transparent conductors and photon energy much smaller than the

bandgap. These factors make the infrared the most challenging portion of the electromagnetic spectrum to achieve tunable metamaterials.

6.1 Free carrier depletion in Schottky diodes for tunable metamaterials

Metamaterial filters are described by a Q factor which is defined as the ratio of the center frequency to the full width half max of the resonance. Compared to radio frequency (RF) filters which may have Q on the order of 1000, it is difficult to build a metamaterial filter with a Q higher than 10 because of limited conductivity in all metals in the mid-IR. Although static metamaterials have been demonstrated, thus far there has been limited progress in creating a tunable surface in the IR. In the RF, tunable metamaterials have been realized by integrating varactor diodes [6.1] or PIN diodes [6.2] between individual elements. This presents a challenge in the IR as diodes of the proper IR frequency response are not common and it is difficult to integrate them between sub-wavelength sized antenna elements.

Alternative RF tuning approaches have made use of substrates with electrical properties that change with an applied bias potential [6.3] such as the piezoelectric effect. One such solution in the IR is to form a DC Schottky diode between a metallic aperture FSS and high-donor-impurity silicon (Si). This results in a permittivity contrast between the n^+ Si and the electrically neutral depletion layer. By changing the width of the depletion layer with an applied bias potential, the resonance frequency may be modulated. Such a technique as been demonstrated as an effective method at frequencies around 1 THz [6.4]. This is because at 1 THz a smaller plasma frequency, and thus lower donor

impurity, is required to achieve a permittivity contrast as seen in Eq. 2.1. This section presents measured results for a single layer DC Schottky diode metamaterial device, as well as simulated data for a two layer device to illustrate the limitation of the technique in the IR. These results serve to illustrate the limitations of the DC Schottky diode approach inherent at frequencies in excess of 30 THz due to the high donor-impurities required for a permittivity contrast to be observed.

The tunable device consists of an arbitrarily thick n^+ Si layer with a depletion layer of finite width beneath a metal sheet patterned with aperture-type elements. Simulations of the tunable metamaterial device were conducted using Ansoft's finite element method based HFSS software. In order to correctly model the response of the device, variable-angle spectroscopic ellipsometry was used to measure the permittivity and loss tangent of the n^+ Si and low impurity n Si. This data is shown in Fig. 39 for both materials. The low-impurity n Si is taken to represent the permittivity of the depletion layer. The n^+ Si was doped with Sb to a concentration of 4×10^{18} cm^{-3} and has both a lower permittivity and a higher loss tangent than the low-impurity Si. The measured dispersion in both materials is included in the HFSS simulation [6.5]. The depletion layer width W was calculated using the equation:

$$W = \sqrt{\frac{2\varepsilon_s}{qN_D}\left(V_{bi} - V - \frac{kT}{q}\right)} \qquad (6.1)$$

where ε_s is the DC permittivity of Si, N_D is the donor impurity, V_{bi} is the Schottky barrier height, and V is the applied bias potential [6.6]. The device was biased from +2 to -4 V during operation. Based on calculation, the width of the depletion region changed from 5 nm to 37 nm under this bias. When the width of the depletion layer was changed, the

local permittivity underneath of the aperture elements changed. This caused a change in the magnitude of reflectivity that was observed in the simulation.

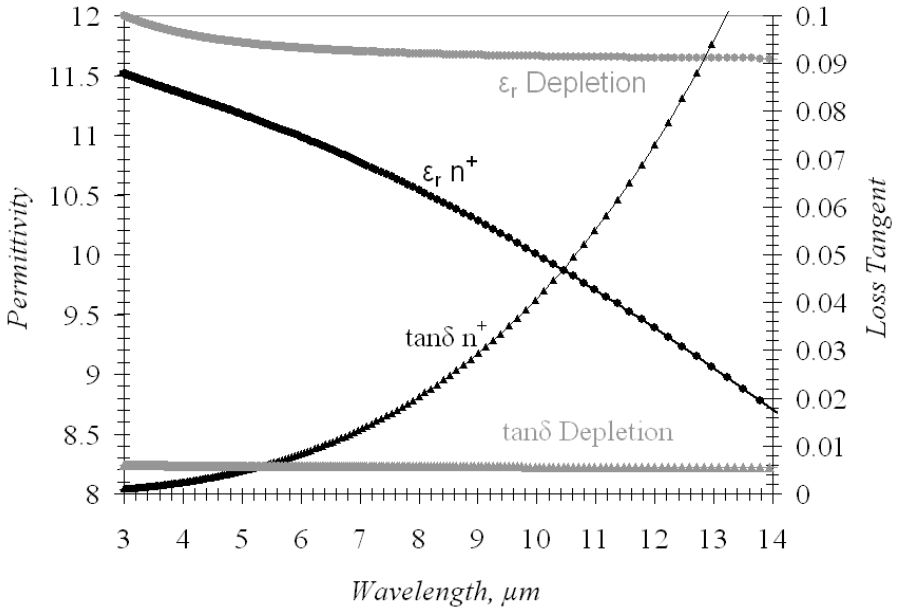

Figure 39 Ellipsometry measurement of high donor impurity n+ Si, and low donor impurity n Si.

A film of Al was electron-beam evaporated onto the backside of a high-impurity Si wafer. The sample was then annealed at 450 ºC in an Ar ambient for 30 minutes to create a eutectic reaction and form an ohmic contact. The front side of the silicon surface was hydrogen terminated by an HF dip, just prior to introducing it in a vacuum chamber for a Pt deposition. Next, 60 nm of Pt was deposited on this hydrogen terminated surface by DC magnetron sputtering to form the rectifying contact. Pt is well known to have a large barrier height (0.9 V at 300 K [6.6]) on n type Si. Electron-beam lithography was used to pattern periodic cross elements on the surface of the Pt film. The cross pattern had an arm length of 1.8 μm, a periodicity of 2.0 μm, and an element width of 300 nm. A physical sputter etch was then used to etch the cross aperture pattern into the film. Figure 40 shows an SEM image of the cross aperture FSS. To complete the test device electric

leads were attached to the ohmic and rectifying contacts using conductive epoxy. The breakdown voltage of the Schottky diode was measured to be -5 V, the turn on potential was 0.2 V, and the saturation current was 0.3 mA.

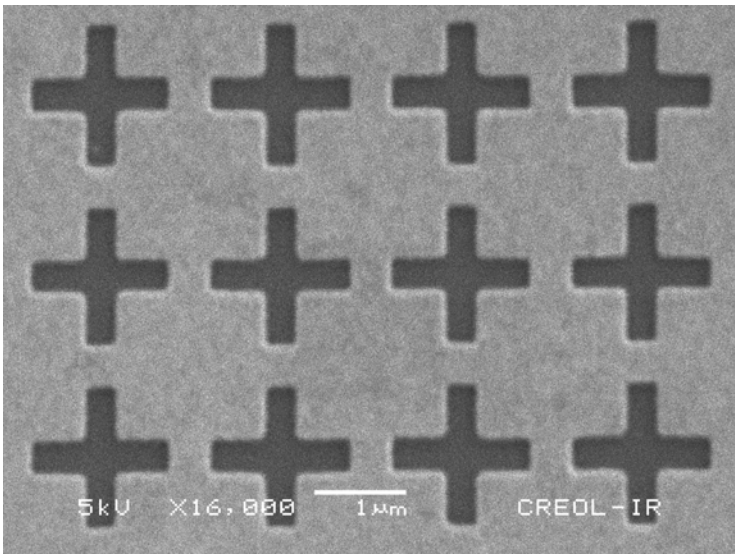

Figure 40 SEM image of measured FSS structure – cross aperture elements.

Measurements of the spectral reflectivity were made using a Fourier transform infrared spectrometer (Perkin Elmer Spectrum One) using unpolarized light with wavelength ranging from 3 μm to 14 μm. A DC bias was applied to the sample, and reflectivity measurements were made at 0 V, +2 V, and -4 V. Forward bias had the effect of increasing the reflectivity while reverse bias decreased the reflectivity across the spectrum. There was little spectral shifting of the features during the measurement. However, the change in the magnitude of reflectivity was repeatable over several trials and five different devices. As shown in Fig. 41, the change in the magnitude of reflectivity ranges from 2 to 5% across the 3 to 14 μm band. To check the validity of the results one of the tunable IR-FSS was burned out by biasing beyond the breakdown voltage and the measurement was repeated. The change in the magnitude of reflectivity in this measurement was less than 0.2 % -- falling in the noise of the instrument.

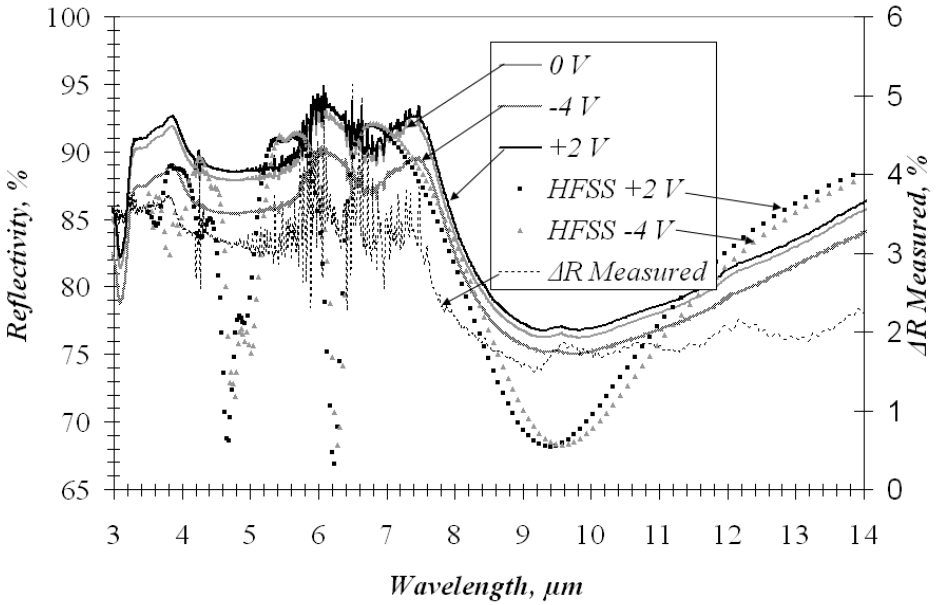

Figure 41 Measured spectral reflectivity under applied bias potential (solid lines). HFSS results for calculated depletion region thickness under same bias (dotted lines).

Simulations (figure 41) predicted a 2-5% change in reflectivity with a Q of 2.7 compared to 2.0 in the measured data. The simulations also predicted a 200 nm change in the resonance frequency moving from 9.4 to 9.6 μm. Although a change in magnitude was observed, there was no significant change in the resonance frequency. The lack of clear resonant frequency movement is due to the weak resonance that occurs when the elements are on a low resistivity substrate. Such a broad-low-Q resonance loses sensitivity to surrounding layers. The change in reflected power was likely due to the change in conductivity at the interface between depletion states.

Although a permittivity difference between the depletion region and the n^+ Si was desired, increasing the donor impurity concentration had the effect of limiting the change in thickness of the depletion region. The depletion region under bias should be greater than the near-field penetration depth which is estimated to be around 60 nm in chapter

5.1. High donor impurity also limits Q because the low resistivity substrate can allow charge density waves to propagate out of resonating modes. The concentration used in this experiment was chosen to be at the optimum point based on calculation and ellipsometry measurements. Given these limitations, this can be taken to be the best possible result for a single surface tunable IR-FSS using the DC Schottky diode method.

One possible way to further increase tunability is to cascade several surfaces of this type together with high donor impurity polycrystalline Si to fabricate a more useful device. One possible layout, as shown in Figure 42, for a multilayer device consists of a wire grid FSS separated from the previous cross slot FSS by a $\lambda / 4$ thick layer of n^+ Si. The wire elements were spaced by half the periodicity of the cross slots and shared the same width. The simulation is taken to be biased such that a rectifying contact exists at each metal / Si interface. The simulated results for a multilayer device are shown in Figure 43. Near resonance the change in reflectivity increases to greater than 10% compared to 4 or 5% in the single layer device. The change in resonance frequency is still small at 300 nm as the resonance frequency changes from 7.3 to 7.6 μm.

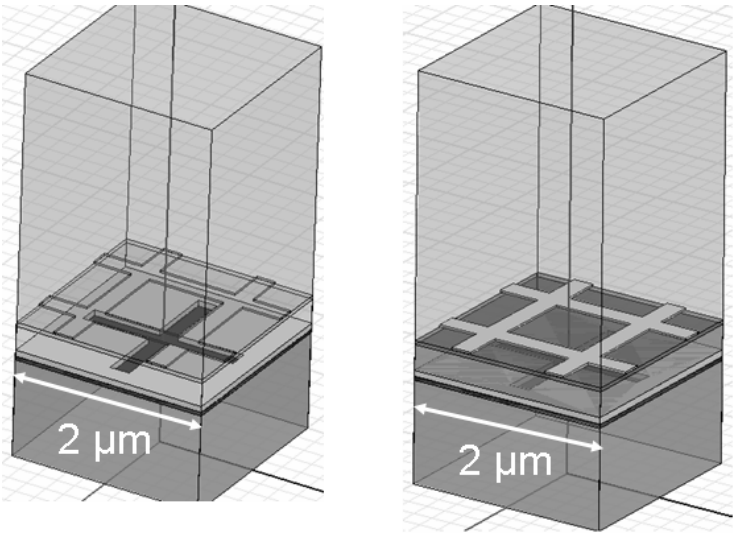

Figure 42 HFSS model for multilayer design: left, bottom layer cross aperture surface, right, top layer wire grid FSS.

Based on agreement between simulated and measured results it can be inferred that the DC Schottky contact method can yield a 5% change in reflectivity per each layer in the IR. However change in reflected power is not nearly as important as change in resonance wavelength, and a 200 to 300 nm shift is limited.

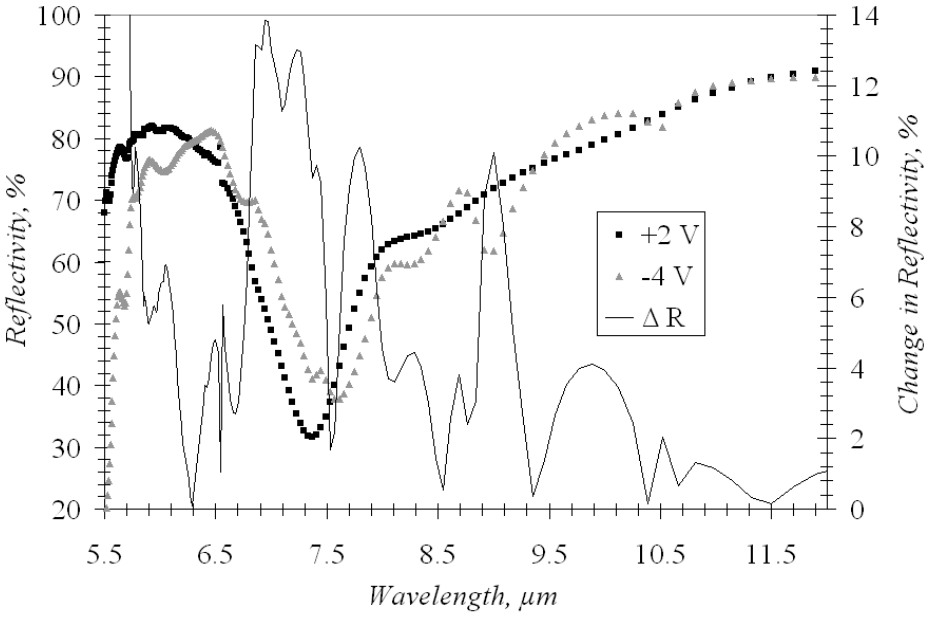

Figure 43 Change in reflectivity under bias from +2 V to -4 V for a simulated multilayer design.

A single-surface tunable metamaterial device was designed, fabricated, and tested. Compared to competing technologies, the DC Schottky diode approach is much cheaper and easier to fabricate, but is limited to around a 5 % change in reflectivity per layer with 10% possible using a two-layer design. The DC Schottky diode had the potential to achieve the desired goal of an inexpensive electronically controllable surface. However, due to the high donor impurity required to produce a permittivity contrast in the IR, the barrier height between the metal and semiconductor decreases as the Fermi energies converge with increased donor concentration. This results in a diode with a low breakdown voltage, and limited change in the size of the depletion region. Metamaterials also become weak resonators as the conductivity of the depletion region increases and shorts the currents on the elements. This problem may be addressed by selectively doping the semiconductor such that only portions were n^+. For example only the region underneath the gap in a split ring resonator might be doped instead of the entire substrate. Regardless of such possible improvements the permittivity contrast in the IR will always be small in a depletion region. We therefore conclude that depletion region tuning is unfeasible for metamaterials at frequencies greater than 1 THz.

6.2 Liquid Crystal Tunable Metamaterials

It has been suggested that liquid crystal (LC) cells may be used as a superstrate layer for tunable metamaterials [6.7]. By applying an electric field across the LC a change in effective index of $\Delta n = 0.8$ is claimed in the IR by Ref. 6.7 based on Ref. 6.8. Although it is possible to obtain such a Δn in the visible using high birefringence LCs, in the IR a $\Delta n = 0.4$ is more realistic [6.9]. This is still a sufficient change in refractive index to predict some resonance frequency tuning using the approximations in Ref. 6.7.

The results of an HFSS simulation for a cross FSS element using ideal conditions are shown in Fig. 39. A waveport matches impedance at the bottom of the unit cell, so reflections from the bottom of the polyimide layer are neglected in the simulated transmission. The metal elements were assumed to be PEC, the LC is lossless, and the polyimide layer underneath the elements had a constant permittivity ($\varepsilon_r = 2.89$) and no loss. The IR permittivity of the LC changed from 2.4 (ordinary axis) to 3.8 (extraordinary axis) based on Ref. 6.9. Any thickness may be used for the LC in an ideal simulation, so a thickness of 2.38 μm was chosen such that the LC was $\lambda_{eff}/2$ thick at a wavelength of 8 μm. Under these conditions a relatively sharp resonance behavior is predicted with some degree of tuning as shown in Fig. 44.

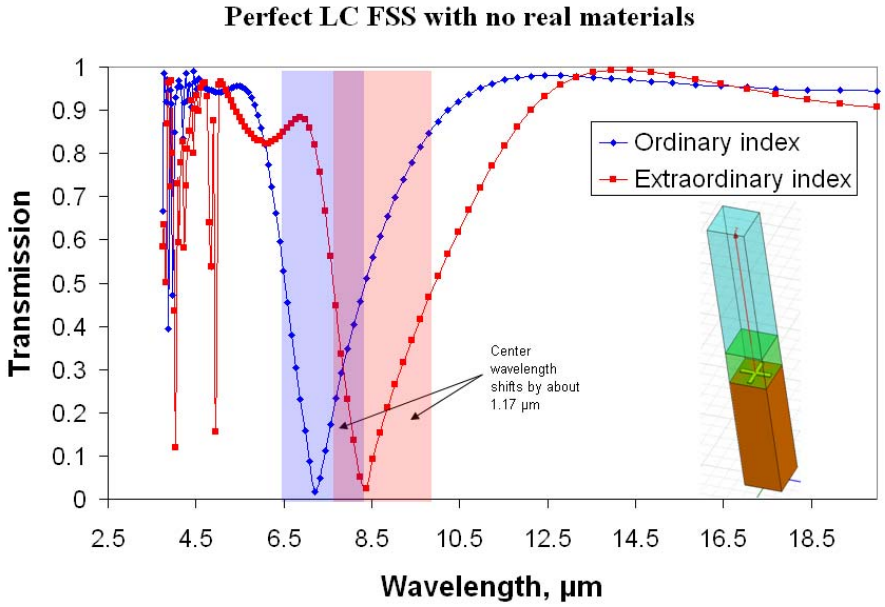

Figure 44: LC FSS simulations in the IR using ideal conditions. The unit cell used in HFSS is shown on the right where the green layer is the LC, the orange layer is the polyimide, and the blue layer is the air box. The cross FSS element sits on the polyimide layer submerged in the LC as in Ref. 6.7.

Next we consider an intermediate step where loss is added to the elements, polyimide, and LC, but the full LC cell and polyimide dispersion are not yet considered. The permittivity of the polyimide is 2.89 as before, but now the loss tangent is 0.023 instead of 0. The LC has the same change in permittivity as before, but the loss tangent is now 0.026. This is based on IR ellipsometry measurements of similar LC materials taken in the IR Systems Lab at UCF. The metal elements are now aluminum, and measured dynamic conductivity values from the ellipsometer are used. In addition to adding loss a realistic LC thickness is considered. Due to uniformity concerns LCs are typically no thinner than 10 µm, so a thickness of 10 µm is used in the simulations. An LC thickness of 1 µm was used in Ref. 6.7, but this is not realistic. The results of this intermediate simulation are shown in Fig 45.

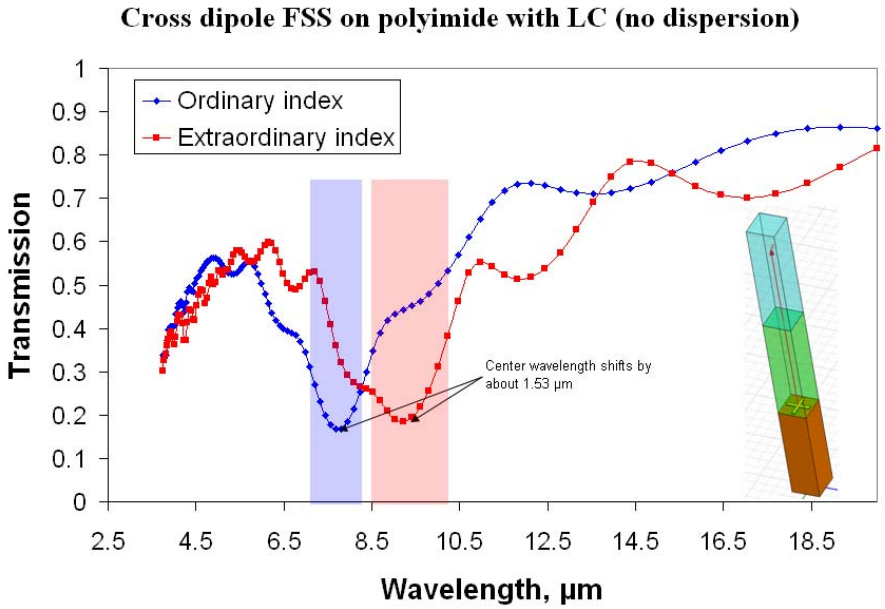

Figure 45: LC FSS simulations including constant permittivity, loss, and a realistic LC thickness. The unit cell used in HFSS is shown on the right where the green layer is the LC, the orange layer is the polyimide, and the blue layer is the air box. The cross FSS element sits on the polyimide layer submerged in the LC as in Ref. 6.7.

In order for molecular alignment to occur in the LC cell it is required that the LC be bound by polyimide layers. With metal elements sitting on the bottom layer of polyimide it is important to include a polyimide "rubbing layer" on top of the LC. This "rubbing layer" is mentioned in Ref. 6.7, but not included in their simulations (in Ref. 6.7 compare Fig. 40 to Fig. 45). The thickness of this layer is taken to be 1 µm to reduce the loss that would result from a thicker layer. In addition the permittivity and loss of polyimide is not constant in the IR. The IR properties of polyimide have been measured by the IR Systems Lab at UCF using ellipsometry. The IR properties of polyimide are shown in Fig. 46. When polyimide dispersion is added to the simulations a thick layer of polyimide produces significant absorptions that compete with metamaterial behavior. To

minimize this effect the bottom polyimide layer was reduced to 1 µm, which is a realistic minimum thickness for a polyimide layer.

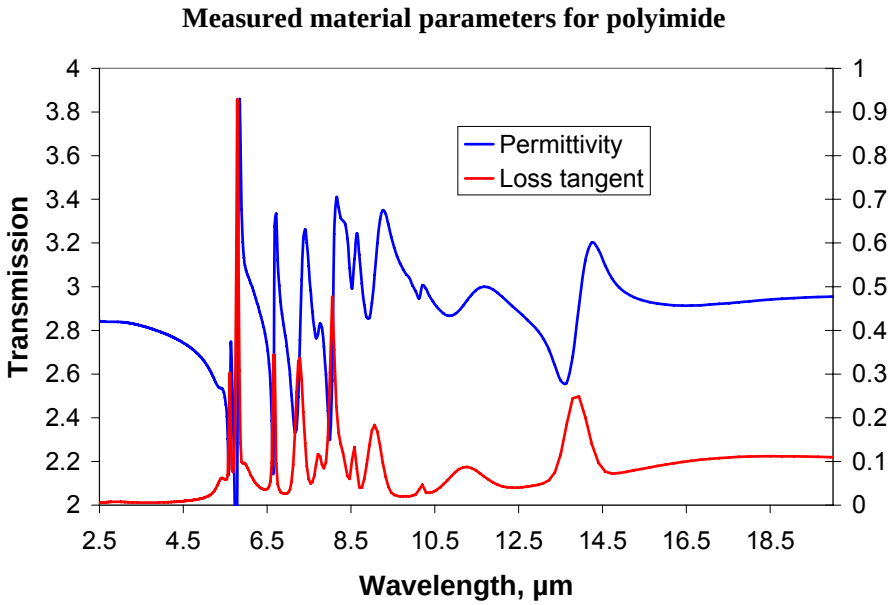

Figure 46: Measured Permittivity and loss tangent for polyimide.

In addition to the polyimide layers a liquid crystal requires electrical connections. Because of the need for optical transparency in standard applications, materials such as indium tin oxide (ITO) are typically used. ITO has an electronic mean free path comparable to a metal, but it has a much smaller carrier density. The result is that ITO acts like an insulator at wavelengths shorter than about 1 µm, but will look like a metal in the IR. Even a thin ITO layer significantly impedes the performance of an IR metamaterial because of the large reflection losses. An IR transparent conductor would require a very low carrier concentration and this would result in high ohmic loss that would likely impact the performance of the LC. The ITO layer in the simulation was treated as a 200 nm thick conducting layer with dynamic conductivity equal to 17.5 kS/m at the center wavelength of the FSS. The ITO dynamic conductivity value was derived

from the Drude model using standard sheet resistance (10 Ω/Sq) and plasma wavelength (1 μm) values [6.10].

Figure 47 shows the simulated performance of an FSS in a full LC cell. An FSS resonance may still be distinguished, but the transmission is now only changing from 10% to 30% from on resonance to off. There was also an increase in bandwidth from 2 μm to 3.7 μm from the lossless model to the full LC model in Fig. 47. This demonstrates that standard LC materials such as polyimide and ITO that are intended for performance in the visible are not well suited for IR applications.

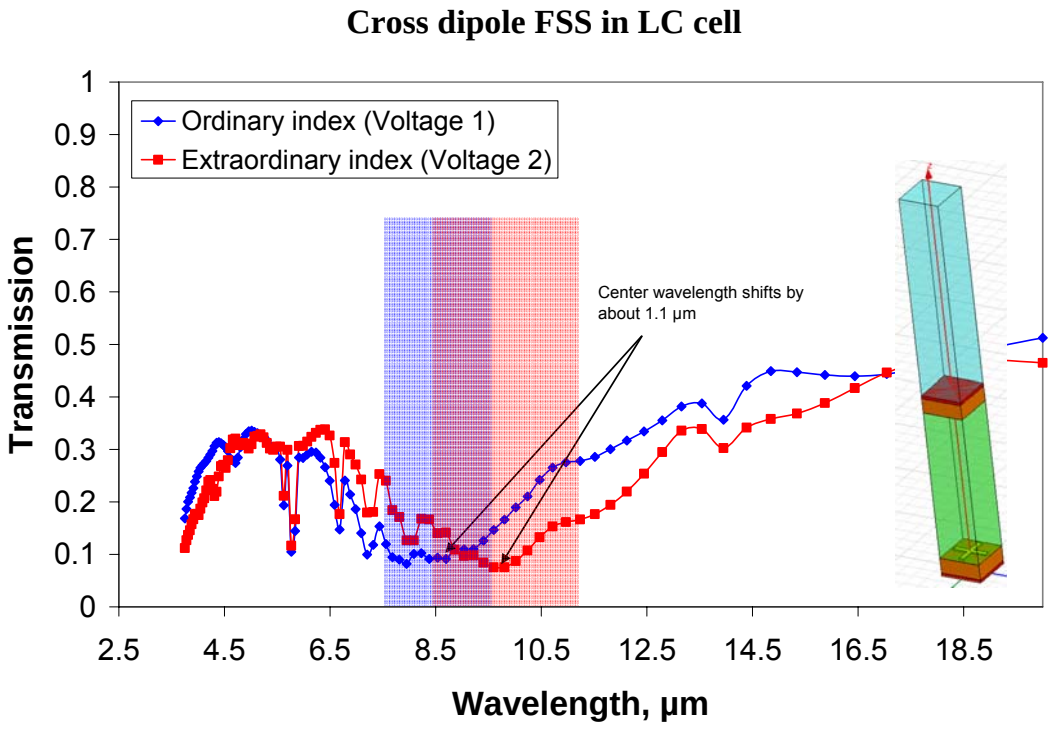

Figure 47: LC FSS simulations including polyimide rubbing layers with measured permittivity, loss, a realistic LC thickness, and ITO contact layers. The unit cell used in HFSS is shown on the right where the green layer is the LC, the orange layers are polyimide, the red layers are ITO, and the blue layer is the air box. The cross FSS element sits on the polyimide layer submerged in the LC as in Ref. 6.7.

Liquid crystal methods are not only better suited for the visible than the IR, but they are also more closely related to a traditional electro-optical device. That is, they employ a moderate change in refractive index over a distance that is comparable to the wavelength. Liquid crystals change the optical-path length of a superstrate or standoff layer. A tunable metamaterials needs a large and more local change in refractive index. It would not be effective for example to build liquid crystal metamaterial elements or hybrid unit cells – even if such a thing were possible. Thus we conclude that liquid crystals are not a feasible method for creating tunable IR metamaterials.

6.3 Photoconductive a-Si:H-N for Tunable Metamaterials

Thin film systems with IR conductivity or permittivity that may be actively tuned with the application of a DC electric field, have been of interest for some time to IR designers. Since the DC Schottky diode method was determined to be unfeasible alternative methods for producing an insulator to metal transition were investigated. One such alternative are photoconductive devices for active IR systems. The carrier concentration can be actively changed by illuminating a-Si:H with source energy above the band gap and thus out of the IR band. This illumination results in the generation of electron-hole pairs, and a sufficient density of these carriers will result in a change in the material's permittivity in the IR frequency range. Thus, by varying out-of-band pump power, an active IR system may be achieved.

Photoconductive elements have been used for optically generated grid arrays and as switches for reconfigurable antennas at 40 GHz [6.11]. In these low frequency designs high resistivity Si wafers have been used as the photoconducting elements. Due to the nanoscale size of IR systems patterned a-Si:H thin films must be used for photoconducting elements, and a higher carrier concentration is required for a contrast in permittivity. The generated electron-hole pairs form a pseudo-metallic plasma with behavior described by the Drude model. Eq. 6.2 gives the permittivity of the photoconductive semiconductor as the difference between the dark permittivity $\varepsilon_L(\omega)$ and a photo-plasma term

$$\varepsilon_r(\omega) = \varepsilon_L(\omega) - \frac{\omega_p{}^2}{\omega^2 - \frac{1}{\tau^2}} \times \left(1 + \frac{i}{\omega\tau}\right) \tag{6.2}$$

where ω_p is the plasma frequency, ω is the IR radiation frequency, and τ is the electronic relaxation time [6.12]. The plasma frequency depends upon the photo-carrier density in equation 6.3

$$\omega_p{}^2 = \frac{q^2}{\varepsilon_0} \times \frac{n_{ilum}}{m^*} \tag{6.3}$$

where q is the charge on the electron, ε_0 is the permittivity of free space, and m^* is the effective mass of the photo-carrier, and n_{ilum} is the photo-carrier density as a function of power from the thermal pump source. n_{ilum} should be greater than 10^{20} cm^{-3} for significant IR photoconductivity to occur. Although Eqs. 6.2 and 6.3 describe a pseudo-metallic plasma in a semiconductor, they are essentially the same principal as Eq. 2.1. Once again in order to force an insulator to metal transition in the IR we require a plasma frequency that is much greater than ω, and thus we require plasma frequency much greater than what has been used in photoconductive devices at lower frequencies such as Ref. 6.11.

The photo-carrier density, n_{ilum}, depends on the photon density, $G(P)$, and the recombination time, t, for electron hole hairs as shown in equation 6.4.

$$n_{ilum} = G(P) \times t \tag{6.4}$$

The recombination time t is the average time required for electron-hole pairs to recombine thus eliminating the photo-carrier. For intrinsic a-Si:H t is on the order of a

microsecond which means that for significant IR photoconductivity to occur *G(P)* needs to be on the order of 10^{26} $s^{-1}cm^{-3}$. By comparison a focused spot from a 100 W thermal source generates a *G(P)* on the order of 10^{23} $s^{-1}cm^{-3}$. Larger *G(P)* values may be obtained using a pulsed source such as a strobe light, but this would result in non-steady-state photoconductivity. In order to make IR photoconductivity accessible with a simple thermal source, a slow *t* is required on the order of a millisecond or longer.

Figure 48 shows density of state functions versus energy for intrinsic and *n* type a-Si:H.

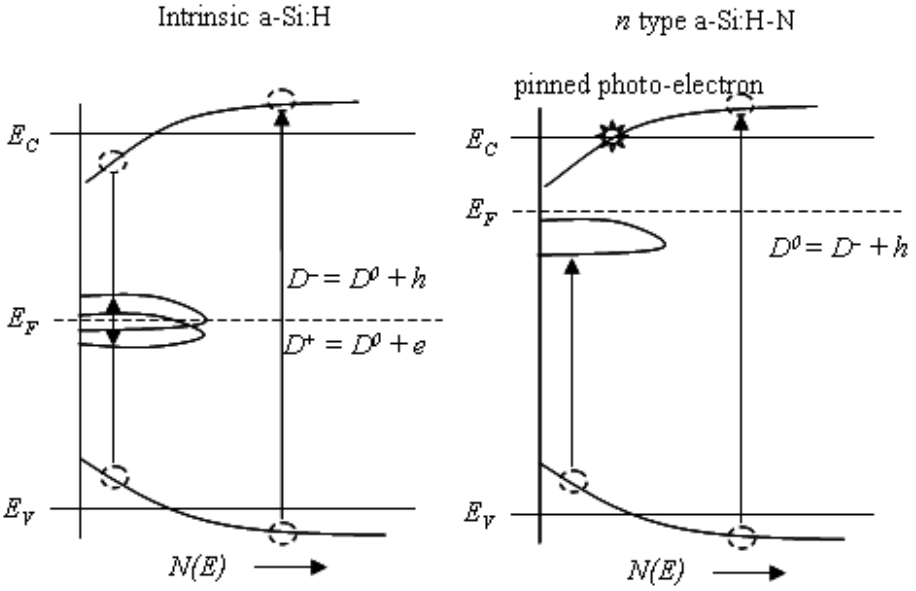

Figure 48: Density of states (N(E)) for a-Si:H.

In both cases E_C and E_V represent the energy of the mobility edge of the conduction and valence bands respectively while E_F is the Fermi energy. Near E_F in the forbidden gap of intrinsic *a*-Si:H are neutral dangling-bond states that may combine with electrons and holes to produce the charged dangling-bond defect reactions shown in the left half of Fig. 48. The production of charged dangling-bonds results in microsecond recombination times for intrinsic *a*-Si:H [6.13]. With the addition of *n* type donors in the right half of

Fig. 48 the Fermi energy increases, and this results in charged dangling bonds which quickly recombine with hole states. This results in a defect reaction that creates a neutralized dangling bond. An excess concentration of electrons is now present at the conduction level, and thus the photo-electrons may be said to be 'pinned' and left without hole states to recombine with. Doping with phosphorus has been observed to retard the recombination process in *a*-Si:H resulting in a high steady-state concentration of photo-carriers [6.14-6.15]. In order to pin electron-hole pairs the added impurity needs to be chosen such that the Fermi level of *a*-Si:H is increased. Nitrogen impurities can be expected to have a similar effect on the electronic structure as other group V elements, and longer recombination times have been observed than in the case of phosphorus doping. For nitrogen concentrations in the range of 10^{20} to 10^{21} cm^{-3} the recombination time was measured to slow to between 10 and 100 ms [6.16] – enough to produce steady-state IR photoconductivity from a thermal source. This *a*-Si:H alloy is referred to as *a*-Si:H-N.

Although the concentration of 'free' electrons in the conduction band may be large the electron mobility is very low in *a*-Si alloys. In states above the mobility edge, E_C, the electron mobility is on the order of 1 cm^2/Vs, but can drop several orders of magnitude in states that fall below the mobility edge as measured in Ref. 6.14 and 6.15. States lying below E_C are localized, and the electrons occupying such states are trapped by low mobility. Electrons that are initially excited into portions of the band above E_C are in non-equilibrium states. Thus it is likely that many of the photo-generated carriers will thermalize into equilibrium states below E_C via phonon interactions. There will be some

thermalization time associated with this event. Thus carrier generation, thermalization, and recombination are all competing processes that determine the steady-state optical properties of an *a*-Si alloy under illumination. This is investigated experimentally for *a*-Si:H-N.

Ion-assisted electron-beam evaporation was selected as the method for depositing *a*-Si:H-N thin films. Although evaporation is a less common method for *a*-Si:H deposition, it has been shown to successfully yield dense *a*-Si:H films suitable for photovoltaic devices [6.17]. Nitrogen is also added to the *a*-Si:H films via the evaporator's ion source. Partial pressures of H_2 at a 25 sccm flow rate and a 99 % Ar balanced N_2 at 1 sccm were pumped into the chamber and ionized by a tungsten filament. The resulting plasma was maintained at a steady discharge current of 0.5 A. Simultaneously to the plasma formation Si was evaporated onto the sample at a rate of 0.5 nm/s. The evaporator setup and processing conditions are shown schematically in Fig. 49.

The primary figure of merit for the *a*-Si:H-N films is the change in permittivity at IR wavelengths as measured by ellipsometry. In these experiments a J.A. Woollam Co. IR-VASE (variable angle spectroscopic ellipsometer) was used under standard *ex-situ* conditions. A test fixture shown in Fig. 50 was constructed to take ellipsometry data under illumination from a 12 V, 100 W quartz-halogen incandescent source. A high-pass filter is placed in front of the thermal source in the test fixture to block IR radiation so that the pump illumination is entirely out of band. The sample was constantly illuminated for 20 minutes during data collection.

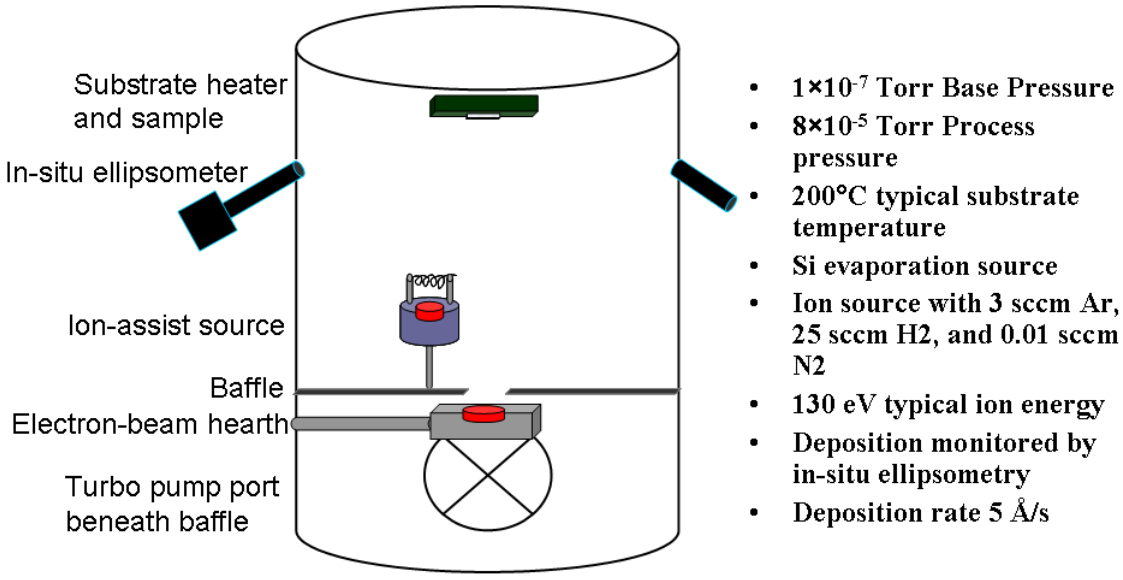

Figure 49: UHV evaporator schematic for a-Si:H-N deposition.

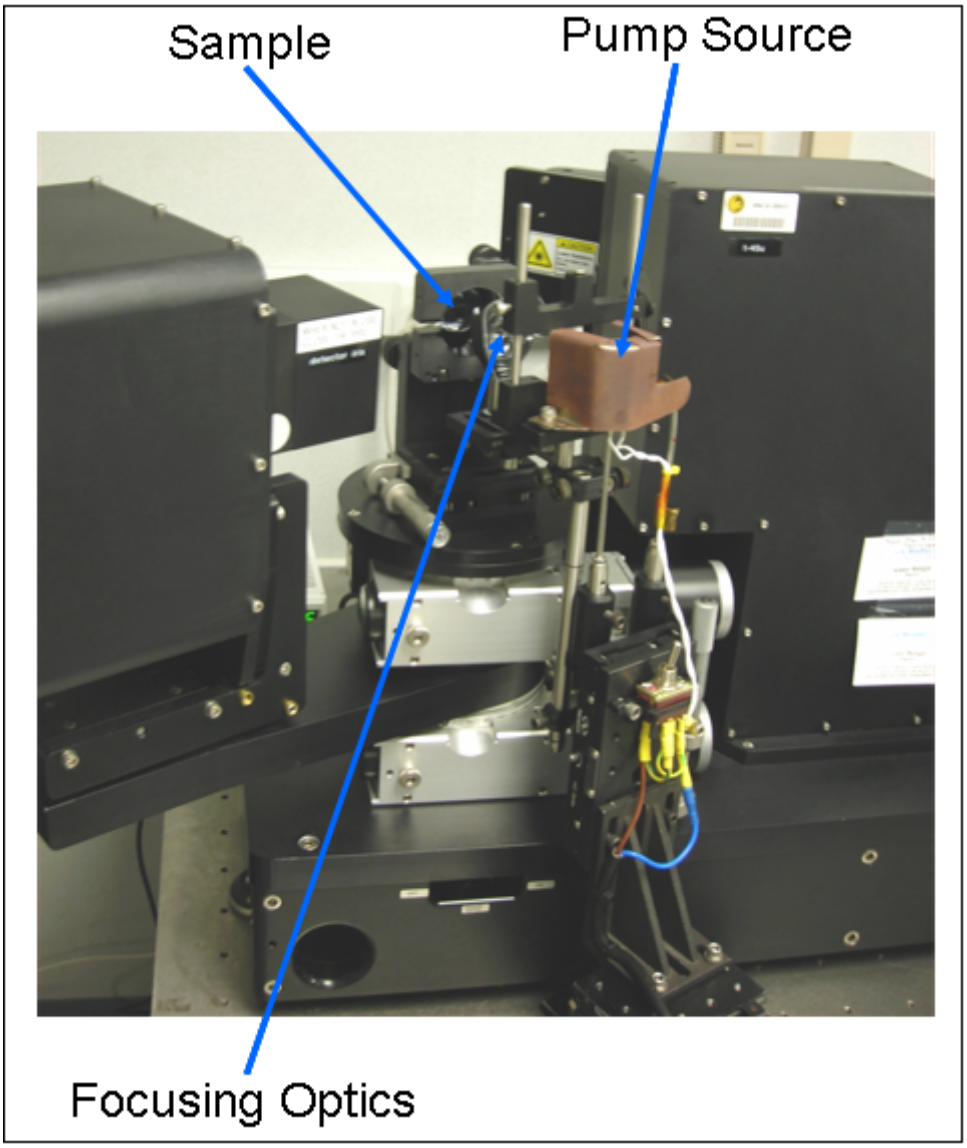

Figure 50: Ellipsometer setup for steady-state photoconductivity measurements.

The hydrogen concentration and Si-H bonding related microstructure may be evaluated using FTIR (fourier transform IR) spectroscopy. Nitrogen concentrations were measured directly using SIMS. The band gap energy, E_g, was measured using visible ellipsometry (J.A. Woollam Co. V-VASE), and E_g was found by fitting to a Tauc-Lorentz oscillator.

Measured results are shown in Table 7 for three films selected because of their large photoconductive response. For the deposition parameters used the hydrogen concentration was in the desired range at around 10 at. %, and the nitrogen concentration was sufficient to slow the recombination time to around 100 ms based on comparison to reference 6.16. The dark (n_{dark}) and illuminated carrier concentrations (n_{ilum}) were based on comparing the generation rate and recombination time following Eq. 6.4, and then to DC secondary photoconductivity measurements. Due to the presence of localized states as shown in figure 48, the mobility is not constant for all states since carriers may exist on either side of the mobility edge. Equations 6.2-6.3 were used to determine an effective steady-state mobility for IR frequency transport by comparing the change in permittivity under illumination from the IR ellipsometry measurement to n_{ilum}. It should not be assumed that the effective mobility for IR frequency transport is the same as the DC transport mobility. Even for metal films it has been shown that there is an effective mobility change at IR frequencies [6.18]. The effective IR mobility is about an order of magnitude smaller than the typical mobility for pure *a*-Si:H. Measurements of the DC carrier transport in references 6.19 and 6.16 were used to find n_{dark} and n_{ilum}. DC carrier transport properties of *a*-Si:H-N were found to be similar to reference 6.16, and from comparison to reference 6.19, it can be seen that the carrier concentration is much higher than in pure *a*-Si:H.

Table 7: Measured properties of a-Si:H-N with literature values for comparison. NH and NN are hydrogen and nitrogen concentrations, Eg is the band-gap energy, ndark and nilum are carrier concentrations under illumination, and μ* is the effective IR mobility.

Sample	N_H, at. %	N_N, at.%	Eg, eV	n_{dark}, cm^{-3}	n_{ilum}, cm^{-3}	μ^*, cm^2/V-s
hn02	20	2	1.6	5×10^{18}	2×10^{21}	0.76
hn03	6.6	1.2	1.4	4×10^{18}	5×10^{21}	0.56
hn12	28	2.8	1.62	2×10^{18}	2×10^{22}	0.18
a-Si:H [9]	10	0		2×10^{8}	2×10^{13}	
a-Si:H-N [6]	10	1.1		8×10^{18}	8×10^{21}	

Based on the high carrier concentrations and small effective mobility, Eq. 6.2 results in a nearly constant shift in permittivity. Due to the small mobility, the $1/\tau^2$ term is large compared to the frequency, so the change in permittivity is approximately equal to the squared product of the plasma frequency and relaxation time τ. Some spectral shifting of absorption features is also present as shown in Figs. 51-53. In figure 51 ellipsometry data of sample hn03 shows a change in permittivity of $\Delta\varepsilon_r = 1.3$ to 2 across much of the measured spectrum. This is due to increased loss from the photo-carriers which can be seen by comparing the imaginary permittivity functions. Sensitivity to some loss features such as the Si-H stretching mode at 630 cm^{-1} begin to be screened by photo-carriers and no longer appear in the spectrum. This screening effect also occurs in sample hn02 which has a similar change in permittivity as shown in figure 52.

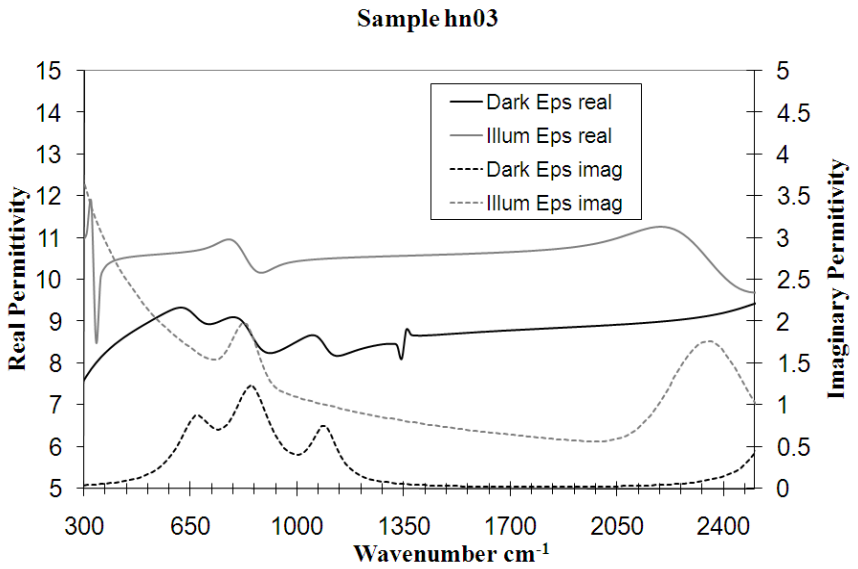

Figure 51: Real and imaginary portions of permittivity from ellipsometry measurements of sample hn03 in dark and illuminated state.

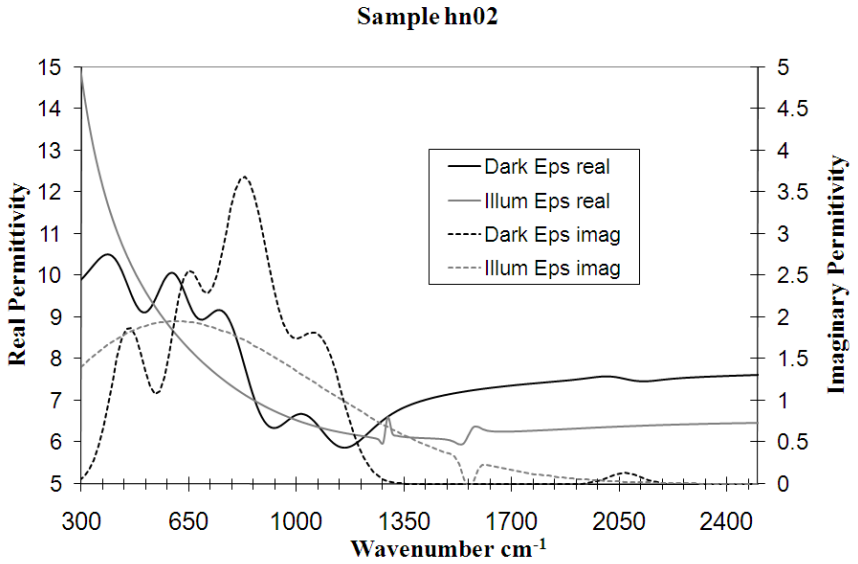

Figure 52: Real and imaginary portions of permittivity from ellipsometry measurements of sample hn02 in dark and illuminated state.

Sample hn02 has both higher nitrogen and hydrogen concentrations than hn03, and as a result it also has stronger absorption features. This leads to a more pronounced photo-carrier screening effect. The change in permittivity under illumination was similar away

from resonant features, and at frequencies greater than 1700 cm^{-1}, the $\Delta\varepsilon_r = 1.5$. The change in permittivity achieved in samples hn02 and hn03 are the highest achieved in these experiments. Figure 53 shows results from sample hn12 which are typical of most the films produced.

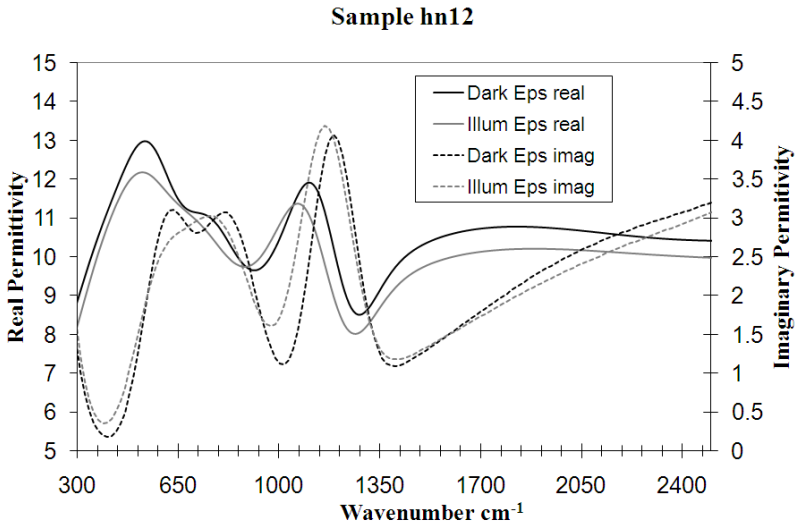

Figure 53: Real and imaginary portions of permittivity from ellipsometry measurements of sample hn12 in dark and illuminated state.

The IR effective mobility of sample hn12 is smaller than hn02 and hn03 which results in a smaller change in permittivity where $\Delta\varepsilon_r = 0.9$ away from resonance. IR frequency electron mobility is consistently the limiting factor in the permittivity change under illumination. Some photo-carrier screening is still present in sample hn12 as can be seen by the shifting of features in the imaginary part of permittivity, but the effect is smaller due to the limited mobility in hn12 compared to hn02.

Slowing the rate of electron-hole recombination in *a*-Si:H-N leads to high carrier concentrations suitable to create a change in permittivity under illumination at IR frequencies. This permittivity change is limited by the effective electron mobility at IR

frequencies and is approximately equal to the product of the plasma frequency and the relaxation time. The largest permittivity change was found to be $\Delta\varepsilon_r = 2$ and occurs over the spectral range from 650 to 2000 cm^{-1}.

Although it was possible to achieve a change in steady-state permittivity using the photoconductive method the quality and $\Delta\varepsilon_r$ of the *a*-Si:H-N films varied somewhat from sample to sample. This was largely due to inconsistent sample temperature during the various depositions. Although the sample temperature issue has since been resolved, the low-mobility problem still remains as a limitation on the performance of *a*-Si:H-N. It is possible to achieve a change in permittivity, but it is not large enough for the a-Si alloys to function as a photoconductive switch in a reconfigurable unit cell as was done in the RF band in Ref. 6.11. As a tunable metamaterial method we conclude that while photoconductivity may be feasible, it is not practical. Without a full insulator-to-metal transition the results would be limited and insufficient to justify the system level problems created by the pump source.

Following the experiments detailed in section 6.3, thermochromic materials were identified as an alternative to photoconductivity approaches. After initial investigations showed that a full insulator to metal transition could be achieved by heating and cooling VO_2, and that the permittivity change associated with this transition was orders of magnitude bigger than what could ever be achieved with *a*-Si:H-N, thermochromic metamaterials were aggressively pursued in place of continued photoconductive work. It

was these thermochromic experiments that would ultimately solve the tunable IR system problem.

6.4 Thermochromic Tunable Metamaterials

In a thermochromic material a reversible insulator-to-metal transition occurs upon heating or cooling through a set transition temperature T_C. Vanadium dioxide (VO_2) was first observed in Ref. 6.20 to undergo a transition from a semiconducting-to-metallic phase at T_C = 67°C. Such thermochromic behavior has been observed in other transition metal oxides such as MnO_3 [6.21], but VO_2 has produced the best results to date and may be integrated into metamaterials with a relatively low transition temperature. As with other tunable methods using diodes and photoconductivity, the mechanism of thermochromic tuning depends upon the creation of free electrons. However in this case instead of depleting electronic states, or generating carriers, in thermochromic materials such as VO_2 carriers are liberated by a symmetry-raising phase transformation. Figure 54 shows the crystal structure of VO_2 at $T < T_C$ and $T > T_C$. In the high temperature phase VO_2 has the rutile crystal structure characteristic of TiO_2 rich minerals and tetragonal symmetry. In the low temperature phase VO_2 has a distorted rutile structure with monoclinic symmetry. [6.22]

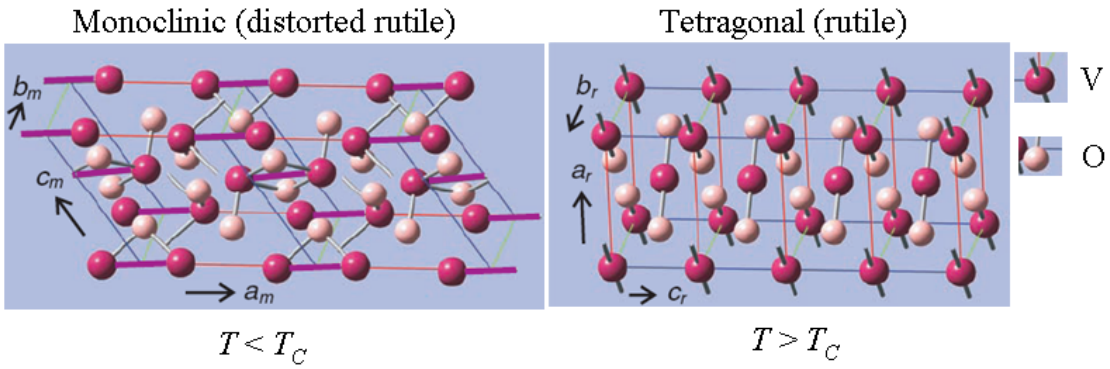

Figure 54: Crystal structure of VO2 relative to TC = 67°C. Diagrams taken in part from Ref. 6.22.

The metal-to-insulator transition in VO_2 is largely a result of the change in symmetry along the *c* axis in Fig. 54 [6.23]. At $T < T_C$ V-V bonds are in pairs with associated localized electron states. At $T > T_C$ the V-V bonds now have long-range order that results in delocalized electronic states. Thus electrons have been freed for transport resulting in metallic optical properties. This phase transformation is diffusionless and occurs on a picosecond time scale [6.24]. As Ref. 6.22 shows via ultrafast electron diffraction studies, the V atoms shift by small fractions of an angstrom during the reorientation from monoclinic to tetragonal symmetry. The V atoms do not shift along a single direction but rather it is a four-step process. A hysteretic response is therefore expected because the atoms move along one route during heating, but must then take this route in reverse order upon cooling. Due to the picosecond speed of the phase transformation illustrated by Ref. 6.22, the transition rate of a thermochromic-tunable metamaterial is effectively limited only by the rate at which the elements may be heated and cooled.

Figure 55 shows the measured optical constants at 20 and 70 °C for the VO_2 used in these experiments. The spectrum is shown in the visible and near IR in part A of Fig. 55, and part B shows the mid and thermal IR portions of the spectrum. In the visible there is little change in optical properties with temperature. This is consistent with Eq. 2.1 because the $T > T_C$ plasma frequency appears to be around 350 THz (850 nm) in Fig. 55 A, so the metallic phase should be transparent at wavelengths below 850 nm. In the near IR, and at important telecommunication wavelengths, the metallic phase plasma frequency is sufficient to produce a large contrast in refractive index in extinction coefficient. In the

mid IR the low temperature phase has a low extinction coefficient and minimal loss. The mid IR properties are ideal for transparent to opaque transitions. The thermal IR properties are similar, but the low temperature extinction coefficient is higher because of proximity to the V-O transverse-optical phonon mode. Based on Eq. 2.1 a permittivity change is expected to continue into the THz band as well. Table 8 compares the optical properties of VO_2 in both temperature states for key IR laser lines.

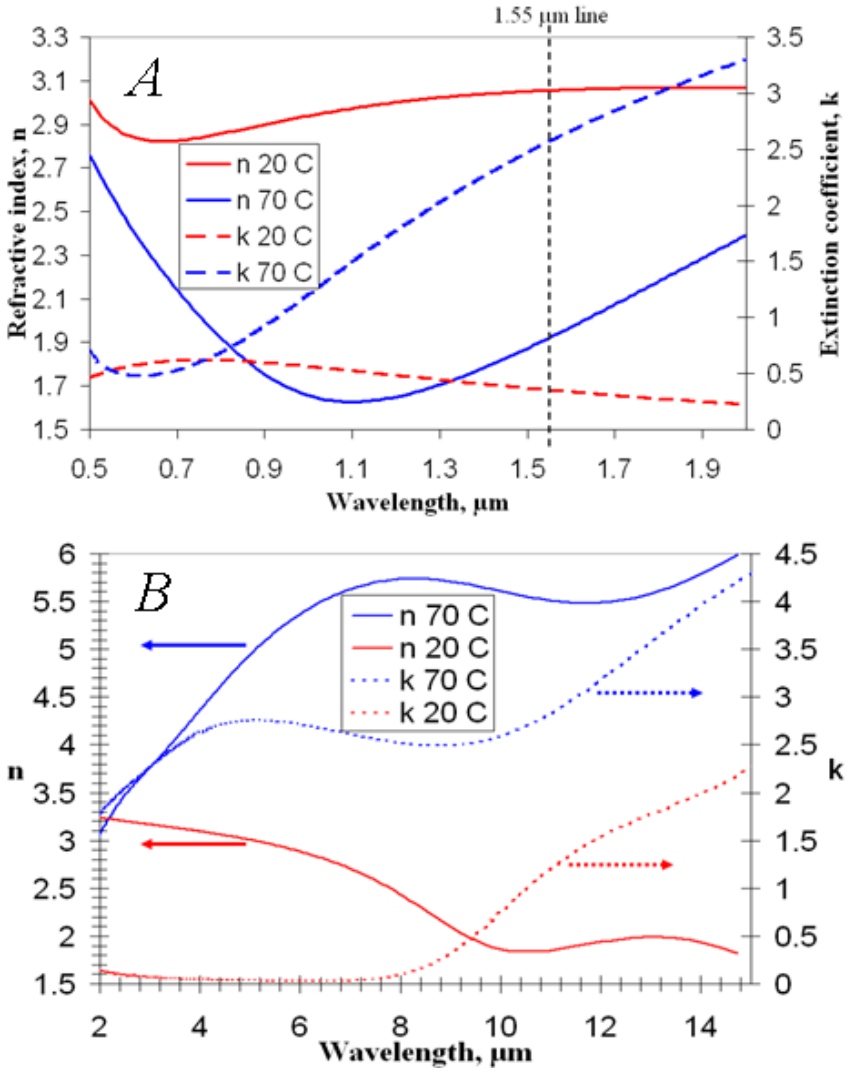

Figure 55: Measured optical properties for VO2, A: Visible and near IR, B: mid and thermal IR (index of refraction n, extinction coefficient k) for VO2 measured by ellipsometry.

Table 8: Optical properties of VO2 in high and low T phases for key IR laser lines.

λ, μm	n(20°C)	k(20°C)	n(70°C)	k(70°C)
1.55	3.05	0.35	1.92	2.57
3.39	3.14	0.06	3.99	2.43
10.6	1.84	1.04	5.54	2.72

Since the optical properties depend upon the liberation of free carriers by the symmetry transformation there should be a direct correspondence between n and k and electrical resistivity. A larger contrast in electrical resistivity will yield a larger optical contrast. The electrical hysteresis versus temperature and temperature range ΔT over which the phase transformation occurs will also transfer from the electrical to optical properties. Since more information is available on the electrical than optical properties, resistivity versus temperature is a good metric for evaluating the quality of VO_2 thin films.

VO_2 thin films may be fabricated by reactive electron-beam evaporation [6.25], reactive sputtering [6.26], pulsed-laser deposition [6.27], or thermal oxidation of metallic vanadium [6.28]. The VO_2 thin films used in these experiments were grown using a thermal oxidation process similar to Ref. 6.28. This method was selected because metallic V elements could be patterned and then oxidized to form VO_2 metamaterial elements. Figure 56 shows the electrical resistivity as a function of temperature during heating and cooling for the VO_2 films used in these experiments as well as films grown by pulsed-laser deposition in Ref. 6.27 for comparison. Compared to pulsed-laser

deposition, the thermal oxidation process has a lower T_C, less hysteresis, and a wider ΔT. The resistivity contrast between states is also smaller in the thermal oxidation method than the pulsed-laser deposition.

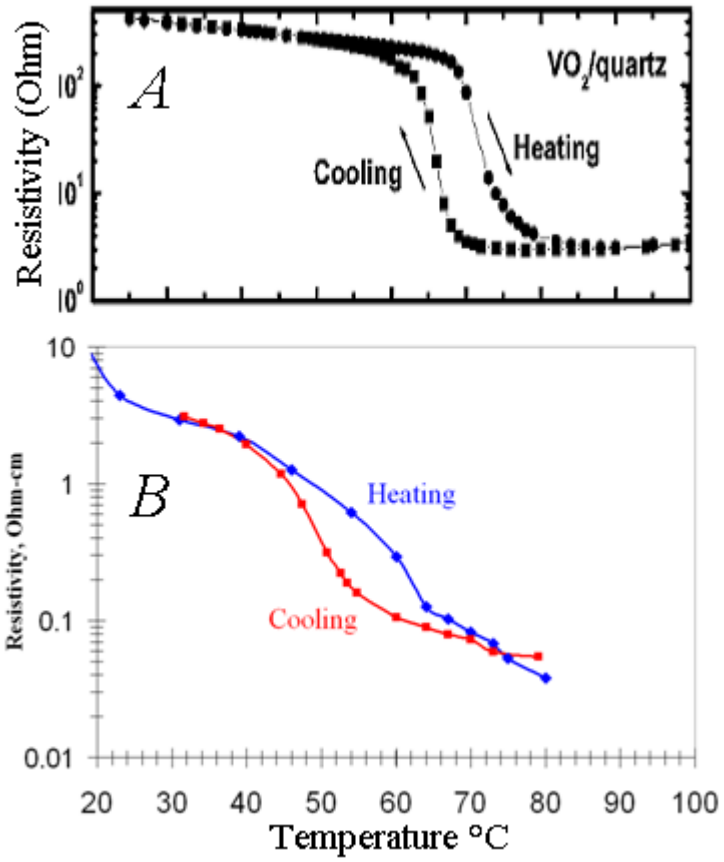

Figure 56: Electrical resistivity versus temperature for A) pulsed-laser deposition from Ref. 6.27, and B) thermally oxidized VO2 used in these experiments.

Depending upon the deposition or growth method and crystalline quality the contrast between states can vary significantly. For a VO_2 single crystal of good quality the contrast between high and low temperature states is on the order of 10^4 Ω-cm. In a single crystal the resistivity contrast is greatest along the *c* axis, and decreases by nearly an order of magnitude along direction perpendicular to the *c* axis. [6.29] Because of this anisotropy randomly oriented polycrystalline films can never match the contrast

obtainable in the single crystal variety. Because of the impact of grain boundaries and orientation dependent resistivity, the electrical contrast obtainable in high quality polycrystalline film is on the order of 10^3 Ω-cm. As shown in Fig. 56 part B, the resistivity contrast for the VO_2 films grown by thermal oxidation is on the order of 10^2 Ω-cm. It would be difficult to account for this smaller response compared to higher quality polycrystalline films on basis of factors such as small grains and defects alone, so the smaller contrast is likely a result of the VO_2 films being not entirely single phase. Since has V has at least half a dozen possible oxidation states it is possible for regions to exist in the crystal that are in a VO_x phase where x is less than 2. Future work may address this issue, and an order of magnitude improvement in the contrast between low and high temperature states should be possible.

Although it is possible to improve contrast, any difference in processing that improves contrast will likely also result in increased hysteresis, T_C and smaller ΔT. This is demonstrated in Fig. 56 by comparing the higher contrast pulsed-laser depositon VO_2 to the thermally grown VO_2. In addition experiments have shown that adding W impurities to single phase VO_2 lower T_C while also decreasing hysteresis, ΔT, and the contrast between states. [6.27] If a 10^2 Ω-cm contrast is sufficient to significantly change the optical properties, which Fig. 55 shows to be the case, then it makes sense to give up some contrast for less hysteresis in some cases. For example in beam steering applications smaller hysteresis and larger ΔT is desirable to change the reflected phase of a surface in an analog fashion rather than simply being able to switch between binary states. In some other applications having just two discrete states with a large contrast may

be preferred. It is useful then to consider Fig. 57 which plots properties of VO_2 versus various processing techniques and resulting structure features. Figure 57 is a composite of data from sources such as Ref. 6.24 to 6.29 and thermal oxidation experiments conducted by the author. A generally linear trend exists in the tradeoff between hysteresis and contrast.

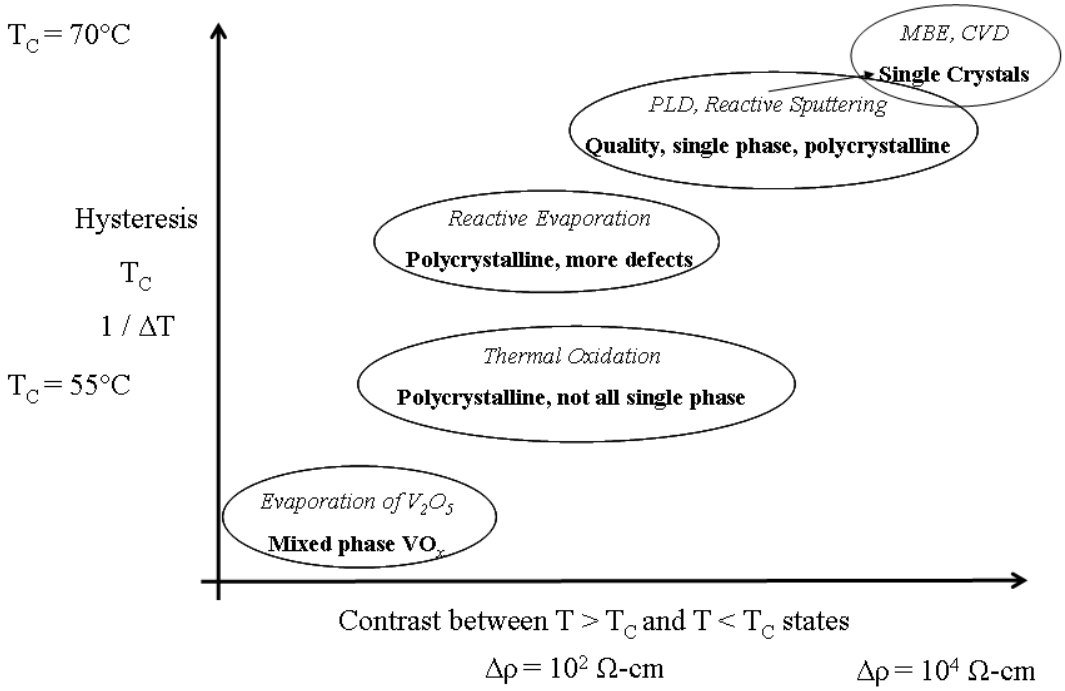

Figure 57: Hysteresis, TC, and ΔT vs. contrast for various processing methods and their resulting crystal structures and quality.

The $T > T_C$ phase of VO_2 does not have sufficient conductivity to serve as metamaterial elements in traditional split-ring resonator (SRR) designs, and thus the use of VO_2 in such designs will only result in a small shift in the resonance frequency. This can be seen in Ref. 6.30. The transition from a transparent to absorbing state that occurs in VO_2 may be best exploited in a metamaterial by coupling VO_2 elements to a resonating microcavity which is similar to an absorber frequency selective surface.

Tunable metamaterials using thermochromic thin films have recently been demonstrated in the THz band [6.31] and in the near IR [6.30]. Both articles use a layer of thermochromic VO_2 underneath the elements that broadens and removes the resonance as the temperature increases. In this section the ability to control reflected phase in a tunable metamaterial is demonstrated for the first time. The results also mark the first tunable metamaterial demonstrated in the thermal infrared band, and the largest resonance shift measured to date in the infrared. This was accomplished using a reflectarray metamaterial configuration [6.32] consisting of thermochromic VO_2 square-patch elements on an amorphous silicon (a-Si) microcavity as shown in Fig. 58. The reflection spectrum was measured by FTIR at 20 and 70 °C, and the reflected phase was measured at 10.6 μm by a Twyman-Green interferometer as a function of temperature. The reflectarray consisted of an array of square-patches 1.7 μm wide spaced at a 2.1 μm periodicity populating a 15 mm by 4 mm array.

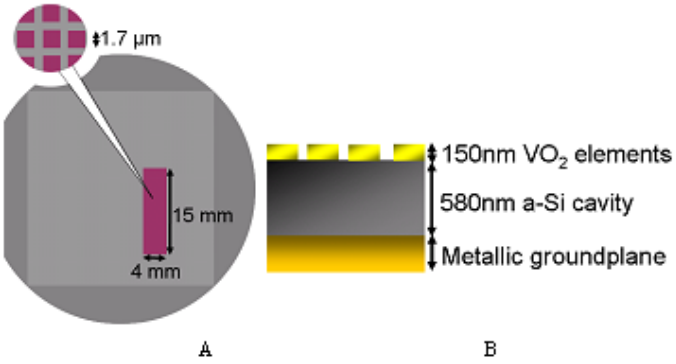

Figure 58: Reflectarray metmaterial diagram, A: patterned stripe with 1.7 μm square-patch VO2 elements, B: reflectarray cross section.

The reflectarray metamaterial from Fig. 58 was fabricated by depositing 100 nm of Cr on a Si wafer followed by the deposition of 580 nm of *a*-Si by electron-beam evaporation. V elements were fabricated on the *a*-Si cavity using electron-beam lithography. The VO_2

elements used in this article were made using a reactive-ion version of the thermal oxidation process in Ref. 6.28 to convert metallic V elements to VO_2. V square-patch elements were fabricated using standard electron-beam lithography methods as in previous chapters. Following liftoff processing the reflectarray was annealed to convert the V elements to VO_2. Results from the FTIR measurement compared to finite-element method (FEM) simulations are shown in Fig. 59. The simulations were done using Ansoft HFSS software which included the measured optical constants of VO_2 at 20 and 70 °C. The reflected phase spectrum calculated by HFSS is shown in Fig. 59 B. The resonating reflection minima shift from 9.2 μm to 11.6 μm covering a significant portion of the atmospheric transmission window in the thermal IR band. This is the first demonstration of a tunable metamaterial in the thermal IR and covers a larger portion of the spectrum than previous VO2 metamaterial results in the near IR [6.30]. Although the bandwidth of the resonance increases at 70°C due to the increased extinction coefficient, the reflectarray remains in a resonating state in both VO_2 phases. This may be seen by the reflection maxima that occur at 5 μm for both VO2 phases. Previous VO_2 metamaterial results in the THz band [6.31] which used a continuous layer of VO_2 had a transition from a resonating to a spectrally flat state in which the device does not appear to be in a resonating mode. Based on the HFSS simulations, the largest change in reflected phase occurs at the 20°C resonance at 9 μm where the reflected phase changes by more than 180 degrees. At 10.6 μm the reflected phase changes by 60 degrees in the HFSS simulation. This will be confirmed by the interferometer measurement.

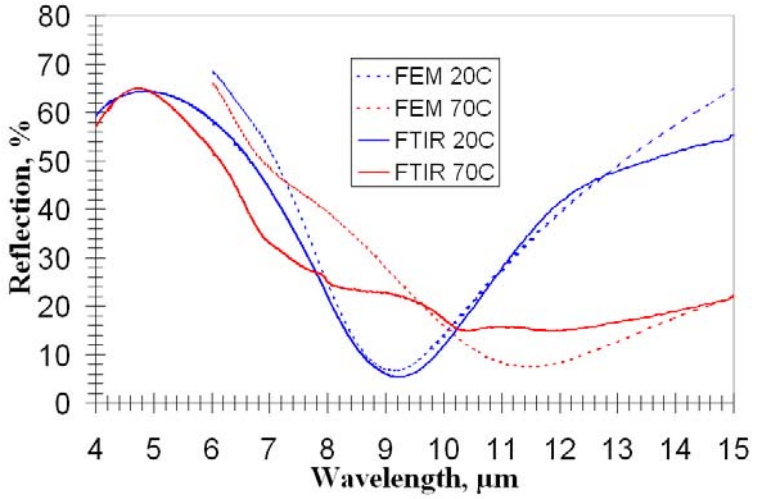

A

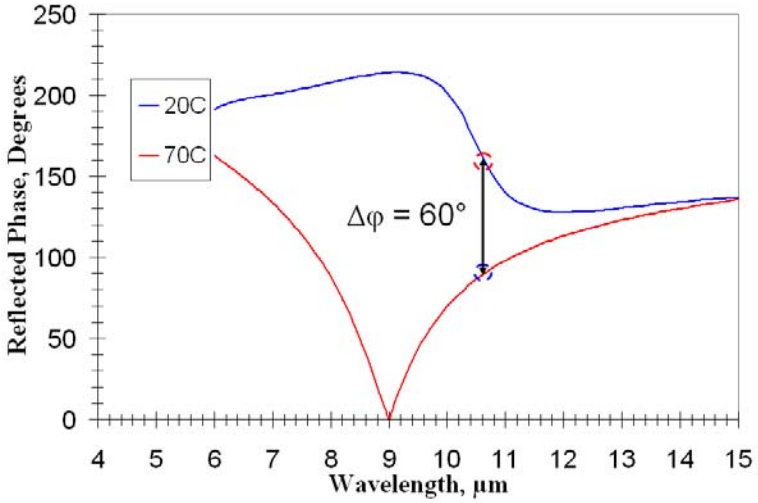

Figure 59: Reflected power and phase spectrum, A: Measured by FTIR compared to FEM simulation, B: Reflected phase spectrum simulated by FEM.

A schematic of the Twyman-green interferometer used to measure the reflected phase is shown in Fig. 60.

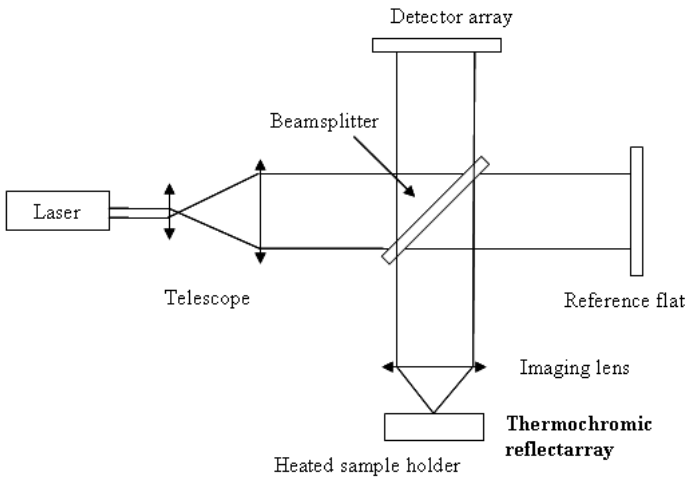

Figure 60: Twyman-Green interferometer using 10.6 μm CO2 laser used to measure reflected phase.

Interferograms are produced using a 10.6 μm CO_2 laser. The signal beam of the interferometer is incident on the thermochormic reflectarray sample that is oriented as shown in Fig. 58. A hot plate is used as the sample holder with a thermalcouple in contact with the wafer to measure the temperature. The detector array is a Spiricon camera used to take interferogram images. Figure 61 shows interferograms measured at 20°C and 70°C.

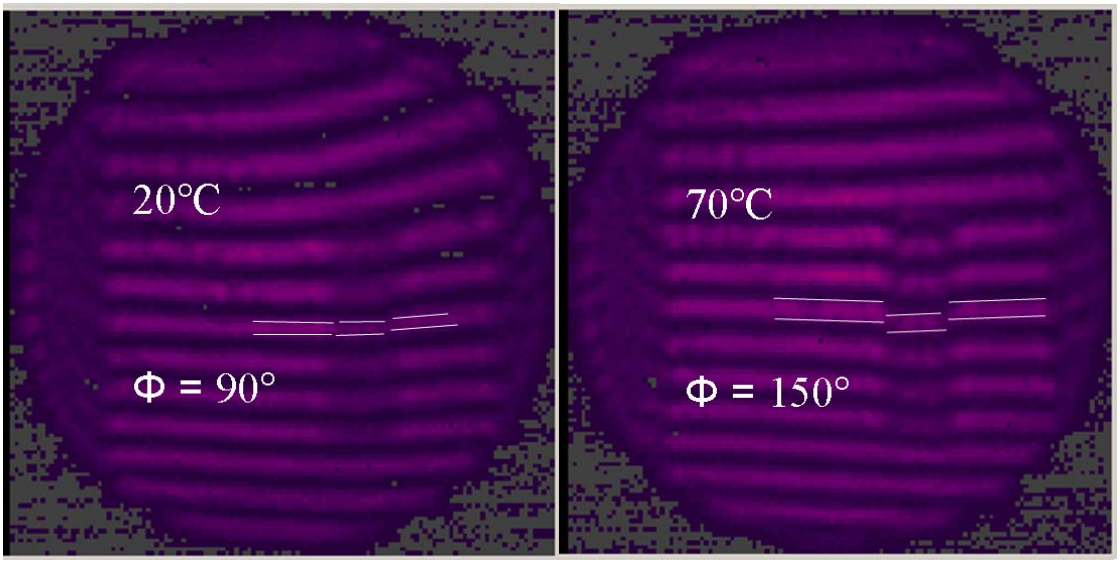

Figure 61: Interferograms of thermochromic reflectarray at 20°C and 70°C. White lines added to emphasize fringe contrast.

The step between successive fringes is equivalent to a 180 degree relative phase difference. The reflected phase of the reflectarray is measured by the size of the step in the fringes across the elements which is the region seen in Fig. 58. At 20°C, when the VO_2 elements are in the distorted-rutile phase, the reflected phase of the reflectarray is nearly equal to the a-Si cavity and thus there is only a small step in the fringes across the patterned region. At 70°C, after the transition to the rutile phase, the reflected phase has shifted 60 degrees as evidenced by the step in the fringes across the elements. This is in agreement with the FEM prediction. Thus the ellipsometry measurement of the optical constants, the FTIR measurement of the spectral reflectance, and the interferometric measurement of the reflected phase are all in agreement. Figure 62 shows the measured reflected phase as a function of temperature.

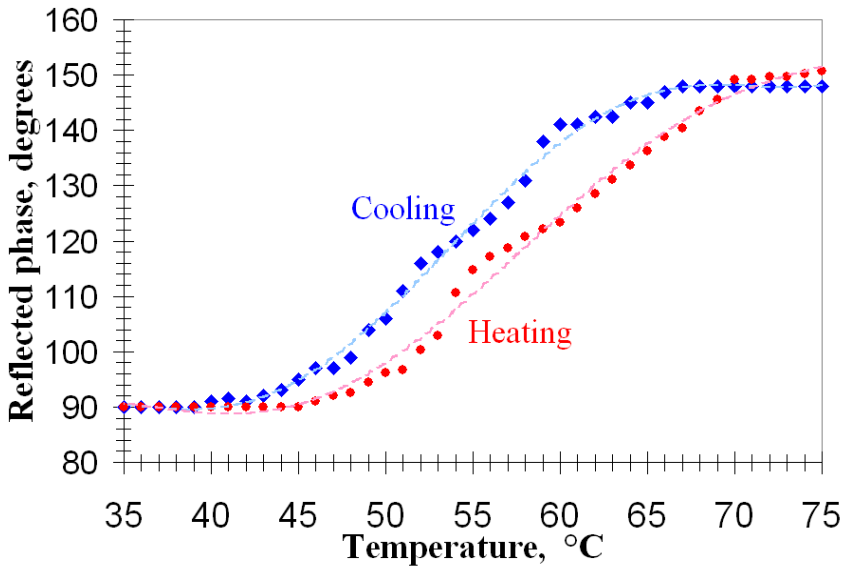

Figure 62: Measured reflected phase as a function of temperature during heating and cooling. Data points from interferogram analysis with polynomial fit indicated by the broken line.

The data in Fig. 62 was taken by analyzing the interferograms measured versus temperature while the sample was heated from 35 through 75 °C and then cooled through the same temperature range. From 65 though 45 °C, there is a linear decrease in the reflected phase corresponding to the exponential change in the resistivity of the VO_2 elements which is seen in Fig. 56 B. Following the hysteresis in the electrical resistivity upon heating and cooling, there is some hysteresis in the reflected phase.

The change in both reflected phase and resistivity in the VO_2 elements occurs between 45 and 65 °C for the films used in this article prepared by thermal oxidation. In pure single phase VO_2 deposited by pulsed laser deposition as in Ref. 6.27 the transition is more abrupt occurring between 65 and 75 °C. The hysteresis is also more significant in pure single phase VO_2 resulting in thermochromic transitions occurring over different temperature ranges for heating and cooling [6.27]. Lower transition temperature and wider thermal range with less hysteresis is seen in VO_2 doped with about 1 at.% W [6.24], or can be caused by characteristics of the microsctructure such as small grains [6.33] or surface roughness and voids [6.29]. The optimal microstructure of VO_2 for thermochromic metamaterials will be the subject of future work, but the current VO_2 elements result in a linear change in reflected phase that may be easily controlled over a 20°C range. This is useful for beam-steering applications as the phase may be scanned continuously instead of being limited to binary states. The reflected phase may also be changed quickly by resistive heating in a thin film beneath the groundplane as in Ref. 6.31 or by optical heating [6.34].

Using thermochromic VO_2 square-patch elements, the reflection minima was shown to be scanned spectrally from 9.2 to 11.6 μm by FTIR measurements. This was in agreement with finite-element HFSS simulations that used the optical constants of VO_2 measured by IR ellipsometry. The same HFSS simulation calculated a 60 degree phase change at 10.6 μm, and this was confirmed by interferometer measurements. Interferometric measurements also showed a linear change in phase that occurred as the sample temperature changed from 45 through 65 °C.

The demonstration of tunable reflected phase in a thermochromic metamaterial marks the successful completion of a five-year-long effort to produce a tunable metamaterial. Early attempts at a tunable device that used Schottky diodes, or some variation with p-n junctions, never had near the potential of that has been shown in the thermochromic devices. At the beginning of the project tuning the resonance frequency across the thermal IR (from 8 to 12 μm) was considered to be more than could reasonably be expected. Just half a micron of movement would have been considered a major achievement. However, in this chapter it was shown that the resonance frequency could be tuned from 9 to past 11 μm. In the next chapter it will be shown how VO_2 elements can be combined with metallic ones to form a hybrid unit cell. These thermochromic / metal hybrids have the potential to scan the resonant frequency across the thermal IR band and beyond – and they can do so while maintaining the Q factor of the resonance.

CHAPTER 7: CONCLUSIONS

7.1 Future Work

Topics of future work from this dissertation come from chapters 5 and 6. In chapter 5 analytical models were developed to determine the resonance frequency of an SRR element based on geometry, fringing-field effects, and plasmon-phonon coupling. A metamaterial resonance with Lorentzian lineshape is described by its resonant frequency, damping rate, and amplitude. The analytical models developed in chapter 5 address the resonance frequency and damping rate but not the amplitude or resonator strength. Future work should address this issue, and particularly the effect of resonator strength on plasmon-phonon coupling. Resonator strength may be related to the magnitude of the electric near fields, so in the case of an SRR element there should be greater sensitivity at the gap of the elements. For SEIS applications this could yield high spatial resolution since the appearance of coupled modes could be traced to molecules in close proximity to the SRR gap rather than just the element in general. It would be interesting to study the effects on plasmon-phonon coupling by: further varying element type and geometry to control the plasmon resonator strength, using dielectrics other than SiO_2 to vary the phonon resonator strength, and patterning the dielectric such that it was only in contact with portions of the element such as the gap in an SRR.

Another topic of future study related to resonator strength and near-field effects is multiple-layer IR metamaterials designed to have layer-to-layer coupling. Some multiple-layer metamaterials that have been fabricated with meanderline elements to act as IR

waveplates. The meanderline waveplates may be differentiated by layers that are spaced by a large enough distance to avoid layer-to-layer coupling. In this case registry between layers is not critical. In the case where the layer-to-layer spacing is less than the near-field penetration depth significant coupling will occur between the pair of elements. Two such coupled elements may be described as an artificial molecular dimer. [7.1] An example of some initial metamaterial dimers is shown in Fig. 63 where the top layer is in two different orientation states (symmetric and anti-symmetric modes) relative to the bottom layer. These test dimers were built just to prove the feasibility of the fabrication process, and to determine if simulations using FEM tools were accurate.

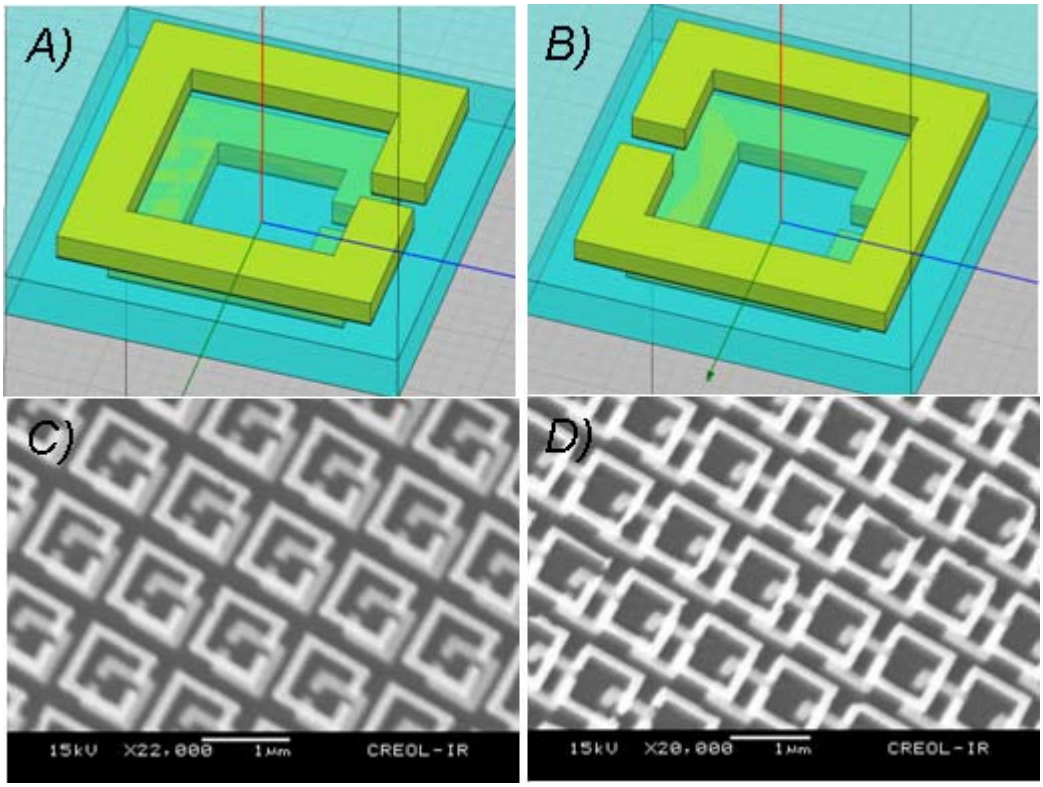

Figure 63: A) Symmetric metamaterial dimer design, B) anti-symmetric metamaterial dimer design, C) SEM micrograph of symmetric metamaterial dimer, D) SEM micrograph of anti-symmetric metamaterial dimer.

The bottom layer of elements were fabricated on Si and the top layer were fabricated on an experimental self-planarizing polyethylene film created by Sandia National Laboratories. The polyethylene film was only 140 nm thick, and the bottom layer of elements were 75 nm thick, so the layer-to-layer spacing was 65 nm. In chapter 5 the near-field penetration depth was estimated to be around 60 nm, so the polyethylene spacer layer was in the right range for a metamaterial dimer. A spacer layer that is still thinner would be preferred in future experiments. Polyethylene does not have any absorption bands in the thermal IR, but has a lower refractive index than Si. Thus the top layer of elements in Fig. 63 are larger than the bottom layer so that both would resonate at the same frequency. Due to misalignment in the initial experiment, which can be seen in Fig. 63, the metamaterials behaved like two independent resonators as opposed to a single dimer mode. Simulations and the initial experiment showed that layer-to-layer position registration was crucial for metamaterial dimers. FEM simulated electric near-field distributions are shown in Fig. 64 for a range of polyethylene (PE) thicknesses and good registration. It is only in the case of good registration and PE layer thickness at 100 nm (25 nm layer-to-layer spacing) that significant coupling is shown to occur between layers. This can be seen by the large magnitude field across the bottom interface of the top element for the 100 nm PE layer. For larger thickness the electric field is only concentrated at the SRR gap, which is the normal single-element mode. This result is in agreement with chapter 5 results that suggest coupling events occur within less than 60 nm of the elements.

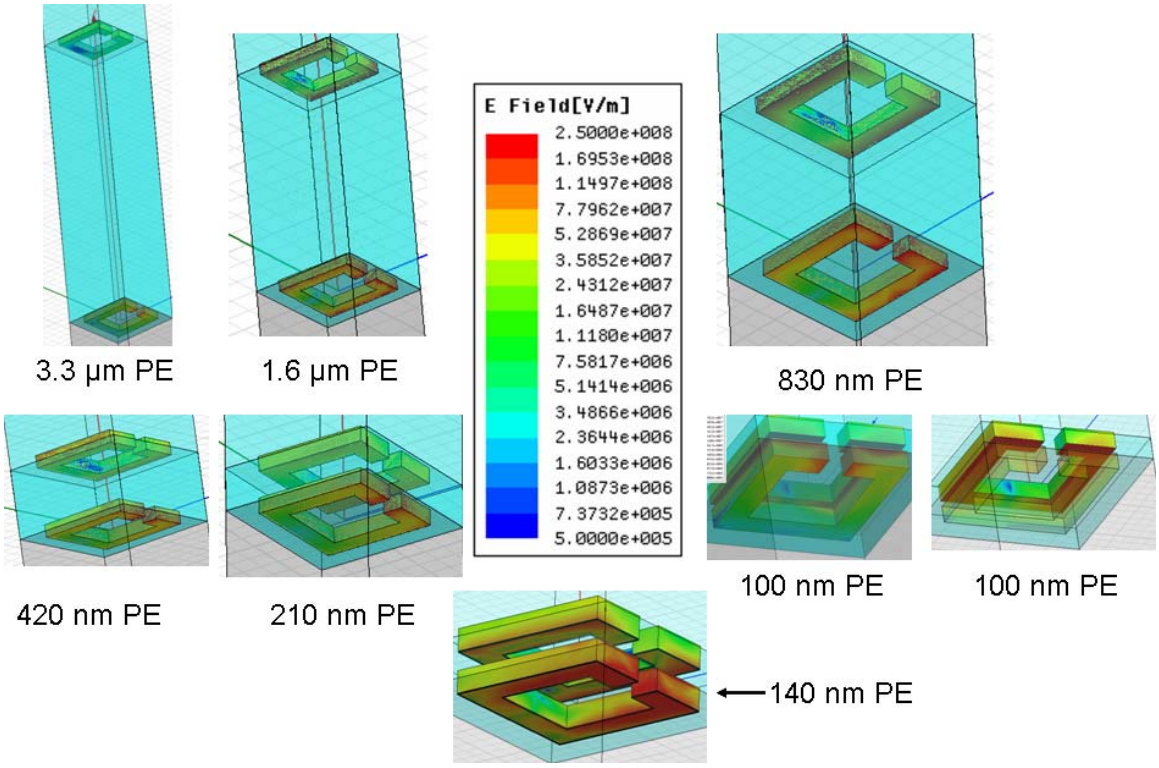

Figure 64: Electric near-field distributions for varying polyethylene (PE) spacer layer thickness in metamaterial dimers.

A great deal of future work may also be derived from chapter 6 utilizing VO_2 for tunable metamaterials. One important task will be to improve upon the resonance shift demonstrated in chapter 6 by creating hybrid unit cells. An example of a hybrid unit cell is shown in Fig. 65. Figure 65 A shows a Pt broken-ring resonator element. Next in Fig. 65 B V patches have been built across the gaps, and then these patches are thermally oxidized to form VO_2 patches as shown in Fig. 65 C. A process for aligning arrays was developed subsequent to the dimer experiment. Although the lithography in Fig. 65 was correct, the devices did not demonstrate tuning.

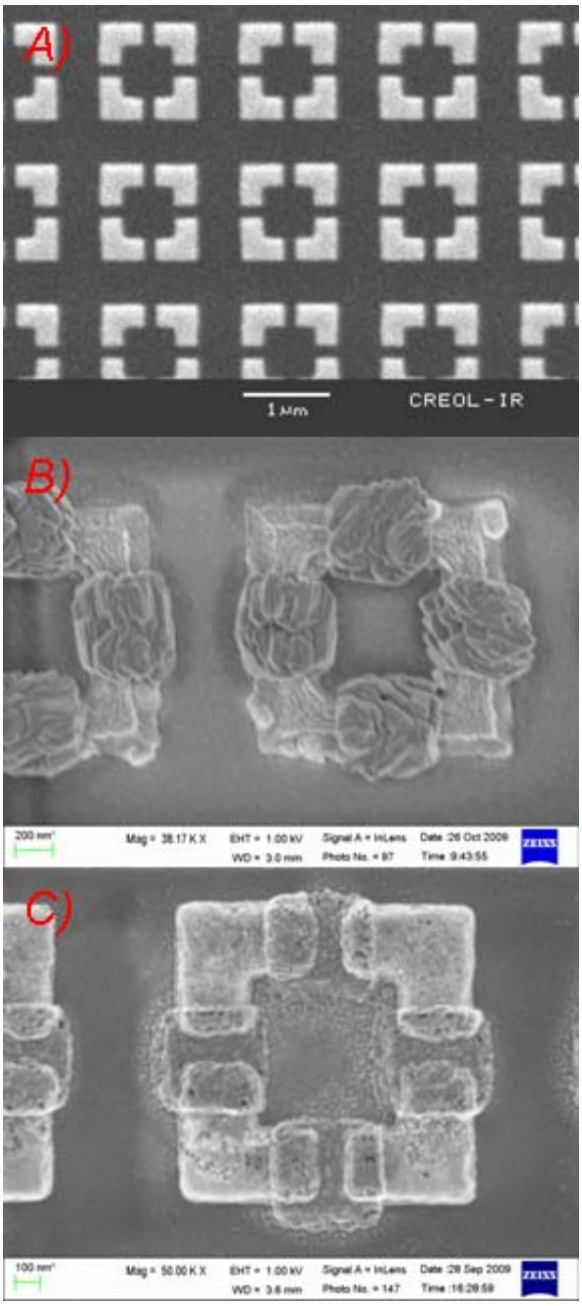

Figure 65: A) Pt broken-ring resonator elements, B) V patches aligned to gaps in Pt elements, C) V elements thermally oxidized to VOx

The lack of tuning indicates that the supposed VO_2 patches in Fig. 65 B were actually some other VO_x phase. When such problems occur a useful diagnostic tool is to compare the device's measured room temperature resonance frequency to the one predicted from simulation based on measured material properties. If the measured resonance frequency is

at a longer wavelength than predicted it is likely a mixed phase lower oxide (i.e. VO_x with $x < 2$ in some portions). In this case the problem may be corrected by simply repeating the thermal oxidation procedure for a longer time. If the measured resonance frequency is at a shorter wavelength than predicted it is likely a mixed phase higher oxide (i.e. VO_x with $x > 2$ in some portions). In continuous films a similar diagnostic is to measure the DC resistivity. As x in VO_x increases the resistivity increases by orders of magnitude. VO_2 has a room temperature resistivity at 10 Ω-cm as a reference point. The hybrid unit cell from the experiment shown in Fig. 65 was unfortunately in a higher oxide mixed phase, and thus there was no easy remedy. The cause of this problem stands as an issue for future work. Once fabrication process problems are solved, the predicted behavior of the hybrid unit cell is shown in Fig. 66 where a resonance in emissivity is scanned across the thermal IR while maintaining a similar bandwidth (hence similar Q factor).

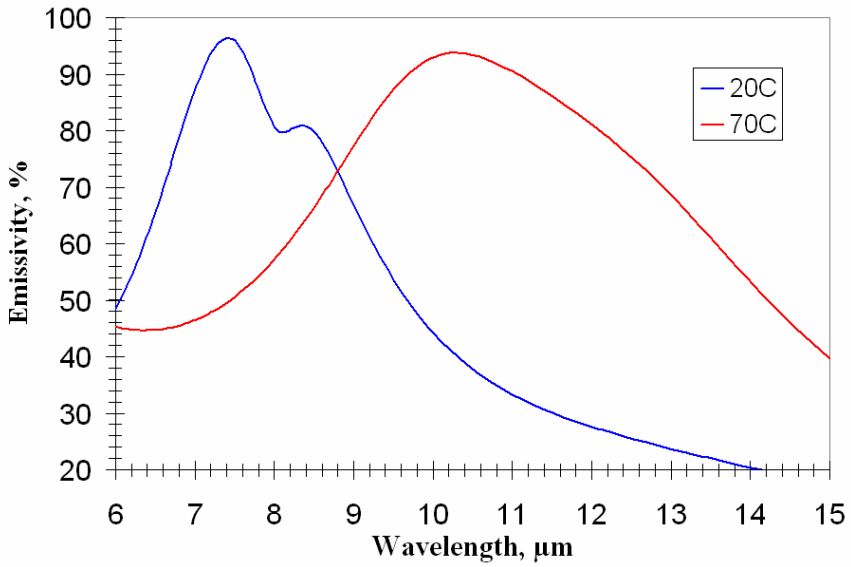

Figure 66: Simulated behavior of hybrid unit cell metamaterial from Fig. 65 assuming VO2 elements.

The goal of tunable metamaterial work was always to electronically control the resonant frequency. This may be achieved indirectly with thermochromic materials by electronically heating the VO_2 thin film or elements. However there are some cases where heating an IR system can be a problem. Thus an electrically induced insulator-to-metal transition is still desirable. Materials that are closely related to VO_2 by crystal structure and properties such as WO_3 have been shown to be capable of supporting electrochromism. Electrochromic materials undergo an insulator-to-metal transition under an applied bias potential. Although a phase transformation and symmetry change is associated with electrochromism [7.3] there is not the same sort of electron state delocalization that occurs in thermochromics. Instead the electrochromic is intercalated with cations (usually H^+ or Li^+) in a wet cell where the electrochromic thin film is immersed in an electrolyte solution as shown in Fig. 67 and a bias is applied. After the initial intercalation in a wet cell as shown in Fig 67 A, the electrochromic is transformed to a new crystal structure with some of the cation species always present. In the case of WO_3 the electrochromic becomes $Li_xW_{(1-x)}O_3$ where *x* may be changed as a function of bias potential in a solid-state-electrochomic stack as shown in Fig. 67 B. When *x* is large the electrochromic is in its colored state. In order to maintain charge neutrality in the colored state free electrons are pulled from the electrode. These free electrons lead to optical properties that follow Eq. 2.1 and an insulator-to-metal transition occurs. When *x* is small in the insulating state the electrochromic is said to be bleached.

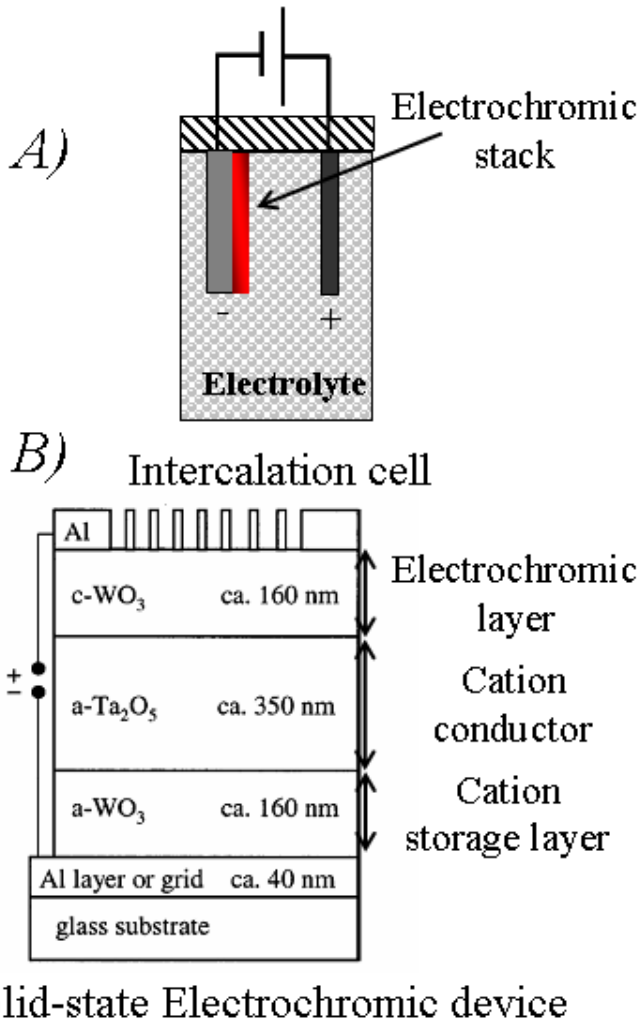

Figure 67: A) Intercalation wet cell, B) Solod-state electrochromic device from Ref. 7.2.

The transition between bleached and colored states is both reversible and fully electronically controlled. However, it is more difficult to implement than thermochromism. As shown in Fig. 67 B a three-film stack is required such that there is a crystalline electrochromic layer, a cation conductor, and an amorphous cation storage layer. [7.2] The cations intercalate into the electrochromic layer in the colored state and return to the storage layer in the bleached state. The cation conductor layer allows cations to be transmitted but not free electrons – in other words it is a good insulator. The change in optical constants between colored and bleached states in electrochromics is very

similar to the contrast between high and low temperature states in thermochromics. The colored and bleached optical properties of WO_3 have been measured using ellipsometry by J.A. Woollam in Ref. 7.4.

Since the cation concentration varies as a function of applied bias multiple states between two extremes are possible. The optical properties depend more upon the injection of free electronics as opposed to a phase transformation, so there is less of a hysteresis problem than occurs in thermochromics. However the stack of dielectric films shown in Fig. 67 B presents problems because the absorption bands in these films will interact with the metamaterial resonance. One obvious way to integrate elements with the electrochromic stack is to pattern slotted aperature elements into the top electrode. Such a device would resonate in the bleached state, but the resonance would be quenched in the colored state. A more interesting solution is shown in Fig. 68 where the electrochromic layer and the electrode have been merged into a single layer to form a hybrid metamaterial unit cell. As with theromochromic hybrids, such a device would be able to transition between two resonating states. Determining the feasibility of such hybrid electrochromic unit cells is an interesting topic for future work.

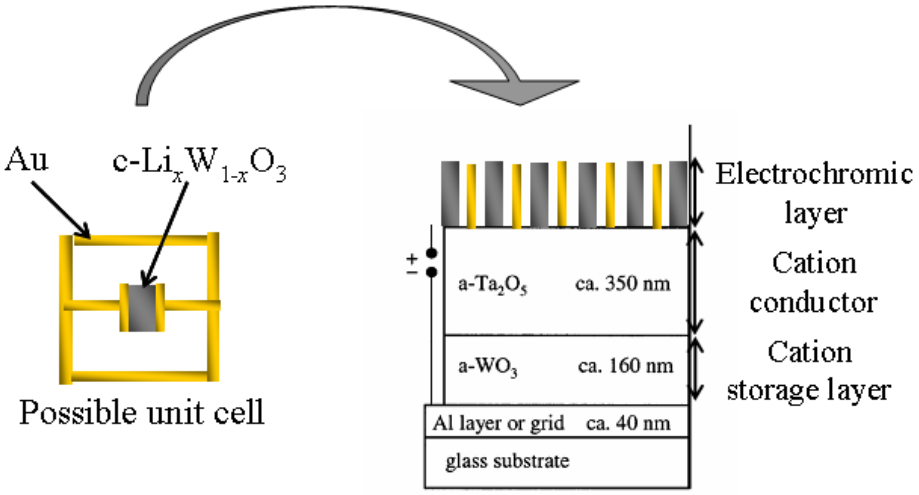

Figure 68: Electrochromic metamaterial.

7.2 Summary

The results from this dissertation can be used as the basis for many future experiments and metamaterial technologies. Tunable reflected phase was demonstrated for the first time in this dissertation, and the largest resonance-frequency-tuning range reported to date was also demonstrated. Interesting static metamaterial properties were also investigated including plasmon-phonon coupling which may be used for surface-enhanced infrared spectroscopy. Metamaterials were shown to be sensitive to surrounding dielectric layers as thin as 2 nm. Analytical models were constructed to predict the resonant frequency and damping rate of metamaterial extinction spectra. By showing agreement between the analytical, simulated, and measured results, some of the most accurate metamaterial experiments performed to date were shown. These experiments and new technologies all depend upon IR frequency carrier transport. Accordingly analytical models were constructed to predict the deviation from the Drude model due to the anomalous skin effect. These experiments mark significant progress in the physical understanding and utility of IR metamaterials.

LIST OF REFERENCES

[1.1] J.W. Goodman, *Statistical Optics* (Wiley, New York 1985) p. 169

[1.2] D.J. Shelton, T. Sun, J.C. Ginn, K.R. Coffey, G.D. Boreman, JAP 104, 103514 (2008)

[1.3] D.J. Shelton, J. Tharp, G. Zummo, W. Folks, G.D. Boreman, JVST B 25, 1827 (2007)

[1.4] D.J. Shelton, J. Cleary, J.C. Ginn, S. Wadsworth, R. Peale, D. Kotter, G.D. Boreman, Electronics Lett. 44, 1288 (2008)

[1.5] D.J. Shelton, D.W. Peters, M.B. Sinclair, I. Brener, L.K. Warne, L.I. Basilio, K.R. Coffey, G.D. Boreman, Optics Express 18, 1076 (2010)

[1.6] D.J. Shelton, I. Brener, J.C. Ginn, K.R. Coffey, G.D. Boreman, *Submitted to Phys. Rev. B* (February 2010)

[1.7] D.J. Shelton, J.C. Ginn, K.R. Coffey, G.D. Boreman, MRS Proceedings 1153, 1153-A02-02 (2009)

[1.8] D.J. Shelton, K.R. Coffey, G.D. Boreman, Optics Express 18, 1330 (2010)

[2.1] N.W. Ashcroft, N.D. Mermin, *Solid State Physics* (Thomson Learning, Inc., Toronto 1976) p.7

[2.2] M. Fox, *Optical Properties of Solids* (Oxford University Press, Oxford 2001) p. 145

[2.3] N.W. Ashcroft, N.D. Mermin, *Solid State Physics* (Thomson Learning, Inc., Toronto 1976) p.32-36

[2.4] M.P. Marder, *Condensed Matter Physics* (Wiley, New York 2000) p.137-147

[2.5] J. Kollar, Solid State Communications 27, 1313 (1978)

[2.6] P.T. Coleridge, *Phys. Rev. Lett.* **22,** 367 (1966)

[2.7] W.L. Barnes, A. Dereux, T.W. Ebbesen, Nature 424, 824 (2003)

[2.8] E. Kretschmann, H. Raether, Z. Naturforsch. A 23, 2135 (1968)

[2.9] A. Otto, Z. Phys. 216, 398 (1968)

[2.10] B. Hecht, H. Bielefeldt, L. Novotny, Y. Inouye, D.W. Pohl, Phys. Rev. Lett. 77, 1889 (1996)

[2.11] H. Ditlbacher, et. al., Appl. Phys. Lett. 80, 404 (2002)

[2.12] R.H. Ritchie, E.T. Arakawa, J.J. Cowan, R.N. Hamm, Phys. Rev. Lett. 80, 404 (2002)

[2.13] S.A. Maier, P.G. Kik, H.A. Atwater, S. Meltzer, E. Harel, B.E. Koel, A.G. Requicha, Nature Materials 2, 229 (2003)

[2.14] S.A. Darmanyan, A.V. Zayats, Phys. Rev. B 67, 035424 (2003)

[2.15] B. Liedberg, C. Nylander, I. Lunstrom, Sensors and Actuators 4, 299 (1983)

[2.16] T.R. Jensen, M.D. Malinsky, C.L. Haynes, R.P. Van Duyne, J. Phys. Chem. B 104, 10549 (2000)

[2.17] J.B. Pendry, L.M. Moreno, F.J. Garcia-Vidal, Science 305, 847 (2004)

[2.18] S.A. Maier, S.R. Andrews, L.M. Moreno, F.J. Garcia-Vidal, PRL 97, 176805 (2006)

[2.19] M.J. Lockyear, A.P. Hibbins, J.R. Sambles, PRL 102, 073901 (2009)

[2.20] B. Min, E. Ostby, V. Sorger, E.U. Avila, L. Yang, X. Zhang, K. Vahala, Nature 457, 455 (2009)

[2.21] V.G. Veselago, Phys. Uspekhi 10, 509 (1968)

[2.22] R.E. Ziolkowski, Phys. Rev. E 63, 046604 (2001)

[2.23] U.K. Chettiar, S. Xiao, A.V. Kildishev, W. Cai, H.K. Yuan, V.P. Drachev, V.M. Shalaev, MRS Bulletin 33, 921 (2008)

[2.24] J.B. Pendry, A.J. Holden, D.J. Robbins, W.J. Stewart, IEEE Tran. Microwave Theory Tech. 47, 2075 (1999)

[2.25] S. O'brian, D. McPeake, S.A. Ramakrishna, J.B. Pendry, Phys. Rev. B 69, 241101 (2004)

[2.26] D.R. Smith, W.J. Padilla, D.C. Vier, S.C. Nemat-Nasser, S. Schultz, PRL 84, 4184 (2000)

[2.27] R.A. Shelby, D.R. Smith, S. Schultz, Science 292, 77 (2001)

[2.28] J. Valentine, S. Zhang, T. Zentgraf, E. Ulin-Avila, D.A. Genov, G. Bartal, X. Zhang, Nature 455, 376 (2008)

[2.29] S. Zhang, W. Fan, N.C. Panoiu, K.J. Malloy, R.M. Osgood, S.R.J. Brueck, PRL 95, 137404 (2005)

[2.30] M. Fox, *Optical Properties of Solids* (Oxford University Press, Oxford 2001) p. 68

[2.31] D.R. Smith, S. Schultz, P. Markos, C.M. Soukoulis, Phys. Rev. B 65, 195104 (2002)

[2.32] D. Schurig, J.J. Mock, B.J. Justice, S.A. Cummer, J.B. Pendry, A.F. Starr, D.R. Smith, Science 314, 977 (2006)

[2.33] T. Driscoll, H.T. Kim, B.G. Chae, B.J. Kim, Y.W. Lee, N. Marie Jokerst, S. Palit, D.R. Smith, M. Di Ventra, D.N. Basov, Science 325, 1518 (2009)

[2.34] B. Kante, A. de Lustrac, J.M. Lourtioz, Phys. Rev. B 80, 035108 (2009)

[2.35] D.H. Kwon, X. Wang, Z. Bayraktar, B. Weiner, D.H. Werner, Opt. Lett. 33, 545 (2008)

[2.36] N.I. Landy, S. Sajuyigbe, J.J. Mock, D.R. Smith, W.J. Padilla, PRL 100, 207402 (2008)

[2.37] W. J. Padilla, A.J. Taylor, C. Highstrete, M. Lee, R.D. Averitt, PRL 96, 107401 (2006)

[2.38] J.F. O'Hara, E. Smirnova, H.T. Chen, A.J. Taylor, R.D. Averitt, C. Highstrete, M. Lee, W.J. Padilla, J. Nanoelectron. Optoelectron. 2, 90, (2007)

[2.39] J. Ginn, B. Lail, J. Alda, G. Boreman, Opt. Lett. 33, 779 (2008)

[2.40] J.C. Ginn, D.J. Shelton, P. Krenz, B. Lail, G.D. Boreman, Submitted to Optics Express, (2009)

[2.41] J. Tharp, J. Alda, G.D. Boreman, Optics Letters 32**,** 2852 (2007)

[2.42] E. Cubukcu, S. Zhang, Y.S. Park, G. Bartal, X. Zhang, J. Appl. Phys. 95, 043113 (2009)

[3.1] G. Fahsold, A. Bartel, O. Krauth, N. Magg, A. Pucci, Phys. Rev. B 61, 14108 (2000)

[3.2] G. Fahsold, M. Sinther, A. Priebe, S. Diez, A. Pucci, Phys. Rev. B 70, 115406 (2004)

[3.3] R. Lenk, A. Knabchen, J. Phys. Condens. Matter 5, 6563 (1993)

[3.4] J.M. Ziman, *Principles of the Theory of Solids 2nd Ed.* (Cambridge University Press, Cambridge 1972) p. 282

[3.5] A.B. Pippard, Proc. Royal Soc. A 224, 273 (1954)

[3.6] E.H. Sondheimer, Advances in Physics 50, 499 (2001) [republished]

[3.7] A.B. Pippard, Proc. Royal Soc. A 250, 325 (1957)

[3.8] R.G. Chambers, Proc. Royal Soc. A 215, 481 (1952)

[3.9] H.E. Bennett, J.M. Bennett, E.J. Ashley, R.J. Motyka, Phys. Rev. 165, 755 (1968)

[3.10] S.R. Nagel, S.E. Schnatterly, Phys. Rev. B 9, 1299 (1974)

[3.11] G.R. Parkins, W.E. Lawrence, R.W. Christy, Phys. Rev. B 23, 6408 (1981)

[3.12] F. Forstmann, R.R. Gerhardts, *Metal Optics Near the Plasma Frequency* (Springer-Verlag, Berlin 1986)

[3.13] P. Zhou, S.Y. Wang, J. Li, R.J. Zhang, H.Y. You, Z.C. Shen, L.Y. Chen, Thin Solid Films 455, 157 (2004)

[3.14] J.C. Ginn, B. Lail, D.J. Shelton, J.S. Tharp, W.R. Folks, G.D. Boreman: ACES J 22, 184 (2007)

[3.15] P.B. Johnson, R.W. Christy, Phys. Rev. B 6, 4370 (1972)

[3.16] T. Sun, B.Yao, A.P. Warren, V.Kumar, S. Roberts, K. Barmak, K.R. Coffey, J. Vac. Sci. Technol. A 26, 605 (2008)

[4.1] B. Monacelli, J. Pryor, B.A. Munk, D. Kotter, G.D. Boreman, IEEE Trans. Ant. Prop. 53, 745 (2005)

[4.2] A. Mahmood, D.P. Butler, Z. Celik-Butler, *Sensors, 2005 IEEE*, 4pp. 30 Oct. – 3 Nov. 2005

[4.3] R.P. Drupp, J.A. Bossard, D.H. Werner, T.S. Mayer, *Antennas and Propagation Society International Symposium, 2004. IEEE,* vol. 2, pp. 1907-1910, 20-25 June 2004

[4.4] S. Young, D. Weston, B. Dauksher, D. Mancini, S. Pacheco, P. Zurcher, M. Miller, J. Micromechanics and Microengineering 15, 1824 (2005)

[4.5] P. Bebin, R. Prud'homme, J. Polymer Sci. B: Polymer Phys. 40, 82 (2002)

[4.6] J. Ginn, B. Lail, D. Shelton, J. Tharp, W. Folks, and G. Boreman, Appl. Comp. Electromag. Soc. J. 22,184 (2006)

[4.7] N. Chen, J. Engel, S. Pandya, c. Liu, *MEMS 2006 Conference, Istanbul Turkey*, Jan. 22-26, 2006

[4.8] D.W. Porterfield, J.L. Hesler, R. Densing, E.R. Mueller, T.W. Crowe, R.M. Weikle II, Applied Optics 33, 6046 (1994)

[4.9] H.T. Chen, J.F. O'Hara, A.K. Azad, A.J. Taylor, R.D. Averitt, D.B. Shrekenhamer, W.J. Padilla, Nature Photonics 2, 295 (2008)

[4.10] B.A. Munk, "Frequency Selective Surfaces," (John Wiley & Sons, New York, 2000) p. 28

[4.11] W. Folks, J. Ginn, D. Shelton, J. Tharp, and G. Boreman, Physica Status Solidi 5, 1113 (2008)

[4.12] D. Shelton, J. Tharp, G. Zummo, W. Folks, and G. Boreman , JVST B 25, 1827 (2007)

[5.1] B. Kante, A. de Lustrac, J.M. Lourtioz, F. Gadot, Optics Express 16, 6774 (2008)

[5.2] W. J. Padilla, A.J. Taylor, C. Highstrete, M. Lee, R.D. Averitt, Phys. Rev. Lett. 96, 107401 (2006)

[5.3] D. Li, Y.J. Xie, P. Wang, R. Yang, J. of Electromagn. Waves and Appl. 21, 1551 (2007)

[5.4] H. Leplan, B. Geenen, J.Y. Robic, Y. Pauleau, J. Appl. Phys. 78, 962 (1995)

[5.5] N.M. Sushkova, A.G. Akimov, Vacuum 56, 287 (2000)

[5.6] D.J. Shelton, T. Sun, J.C. Ginn, K.R. Coffey, G.D. Boreman, J. Appl. Phys. 104, 103514 (2008)

[5.7] M. G. Moharam, T. K. Gaylord, J. Opt. Soc. Am. 71, 811 (1981)

[5.8] J.B. Pendry, L.M. Moreno, F.J. Garcia-Vidal, Science 305, 847 (2004).

[5.9] S.A. Maier, S.R. Andrews, L.M. Moreno, F.J. Garcia-Vidal, PRL 97, 176805 (2006).

[5.10] M.J. Lockyear, A.P. Hibbins, J.R. Sambles, PRL 102, 073901 (2009).

[5.11] B. Min, E. Ostby, V. Sorger, E.U. Avila, L. Yang, X. Zhang, K. Vahala, Nature 457, 455 (2009).

[5.12] X. Zhang, D. Wu, C. Sun, X. Zhang, Phys. Rev. B 76, 085318 (2007).

[5.13] K. Lopata, D. Neuhauser, R. Baer, J. Chem. Phys. 127, 154714 (2007).

[5.14] S. Noda, M. Fujita, T. Asano, Nature Photonics 1, 449 (2007).

[5.15] T.J. Thompson, G. Rempe, H.J. Kimble, PRL 68, 1132 (1992).

[5.16] C. Weisbuch, M. Nishioka, A. Ishikawa, Y. Arakawa, PRL 69, 3314 (1992).

[5.17] F. Neubrech, A. Pucci, T. Cornelius, S. Karim, A. Garcia-Etxarri, J. Aizpurua, PRL 101, 157403 (2008)

[5.18] F. Neubrech, D. Weber, D. Enders, T. Nagao, A. Pucci, J. Phys. Chem. C (to be published).

[5.19] J.C. Ginn, D.J. Shelton, P. Krenz, B. Lail, G.D. Boreman, J. Appl. Phys. **105**, 074304, (2009).

[5.20] A.V. Kavokin, J.J. Baumberg, G. Malpuech, F.P. Laussy, *Microcavities* (Oxford University Press, Oxford 2007), p. 151.

[5.21] K.L. Kliewer, R. Fuchs, Phys. Rev. **144**, 495 (1966).

[5.22] R. Fuchs, K.L. Kliewer, Phys. Rev. **150**, 574 (1966).

[5.23] D.J. Shelton, T. Sun, J.C. Ginn, K.R. Coffey, G.D. Boreman, J. Appl. Phys. 104, 103514 (2008).

[5.24] T. Driscoll, H.T. Kim, B.G. Chae, B.J. Kim, Y.W. Lee, N. Marie Jokerst, S. Palit, D.R. Smith, M. Di Ventra, D.N. Basov, Science 325, 1518 (2009).

[5.25] M.J. Dicken, K. Aydin, I.M. Pryce, L.A. Sweatlock, E.M. Boyd, S. Walavalkar, J. Ma, H.A. Atwater, Optics Express 17, 18330 (2009).

[5.26] D.J. Shelton, K.R. Coffey, G.D. Boreman, Optics Express 18, 1330 (2010).

[6.1] C. Mias, Electronic Letters 39, 850 (2003).

[6.2] A. Tennant, B. Chambers, IEEE Microwave and Wireless Components Letters 14, 46 (2004).

[6.3] Y.H. Ye, D.Y. Jeong, Q.M. Zhang, Appl. Phys. Lett. 85, 654 (2004).

[6.4] H.T. Chen, W.J. Padilla, J.M.O. Zide, A.C. Gossard, A.J. Taylor, R.D. Averitt, Nature 444, 597 (2006).

[6.5] J. Ginn, B. Lail, D. Shelton, J. Tharp, W. Folks, and G. Boreman, ACES Journal 22, 184 (2007).

[6.6] S.M. Sze, *Physics of Semiconductor Devices 2nd edn*, (Wiley-Interscience Publication, New York 1981) p. 246-250

[6.7] Bossard, J.A.; Xiaotao Liang; Ling Li; Seokho Yun; Werner, D.H.; Weiner, B.; Mayer, T.S.; Cristman, P.F.; Diaz, A.; Khoo, I.C., IEEE Trans. Antennas and Propagation 56, 1308 (2008).

[6.8] S. Gauza, C. H. Wen, **S. T. Wu**, R. Dabrowski, C. S. Hsu, C. O. Catanescu, and L. C. Chien, Proc. SPIE 5947, 594706-1 (2005).

[6.9] Private conversation with S.T. Wu at CREOL.

[6.10] Technical paper online from Williams thin film materials, http://www.cerac.com/pubs/proddata/ito.htm

[6.11] D.S. Lockyer, J.C. Vardaxoglou, IEEE Trans. MTT 47, 1391, (1999).

[6.12] C.H. Lee, P.S. Mak, A.P. Dephonzo, IEEE J. Quantum Electron. 16**,** 277 (1980).

[6.13] F. Vaillant, D. Jousse, Phys. Rev. B 34, 4088 (1986).

[6.14] R.A. Street, J. Zesch, M.J. Thompson, Appl. Phys. Lett. 43, 672 (1983).

[6.15] R.A. Street, D.K. Biegelsen, R.L. Weisfield, Physical Review B 30, 5861 (1984).

[6.16] A. Morimoto, M. Matsumoto, M. Yoshita, M. Kumeda, T. Shimizu, Applied Physics Letters 59, 2130 (1991).

[6.17] H. Rinnert, M. Vergnat, G. Marchal, Journal of Applied Physics 83, 1103 (1998).

[6.18] S.R. Nagel, S.E. Schnatterly, Physical Review B 9, 1299 (1974).

[6.19] W. Beyer, B. Hoheisel, *Solid State Communications* 47, 573 (1983).

[6.20] F.J. Morin, Phys. Rev. Lett. 3, 34 (1959).

[6.21] P. Laffez, M. Zaghrioui, L. Reversat, P. Ruello, Appl. Phys. Lett. 89, 081909 (2006).

[6.22] P. Baum, D.S. Yang, A.H. Zewail, Science 318, 788 (2007).

[6.23] J. B. Goodenough, J. Solid State Chem. 3, 490–500 (1971).

[6.24] A. Cavalleri, T. Dekorsy, H. H. W. Chong, J. C. Kieffer, and R. W. Schoenlein, Phys. Rev. B 70, 161102 (2004).

[6.25] M.H. Lee, M.G. Kim, Thin Solid Films 286, 219 (1996).

[6.26] F. Guinneton, L. Sauques, J.C. Valmalette, F. Cros, J.R. Gavarri, Thin Solid Films 446, 287 (2004).

[6.27] M. Soltani, M. Chaker, E. Haddad, R.V. Kruzelecky, D. Nikanpour, J. Vac. Sci. Technol. A 22, 859 (2004).

[6.28] F.C. Case, J. Vac. Sci. Technol. A 5, 1762 (1987).

[6.29] F. Guinneton, L. Sauques, J.C. Valmalette, F. Cros, J.R. Gavarri, J. Phys. Chem. Solids 66, 63 (2005).

[6.30] T. Driscoll, H.T. Kim, B.G. Chae, B.J. Kim, Y.W. Lee, N. Marie Jokerst, S. Palit, D.R. Smith, M. Di Ventra, D.N. Basov, Science 325, 1518 (2009).

[6.31] M.J. Dicken, K. Aydin, I.M. Pryce, L.A. Sweatlock, E.M. Boyd, S. Walavalkar, J. Ma, H.A. Atwater, Optics Express 17, 18330 (2009).

[6.32] J. Ginn, B. Lail, J. Alda, G. Boreman, Opt. Lett. 33, 779 (2008).

[6.33] E.E. Chain, Applied Optics 30, 2782 (1991).

[6.34] A. Cavalleri, C. Tóth, C. W. Siders, J. A. Squier, F. Ráksi, P. Forget, and J. C. Kieffer, Phys. Rev. Lett. 87, 237401 (2001).

[7.1] N. Liu, H. Liu, S. Zhu, H. Giessen, Nature Photonics 3, 157 (2009).

[7.2] E.B. Franke et. Al., J. Appl. Phys. 88, 5777 (2000).

[7.3] Q. Zhong et. al., Phys. Rev. B 46, 2554 (1992).

[7.4] J.S. Hale et. al., Thin Solid Films 313, 205 (1998).